NUMERICAL ANALYSIS OF 3D MODEL FLAPPING FLAT PLATE

A THESIS SUBMITTED TO
THE GRADUATE SCHOOL OF NATURAL AND APPLIED SCIENCES
OF
MIDDLE EAST TECHNICAL UNIVERSITY

BY

BEGÜM DİZMAN

IN PARTIAL FULFILLMENT OF THE REQUIREMENTS
FOR
THE DEGREE OF MASTER OF SCIENCE
IN
AEROSPACE ENGINEERING

MAY 2016

ii

Approval of thesis:

NUMERICAL ANALYSIS OF 3D MODEL FLAPPING FLAT PLATE

submitted by BEGÜM DİZMAN in partial fulfillment of the requirements for the degree of **Master of Science in Aerospace Engineering Department, Middle East Technical University** by,

Prof. Dr. Gülbin Dural Ünver

Dean, Graduate School of **Natural and Applied Sciences** _____

Prof. Dr. Ozan Tekinalp

Head of Department, **Aerospace Engineering** _____

Assoc. Prof. Dr. D. Funda Kurtuluş

Supervisor, **Aerospace Engineering Dept., METU** _____

Examining Committee Members:

Assoc.Prof. Dr. Sinan Eyi

Aerospace Engineering Dept., METU _____

Assoc. Prof. Dr. Dilek Funda Kurtuluş

Aerospace Engineering Dept., METU _____

Asst. Prof. Dr. Kutluk Bilge Arıkan

Mechatronics Engineering Dept., Atılım Universtiy _____

Asst. Prof. Dr. Nilay Sezer Uzol

Aerospace Engineering Dept., METU _____

Asst. Prof. Dr. Harika Senem Kahveci

Aerospace Engineering Dept., METU _____

Date: 03.05.2016

I hereby declare that all the information in this document has been obtained and presented in accordance with academic rules and ethical conduct. I also declare that, as required by these rules and conduct, I have fully cited and referenced all material and results that are not original to this work.

Name, Last Name: Begüm DİZMAN

Signature:

ABSTRACT

Numerical Analysis of 3D Model Flapping Flat Plate

Dizman , Begüm

M.Sc., Department of Aerospace Engineering

Supervisor   : Assoc.Prof.Dr.D. Funda KURTULUŞ

May 2016, 103 pages

Flapping Micro Air Vehicles (MAV) studies gain an importance recently and in the future they will be used in civil and military applications in a widespread manner. Wing mechanism of MAV's is similar to birds' and insects' wing motion and is highly maneuverable. This flapping motion provides them fly in low Reynolds Number. In order to understand successful flight of MAVs , time dependent aerodynamic performance must be investigated in detail. This study includes investigation of 3D sweeping of flat plate numerically in water. The numerical simulations are performed at different constant pitch angles (5º, 30º and 45º) and sinusoidal sweeping angles with 30º and 60º which are 60 º and 120 º amplitudes. In the current study , water tank and 3D flat plate was modelled and analysis are carried out with a commercial CFD code and dynamic mesh option is used with user defined subroutines. Laminar Navier Stokes equations are used since the motion was in hover mode and at very low Reynolds numbers. Unsteady 3D aerodynamic forces are obtained. The purpose of this study is to examine pressure distribution and aerodynamic force coefficient effects of 3D time dependent wing numerically. In addtion , velocity vectors and streamlines effects are investigated on different planes. To the knowledge of the author, there are no other studies that investigate sweeping motion with different amplitudes at different pitch angles for flat plate.

Keywords: numerical simulation, low Reynolds number, Micro Air Vehicle, 3D flat plate, aerodynamic force coefficients, velocity vector, streamline

ÖZ

Üç Boyutlu Çırpan Düz Plakanın Sayısal Analizi

Dizman, Begüm

Yüksek Lisans, Havacılık ve Uzay Mühendisliği Bölümü

Tez Yöneticisi   : Doç. Dr.D.Funda KURTULUŞ

Mayıs 2016, 103 sayfa

Çırpan kanatlı Mikro İnsansız Hava Araçları çalışmaları son zamanlarda büyük önem kazanmış olup, gelecekte sivil ve askeri alanda yaygın bir şekilde kullanılacaktır. Mikro Hava Araçlarının kanat mekanizması, kuşların ve böceklerin kanat hareketine benzer yapıda olup, yüksek manevra yapabilir özelliktedirler. Düşük Reynolds sayılarında da uçabilme özelliğine bu çırpma hareketi sayesinde sahip olabilmektedirler. Mikro Hava Araçlarının başarılı bir şekilde uçmasının anlaşılması için zamana bağlı aerodinamik performansının iyi incelenmesi gerekmektedir. Bu çalışma üç boyutlu düz bir plakanın suyun içinde sayısal akışkanlar dinamiği yöntemi ile incelenmesini kapsamaktadır. Bu sayısal simulasyonda kanat farklı hücum açılarında iken (5º,30º,45º) iki farklı süpürme açısında (30º ve 60º) hareket verilmiştir. Bu iki süpürme açısı 60 ° ve 120 ° süpürme genliğindedir. Bu çalışmada 3 boyutlu kanat ve bulunduğu havuz çizilerek modellenmiş ve kod ile belirtilen frekansta dinamik ağ ile analizler gerçekleştirilmiştir. Laminar Navier Stokes denklemleri kullanılmıştır ve plaka hızı düşük ve dolayısıyla Reynolds sayımız düşük bırakılmıştır. Bu çalışmanın amacı sayısal analizle üç boyutlu zamana bağlı kanadın kuvvet ve basınç etkilerinin incelenmesidir. Ayrıca bu çalışmada farklı düzlemler üzerinde hız vektörleri ve akış yolu etkileri de incelenmiştir. Yazarın bilgisi doğrultusunda düz plaka ile farklı hücum açılarında ve farklı genliklerde süpürme hareketi yapan bir çalışma bulunamamıştır.

Anahtar Kelimeler: Sayısal Simülasyon , düşük Reynolds Sayısı , Mikro İnsansız Hava Araçları , Üç Boyutlu Düz Plaka, aerodinamik kuvvet katsayısı,hız vektörü, akış yolu

TO MY FAMILY AND MY SUPERVISOR

ACKNOWLEDGMENT

TABLE OF CONTENT

LIST OF FIGURES

LIST OF TABLES

LIST OF SYMBOLS

Re   Reynolds Number

α Angle of Attack

c   Chord length

b   Span

V   Velocity

ν Kinematic Viscosity

t   Time

P   Pressure

θ Angular Displacement

$\dot{\theta}$ Angular Velocity

r   Radius

f   Frequency

k   Reduced Frequency

U_{ref} Reference Velocity

L_{ref} Reference Length

CHAPTER 1

INTRODUCTION

1.1 Morphology of Birds:

Body and wing geometries and their interaction take an important role in flight condition of a bird. There are many wing shapes for different bird species. Wing geometry analysis show that bird shape differs so bird's flight differs. Broad wings allow efficient power for soaring on the other had long wings allow efficient lift for gliding.

Aspect ratio gives characteristics of flight for flapping animals. Wing shape can be defined with aspect ratio and described as wing span squared divided by wing area and given as:

$$AR = \frac{b^2}{S} \qquad\qquad [1.1]$$

Here , b is the wing span and S is the wing area.

Wing loading also is decribed as weight of bird to the area of both wings and is expressed as:

$$\text{Wing Loading} = \frac{\text{weight of bird}}{\text{area of both wings}} \qquad\qquad [1.2]$$

From the equation we can say that higher wing loading means higher bird mass and requires more energy for flying. However, lower wing loading requires lower energy consumption.

1.2 Kinematics of flapping flight:

Wing stroke of birds generally divided into two phases which are translational and rotational phases. Translational phase consists of upstroke and downstroke motion and in addition to this, rotational phase consists of pronation and supianation. Pronation occurs before downstroke motion and supianation on the other hand occurs before the upstroke motion. During the downstroke-to-upstroke motion, the wing 'supinates' means that a rotation brings the ventral surface of the wing to face upward rapidly. The wing 'pronates' means that at the end of the upstroke, a rotation brings the ventral surface to face downward at the end of the upstoke. In addition, sweeping motion means that translational motion in the arc.

Figure 1.1: Flight Path

We can see flight path of bird from the Figure 1.1.
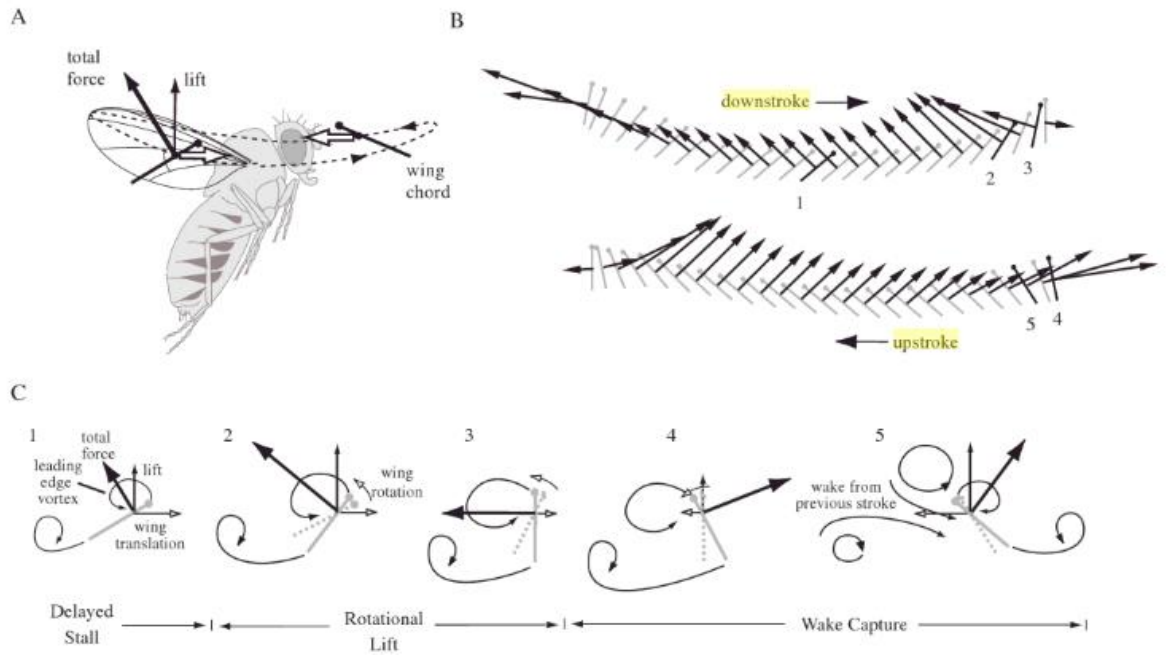
Figure 1.2: Downstroke and upstroke motion of insect [1]

Figure 1.2 shows aerodynamic mechanisms used by insects. (A) Insects flap their wings back and forth during each stroke under hover condition. The dotted line shows wing path and white arrows shows wing motion. Thick arrows shows total aerodynamic force which act perpendicular to the surface of the wing and can be decomposed lift and drag components which is shown with thin arrows. (B) Wing motion diagram shows magnitude and direction of the total aerodynamic motion which is shown with black arrow. Small circles indicates leading edge of the wing. (C) Drawing shows air flow around the wing.

Figure 1.3: Hummingbird in hover condition [2]

1.3 Hovering Flight:

Hovering flight is generally observed in smaller birds and insect because larger birds can not rotate wings between forward and backward strokes. Hovering is a state of flight and exhibited by bees, dragonflies and hummingbirds. The speed of flying animals is equal to the speed of the wind. In hover, vertical generated force is equal to weight. The ability to stay in hover condition depends on flying animal's size and the moment of the inertia of the wing and wing shape.
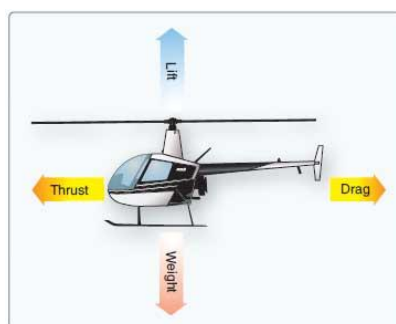
Figure 1.4 Aerodynamic forces in hover condition [3]

$$\text{Lift=Weight (in hover condition)} \qquad [1.4]$$

4

1.4 Background of Flapping Motion:

Bird, bat and insect flight has inspired humans for many years. Man try to understand the flight of natural creatures. There are a million of flying insects and warm blooded species can fly upper level in the atmosphere [4]. Engineers try to replicate wing action of birds. Body and wing geometries and their action are important in flight performance of a bird. Wing shape differ so bird's flight differs such as broad wings and long wings.

Birds, insects use flapping motion and create lift and thrust and these motions can guide the design of micro air vehicles. Knoller and Betz [5-6] with an effective angle of attack studied vertical motion that generates aerodynamic forces which are lift and thrust components. Like these experimental investigations support the Karman-Burger thrust generation hypothesis. Jones and Platzer [7] tested numerically and experimentally flapping MAV's. They used flow visualization and Laser Doppler velocimetry for experimental research and in addition to this panel and Navier Stokes computations are used for numerical research. These studies are done to investigate aerodynamic characteristics and combinations of flapping wings. Also Willis et al. [8] and Persson et al. [9] used numerical method to analyze the flapping MAV flight. In these research a computational frame work was used and some tools were used to solve Navier Stokes equations which are computational methods such as panel method and Galerkin method. In addition, both experimental and numerical investigations are done by Jones and Platzer [10-11], Katz and Plotkin [12] and Liu and Kawachi [13]. Liu and Kawachi use numerical model for insect flight. They used time accurate, incompressible, three dimensional laminar Navier Stokes equations. The geometry of the wing is based on Manduca Sexta with an elliptic airfoil shape. Reduced frequency was 0.37 and the Reynolds number was 4000. Mean chord length was 1,83 cm. In Jones and Platzer study [14], flapping wing propulsion is investigated numerically and experimentally and the results are compared. Numerical method based on panel method and experimental one was based on wind tunnel. Airfoils that they tested were symmetric (NACA0014) and asymmetric (NACA23012). Chord length of wing was 64 mm and span was 1270 mm. Recently, number of publications are released for flapping wing aerodynamics and shows great interest in this research field [15-16].

5

1.5 Flapping Micro Air Vehicles:

First MAV research was started in 1997 with DARPA (Defense Advanced Research Projects Agency) which request a new type of UAV with size constraint. The design conditions are that size constraint must be 15 cm, endurance must be 1 hour with a GTOW which is less than 100 grams.

Recently two main types of MAV's are developed which are fixed and rotary wing MAV's.

Fixed wing MAVs are less complex, have fewer moving parts and are used fot long endurance missions. Succesful fixed wing MAV prototypes are used recently. In 1980, 80 g Black Widow is produced and the win span is 6 inch with 30 minutes endurance. Later ın 2002, WASP [17] produced another MAV which has 33 cm wing span with an endurance of 107 minutes. But for fixed wing MAVS, there are some design challenges and disadvantages to use. They can not fly at low speeds and hover condition and are not suited for missions in confined regions.

Rotary wing MAVs are able to fly at hover condition and most widely used type is quadrotor which have four rotors. Quadrotors have good flight stability and agility and have large operational envelopes. The disadvantage of them is diffucult to control especially in gusty environments compared to fixed wing besides fixed wing can not hover.

With these limitatios, a vehicle which can also hover and fly at gusty environments easily and fly at low speeds. The solution is flapping MAVs.

Flapping MAVs, FMAVs have high aerodynamic efficiency and gust tolerances. The wing can sweep in the air with large pitch angles.Flapping motion provides both vertical and propulsive forces in order to flight. For example, real insects are observed that have high maneuverabilit in gust tolerance capability for flapping wings.

1.6 Objective and Outline of the Present Study:

The objective of this thesis is to understand the underlying mechanisms in flapping motion that are responsible for generation of aerodynamic forces and also to

achieve an improvement for lift and drag force outputs in order to help to design more efficient flapping wings. Numerical simulations on a flapping flat plate in hover conditions are done in this research. Three different pitch angles (5º, 30º, 45º) of flat plate are used for analysis. It is assumed that plate undergoes flapping motion with two diffrent sweep angles which are chosen as 30º and 60 º. In this research, force coefficients and pressure distributions are examined for laminar flow at low Reynolds number. Also, velocity vectors and streamlines are plotted at different cases. In this study, ANSYS Fluent 14.0 [18] with a user defined function is used to solve the problem for flapping rectangular flat plate at low Reynolds number in hover condition.

The present study is organized as five chapters. Chapter 1 introduces the morphology of birds and kinematics of flight. In addition, the background of flapping motion studies, the objective and outline of the present study are emphasized. Next, Chapter 2 includes the literature surveys of numerical and experimental methods. The 3D model and mesh view of flat plate and water tank in Gambit software program is presented in Chapter 3. In addition, the CFD analyses which were conducted by using ANSYS-Fluent package program were detailed in this chapter. Chapter 4 of the study gives the details and results of the forces and pressure distributions on flat plate. Chapter 5 concludes the work with the general conclusions drawn and the recommendations for the future work.

CHAPTER 2

LITERATURE SURVEY

In recent years, micro air vehicles have gained great importance and will be used for commercial and military applications in the future. Wing mechanism of MAV's are similar to birds and insects wing mechanism and is highly maneuverable. This flapping motion helps them fly in low Reynolds Number. In order to understand successful flight of MAVs , time dependent aerodynamic performance must be investigated in detail. MAVs, insects and birds share a direct relation in size speed, flight regime and mission.

Lots of studies are carried out on low Reynolds number aerodynamics to understand flight of birds and unsteady flapping wing motion [19-21].

Recently, numerious publications related with the flapping wing aerodynamics are issued to show great interest of this research field. Recent studies can be found in the books related with biological flyers [22-23] which are insects and birds and MAVs [24 - 25] .

2.1 Review of Experimental Studies:

Kim and Gharib [26] experimentally studied vortex structures in translating and rotating rectangular model plates with constant chord length along the span. Digital Particle Image Velocimetry was applied to understand the structure and dynamics of the vortex generated by plates for both translating and rotating cases with A.O.A of 45° at Re of 60, 1100 and 8800. Vortex formation of translating plate compared with the rotating plate. For the rotating case, the plate rotated with constant angular velocity as angular velocity. For the translating case, the plate translated with the same velocity. During translation, spanwise flow develops first near the center of plate. The influence of the tip, leading edge vortices develops nonuniformly along the span. In the rotating case, vortex structure is stronger near the tip than the root so leading edge vortices are tilted.

Khan et al. [27] studied the investigation of unsteady aerodynamics by experimental method. For this purpose, dynamically scaled robotic flapper was used. The method based on the principle of dynamic similarity to determine aerodynamic force coefficients. The wing was made of carbon rods and the length of it was 0.58 m. Aspect ratio was 5.7677 and flapping frequency was 0.5 cyc/sec. Reynolds number interval was 12000–20000.

Das et al. [28] investigated the butterfly shaped wings and in this research butterfly flapping motion is replicated. To understand the unsteady flow field, flow visualization and PIV experiments are performed. Their experiments are carried out at Re number of 3000-7000 and force measurements are done. The purpose of their study is to understand nature of flapping flight. In the experiment, closed circuit wind tunnel is used. The flapping frequencies are 0.46 and 0.7 Hz. The wing is triangular wing. The conclusion of this study shows that force results are more dependent on frequency. They concluded that the high frequencies result more lift coefficients.

George [29] studied for design and analysis of a flapping wing mechanism for optimization . The aim of their study was to improve lift and thrust force outputs and help to design more outputs by using two methods. In this research a ladybug is used as a model . The thickness of the wing is 3 mm. The method which is used is direct linear transformation to explore flapping wing kinematics of ladybug. The mechanism is a gear design with two wings in underwater. Two methods are used for this investigation. First study is based on Box-Behnken screening design to search lift and thrust combination and in the second study is to build a response surface. Box Behnken design is an experimental design for response surface methodology. This surface is used for optimization to produce more efficient combined lift and thrust forces. In order to test flapping mechanism , a structural design was made which is shown in Figure 2.1.
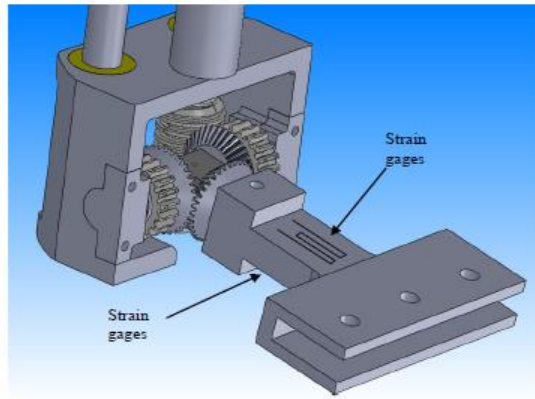
Figure 2.1 Flapping wing mechanism [29]

Each experimental runs, a high level MATLAB optimization code running on a PC and gives force data by using encoders and strain gages. Then lift and thrust production data are plotted by using Box – Behnken iterations. Figure 2.1 shows the thrust and lift coefficients for sinusodally flapping motion at frequency of 0 -0.5 Hz in water whose velocity 25 m/s with an amplitude of 45^0 with a variable pitch angle.
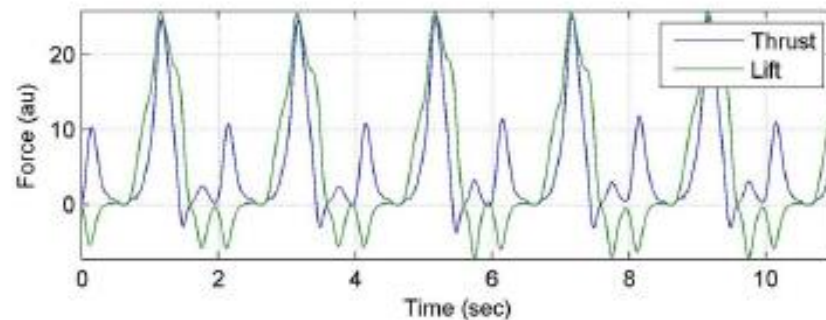
Figure 2.2 Aerodynamic Forces of sinusoidally flapping motion [29]

Resulting forces improved lift and thrust results and results are consistent.The results can be aid to design more efficient   micro air vehicles with better understanding of flapping wing aerodynamics.

Morrison et.al [30] studied experimental investigation of rigid and flexible wings with bio-inspired kinematics. The wings have periodic motions with a given pitch and flapping angle. The wings are thin flat plates with an aspect ratio 7.2. Experiments are done underwater with a Reynolds number which is 7100 and reduced frequency is 0.21. Flapping motions are compared between rigid and flexible

wings. In experiment method a stepper motor driven assembly is used to move the wings in an arbitrary periodic motion.
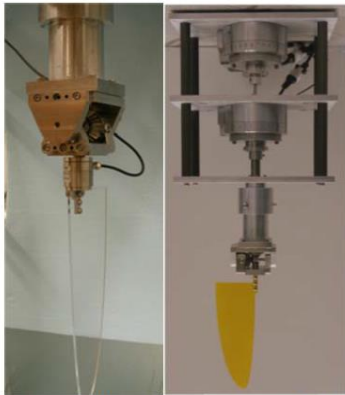
Figure 2. Flapping apparatus and load cell.
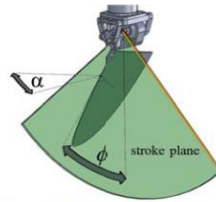
Figure 1. Coordinate system
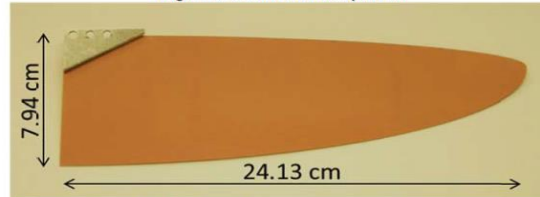
Figure 3. Flexible aluminum wing and support.

Figure 2.3 Flapping apparatus and wing configuration [30]

In different pitch angles , rigid and flexible thrust coefficients are plotted and compared. According to results, flexible wing yield a significant performance based on analysis.

Several different experimental investigations have been performed to understand the unsteady mechanisms of aerodynamic forces and moments generation for flapping wing MAVs.

Eisma [31] investigated flow visualization and force measurements on a flapping-wing MAV DelFly II in forward flight configuration. Delfly II is a bioinspired flapping wing MAV. Wing span is 280 mm and chord length 80 mm. Reynolds numbers range from 5500 to 22000. For experimental research a brushless motor is used with a controller and a gear system and a crankshaft mechamism which drive the wings in flapping motion (clap and fling motion). Force results are taken at different flight configurations with PIV method by using force sensor which is connected to a PC with Data Acqusition Card. Studies are done in low speed wind tunnel. At different angle of attacks lift force are plotted with respect to time and according to results when angle of attack increases, lift force increases. So sufficiently high A.O.A is beneficial for a efficient lift .

(a) Lift force   (b) Thrust force
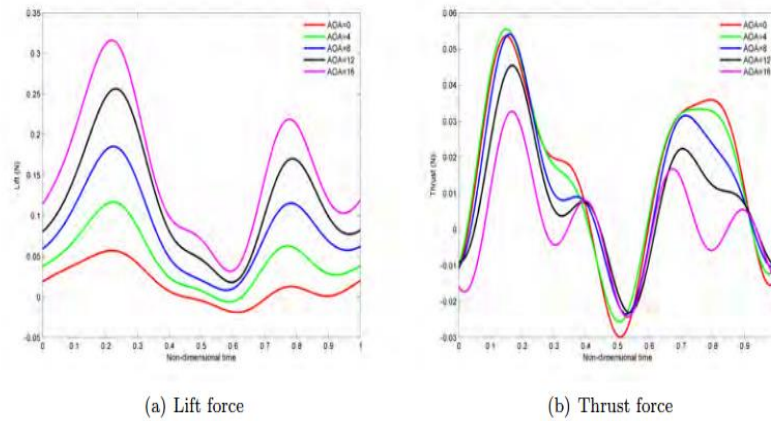
Figure 2.4 Lift and Thrust outputs at different angle of attacks of DelFly flapping at 10 Hz. [31]

The forward velocity is 3 m/s.The angle of attack varies from 0 to 16 degree. [Fig 2.4]

Çakır [47] has performed an experimental study in a water tank and compared aerodynamic force coefficients of 3 different wing geometries which is shown in Figure 2.5 and Figure 2.6.

Flat Plate Wing Geometry

Hummingbird wing geometry

Zimmermann wing geometry
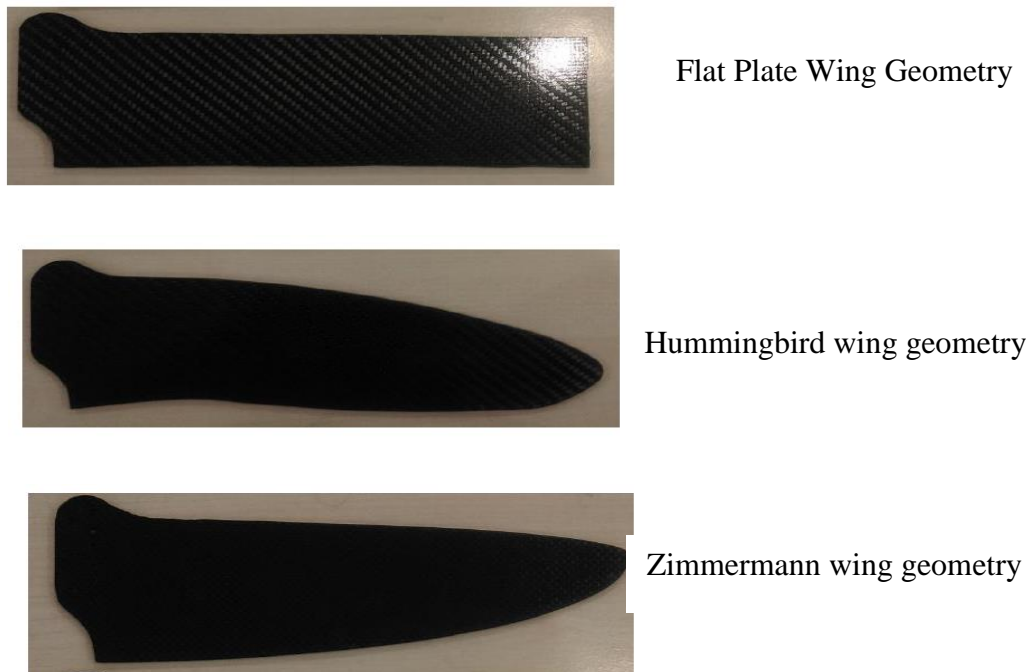
Figure 2.5: Different wing configurations used for experimental method [47]
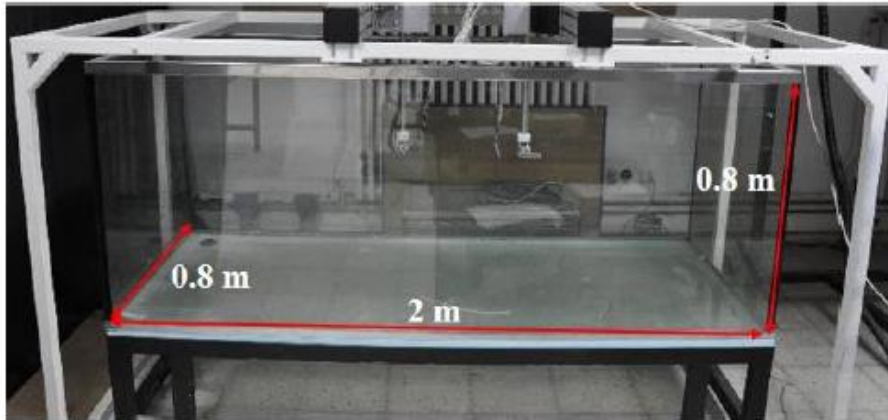
Figure 2.6 Water Tank with its dimensions [47]

2.2 Review of Numerical Studies:

CFD is an alternative way that can be used in conjunction with experiments to understand the flow physics. Various investigations have been done for 2D and 3D pitching/plunging airfoils [34-35].

Ellington et al. [36] studied visualization of the airflow around wings of the hawkmoth Manduca sexta and a "hovering" large mechanical model – the flapper. They designed a scaled up robotic insect model to study aerodynamics of the hawkmoth Manduca sexta motion. Robotic insect replicated wing movements of hovering hawkmoth. Also Liu and Kawachi [37] and Liu et al. [38] studied same wing model numerically to show unsteady and viscous flow around hawmokth Manduca sexta by using Navier-Stokes solver. A hawkmoth is modeled to replicate real flapping wing motion. Their results are consistent with Ellington et al. [35] results. It shows that computed lift is produced during downstroke and in latter half of the upstroke.

Masarati et al. [32] studied for Tightly Coupled CFD/Multibody Analysis of Flapping-Wing Micro-Aerial Vehicles numerically. This study focuses on to predict the aeromechanical behaviour of significantly flexible flapping wings. Analysis were done by using compressible and incompressible Unsteady Reynolds Averaged Navier Stokes solver. Three semi span models of a straight, untapered and untwisted wing which is exposed to harmonic heave motion. The NACA 0012 airfoil is used with a chord length of 0.1m. The three wings have identical geometry however differ

14

from each other with structural properties. One of them was rigid, the others were flexible and highly flexible. In rigid case, the wing is subjected to harmonic plunge with k=2 and Re =10000 to 30000. In flexible case analyses are done with k=1.82 and Re=30000 The study involves comparison of deformations and generated thrust coefficients.

Niu et al. [33] studied a NACA0012 flapping wing models to investigate vortex behaviours and forces. The chord length of first NACA0012 model wing is of 0.1m . Wing span is 0.6 m, velocity is 0.393 m/s , Reynolds number is 30000 and reduced frequency is 1.82. The chord length of second model is 0.02 m, span is 0.1m , flapping angle 30^0 , flapping frequency is 20 Hz and Reynolds number is 60000. Vortex behaviors and forces are investigated according to the reduced frequency of the three-dimensional flapping wings. Unsteady 3D incompressible Navier-Stokes equations were used. The leading edge vortex, trailing edge vortex and tip vortex around the flapping NACA 0012 wings are discussed. Also it is noted that pressure difference between the upper and lower surfaces play a major role in the formation of leading and trailing edge vortex. The thrust and lift coefficients are also investigated and it shows that lift and thrust coefficicents become larger as reduced frequency increases from 0.3 to 0.6.

Lin and Hu [38] studied flapping wing numerically by using both Euler and Navier-Stokes equations. Firstly, for 2D NACA0014 airfoil, time depend thrust and lift coefficients are compared with reduced frequencies of k=0.1 and 0.2 using Euler equations during pure plunging motion. Also the mean thrust, lift coefficient and propulsion efficiency varying with mean angle of attacks under different plunging reduce frequencies of k=0.1, k=0.2 and k=0.5, are compared. The results show that a flapping flight with pure plunging motion gains additional thrust output by increasing plunging frequency. 3D wing with NACA 0014 airfoil is analyzed for different reduced frequencies of k=0.1, 0.2 and 0.5 during pure plunge motion. 2D and 3D Euler solutions are compared. Both lift and thrust coefficient in 3D are below the 2D results. Plunging/pitching motion are also calculated for 2D and 3D wings. 2D Euler simulation were carried out with a amplitude of h=0.1 c and reduced frequency k=0.1. 3D NACA0014 rectangular wing with a aspect ratio of 8 is subjected to turbulent pitching/plunging motion. For the plunging/pitching motions, maximum propulsion is occurred with the phase shift of 90 degree.

15

Isaac et al. [39] studied together for kinematics of controlled wing at low Reynolds numbers and high angle of attack values. 2D airfoil model is used for analyses. The leading edge of the airfoil was elliptic and trailing edge was tapered model with a chord length of 30 cm. The maximum thickness was 1.4 cm. The analyses were carried out with a range of Reynolds numbers (500-5000) and two angle of attack values (30^0 and 45^0). Time accurate, unsteady simulations were analyzed. The results show that at high angle of attack , the LEV became dominant and at higher angle of attack , the LEV and TEV were equally dominant.

2.3 Review of Both Numerical and Experimental Studies:

Usherwood and Ellington [40] investigated the forces acting on a hawkmoth model wings in "propeller-like" rotation (revolution). It shows that rotating hawkmoth model wings produce high lift and profile drag forces because of the leading edge vortices. A two winged propeller was designed at   Re= $O(10^3)$ with a rotation frequency of 0.1 Hz. Knowles et al. [41] studied flapping wing MAV's based on insect-like aerodynamics. In order to understand and design wing aerodynamics and kinematics, a combined analytical, experimental and CFD method is carried out. 2D CFD and linear experiments (in water tunnel) and also 3D CFD and equivalent experiments (in water tank) are used to investigate the spanwise flow in leading edge vortex with Re of 500. The study shows that for 2D flows the leading edege vortex is unstable for all but very lowest (<50) Reynolds' numbers. CFD results for rotating 3D wing shows that at high angle of attack produces a conical leading edge vortex as has been seen in physical experiments and also by others [42]. Also it is noted that LEV depends on Reynolds numbers. If Reynolds number increases a critical value, a Kelvin-Helmholtz instability [43] occurs in the LEV sheet hence resulting the sheet breaking down on outboard sections.

Yongsheng Lian [44] compared numerical and experimental results in his investigation. The wing is SD7003 rectangular wing and aspect ratio is 3. The chord length was 8 cm and reduced frequency is 3.93. 3D Navier Stokes equatins and moving grid technique were used for analyses. 2D (experimental) and 3D (numerical) force histories and flow field are compared. The conclusion shows that

blockage and domain size plays an important role for flow field and aerodynamic forces.

Mayo [45] studied for flexible flapping wings in forward flight and experiments which are done are coupled with CFD and CSD. 2D Partice image velocimetry (PIV) and force measurements were carried out in a wind tunnel with a 3 m/s flow speed. In the research rigid and flexible wings are used.Reynolds number is 15000 and flap frequency is 0,4,6,8,10 Hz. AR=1.67 and t/c=1% . Force coefficients and LEV circulation are examined along the span. RANS solver with a structural model which is MBDyn are used to investigate results. Performance of flexible and rigid wings are compared with different situations. According to results, in general flexible wings are less complex and lighter. Due to the dynamic twisting, greater forces achieved for flexible wings. These results Show that sufficient amount of flexibility makes the wings more efficient.

Prosser [46] studied flapping wing design of a dragonfly – like micro air vehicles. In this study Quad-wing vehicle is analyzed by using Computational Fluid Dynamics, potential flows analysis and experimental testing. The wing span is 7 cm, chord length 3 cm with a flapping frequency 30 Hz. In CFD method ANSYS Fluent 12.1 solver is used as a solver and in experimental testing benchtop flapping device is designed which is shown in Figure 2.7.

Figure 2.7: Flapping device design [45]

The force , moment and power results are investigated. Mesh which is used is Dynamic mesh. Lift and thrust forces are plotted with respect to flapping period and

compared with experiment method and also velocity vectors an pressure contoures are investigated in CFD method .

2.4 Review of Recent Studies at METU:

Mutlu [48] investigated 3D complex flow around flapping wings experimentally by developing a tandem mechanism. The aim of the study is to develop flapping wing test setup. Multiaxial force and torque sensor at the root chord of the wing is used for the mechanism. So by doing this, forces and moments can be measured. The wing model is Zimmerman wing model and experimental analyses are done in water tank. The wing is subjected to pure and combined pitch and plunge motions. The wing span is 24 cm with 8 cm chord length and thickness is 3mm and flapping frequency is 0.14. In the study, force and moment measurements are compared and discussed.

Günaydınoğlu [49] studied numerically flapping airfoils in hover and forward flight condtion at low Reynolds regime. Two dimensional Navier Stokes equations are solved by using moving grids. The airfoil model is SD7003 model. Reynolds number range from 10000 to 60000 and reduced frequency is k=0.15. In forward flight, wing is subjected to pure plunge and combined pure-pitch motion for the investigation. In hover the effects of vertical translational amplitude and Reynolds numbers are also investigated. When the amplitude increases, vortex becomes dominant.

Hızlı [50] studied pitching/plunging airfoils in hover condition experimentally and numerically. Four airfoils are used for investigation and these are SD7003,NACA0012,10% elliptical,%10 thick flat plate. Chord length is 0.06m. The aim of this study is to investigate the effect of pitching and plunging amplitudes in hover condition and to compare the numerical and experimental results for the validation. In numerical method unsteady, incompressible Navier Stokes equations are used and the experimental method PIV technique is used.

Kaya [51] studied viscous flow over flapping airfoils. The flow is laminar, Reynolds number is 10000 and reduced frequency ranges from 0. 5 to 3. Two different airfoils are used which are NACA0012 and NACA0014. Unsteady viscous

flow is investigated by using Naiver Stokes solver. The purpose of the study is to maximiz thrust production and the efficiency of the thrust. Thrust generaton is optimized with pitching – plunging amplitudes and flapping frequency. The study shows that thrust generation of flapping airfoils strongly depend on phase shift. Reynolds Averaged NaiverStokes Equations are used.

Şenol [52] studied four bar flapping mechanism. The aim of the study is to design and test four bar mechanism. The mechanism is double rocker. The wing model is Drosophilla wing with 1mm thickness and 29.15 mm wing length. The four bar mechanism is actuated by a servo motor. The motion is püre flapping motion in hover condition. By using force transducer force values are obtained. Şenol studied both experimentally and numerically and in numerical method , 3D incompressible Navier Stokes equations are used.

Ormancı [53] investigated unsteady flow models for flapping wings' controller design approach. The scope of the study is to develop an unsteady model capable of calculating aerodynamic forces and moments for insect flight. In experimental method, unsteady panel method is used. Calliphora wing is taken as a model with 1mm thickness. Chord length of the wing range from 0.1 to 0.3. Reduced frequencies are taken as f=5.85 and 11.2 Hz for cases. In addition , flat plate wing model is used for comparison . The chord length of flat plate is 0.02915m and frequencies which are f=5.85 and 11.2 Hz are same with Calliphora wing model.Double wing four bar mechanism with piezo-actuator is used for experimental method. In the study , experimental results are compared with CFD results which are taken from Şenol's study.

Ansys Dynamic mesh options have already been used by Gunaydınoğlu, Hızlı and Şenol [49,50,52]. A similar procedure is applied to the current study and 3D flapping motion in hover is analyzed numerically by using ANSYS Fluent Software program.

Table 2.1. Comparison of Research Methodology

Researchers	Wing Model	motion	span/mean chord	Reynolds Number	Frequency	Operating Medium	Type of Reseacrh
George [29]	Ladybug model	Flapping	-	-	0-0.5 Hz	Water	Experiment
Morrison [30]	Rigid and flexible wings	Flapping	-	7100	k=0.21	water	Experiment
Eisma [31]	a bioinspired flapping wing	Clap and fling	b/c=2.8/0.08	5500-2200	f=10 Hz	Low speed wind tunnel	Experimental
Ellington et al.[35,36]	Robotic insect model of The hawkmoth Manduca sexta	hovering	b=1.03 m	-	f:0.3 Hz	Wind tunnel	Experimental
Liu and Kawachi [37]	3D-The hawkmoth Manduca sexta wing model	translational & rotational motion	C_m=1.83cm b=4.83 cm	5000	k=0.37 flaping freq f =26.1	Numerical Simulation (fluid is air) Navier Stokes Solver (3D incompressible laminar navier stokes equations)	Numerical
Liu et al.[38]	3D-The hawkmoth Manduca sexta robotic wing model	translational & rotational motion	C_m=1.83cm b=4.83 cm	3000 4000	k:0,37 flaping freq f =26.1	Numerical Simulation (fluid is air) Navier Stokes Solver	Numerical
Kim and Gharib [26]	rectangular model plate	Trapezoidal & sinusoidal	chord=60 mm	1100 8800 60	-	Water Water Oil	Experiment

Usherwood and Ellington [40]	hawkmoth model wing	translating & revolving motion	b=500mm	10000	k:0.1	Smoke visulation	Experiment
Knowles et al. [41]	Aerodynamic model of the insect like flapping wing model	translational & rotational motion	c=50 mm	500	-	2D Water Tunnel 2D CFD (incompressible fluid)-RANS 3D Water Tank 3D CFD(incompressible fluid)-RANS	Numerical & Experimental
Massarati et al.[32]	3D -NACA 0012	harmonic heave motion	c=0.1 m b=0.3 m	10000 to 30000 30000	k=2 k=1.82	Numerical simuation (fluid is water) Navier Stokes Solver	Numerical
Niu et al.[33]	3D -NACA 0012	heave motion	c=0.1 m span=0.6m & c=0.02 m span=0.06m	30000 60000	k=1.82 f=20	Numerical simuation (fluid is air)	Numerical
Lin and Hu[34]	2D , 3D-NACA 0014	plunging / pitching motion	-	-	k=0.1 , 0.2 , 0.5	Numerical study - Euler & Navier stokes Solver	Numerical
Isaac et al.[39]	2D elliptic airfoil	-	c=30 cm	500 to 5000	-	Fluent solver	Numerical
Zaeem [27]	dynamically scaled robotic flapper	flapping	b = 0,58 m c:0.270-0.115m	12000 – 20000	flappin frq f:0,5 cyc/sec k:0.332 – 0.2095-0.2477	principle of dynamic similarity (experıment)	Experiment
Debopam Das[28]	triangular wing	butterfly flapping motion	Wing length: 6,35 -8,89cm	3000-7000	flapping frequency f= 0.46 and 0.7 Hz	flow field flow visualization and PIV experiments in a closed circuit wind	Experiment

						tunnel	
Yongsheng Lian [44]	SD7003 rectangular wing	flapping wing motion	c=8 cm	10000	k=3.93	3D navier stokes equations and moving grid technique (numerical)	Experimental & Numerical
Mayo [45]	Flexible and rigid wings	Flapping	t/c=0.01	1500	f=0-10Hz	Wind tunnel & CFD & CSD (experimental & numerical)	Experimental & Numerical
Prosser [46]	Dragonfly wing model	Flapping	7/3	*	f=30 Hz	Wind tunnel & CFD (Dynamic mesh) (experimental & numerical)	Numerical & Experimental
Mutlu [48]	Zimmerman wing	pure and combined pitch and plunge motion	24cm/8cm	-	f=0.14 Hz	Water tank	Experimental
Günaydınoğlu [49]	SD7003 2D airfoil	pure plunge and combined pure-pitch motion	-	10000 - 60000	k=0.15	Navier Stokes Equations Air	Numerical
Hızlı [50]	SD7003, NACA0012, 10% elliptical, %10 thick flat plate	pitching/ plunging	c=0.06m	100 - 1200	k=1.00-11..46	Water unsteady, incompressible Navier Stokes equations & PIV Technique	Experimental & Numerical
Kaya [51]	NACA0012 NACA0014	Pitching-Plunging & Flapping	-	10000	k=0.5-3	Reynolds Averaged Navier Stokes Equations Air	Numerical

						3D incompressible Navier Stokes equations & Double Rocker mechanism Air	Numerical & Experimental
Şenol [52]	Drosophilla wing	L=29.15 mm t=1 mm	-	-	-		
Ormancı [53]	Calliphora wing	flapping	c=0.1 -0.3	-	f=5.85-11.2 Hz	Unsteady panel method & Navier Stokes Equations	Experimental & Numerical

In this study, unsteady aerodynamic forces and moments were calculated numerically for flapping flat plate by using a commercial software (ANSYS) and also numerical solutions are compared for different pitch angles and sweeping angles distinctively.

CHAPTER 3

3D NUMERICAL MODEL OF FLAT PLATE AND WATER TANK AND NUMERICAL ANALYSIS

In this section, numerical analysis of 3D flat plate model and water tank model are done using ANSYS Fluent Software Program.

3.1 Gambit Software Program:

The model is constructed using Gambit Software Program.Gambit has a single interface for both geometry creation and meshing. The advantage of Gambit is ease of use fast modelling and intelligent meshing. Later 3D model (flat plate and water tank) is created with dimensions in Gambit software program. The mesh size of other region in control volume is a bit coarser than mesh size of the area close to the flat plate.

3.2 3D Model Design

Figure 3.1 shows the dimensions of water tank and Figure 3.2 shows the dimensions of flat plate. Also Figure 3.3 shows 3D solid model by using CFD post program. Sweeping region is chosen five times greater of the wing to investigate aerodynamic effects accurately around the wing since fluid interacts with wing at that region. The sweeing area is chosen close to the wing motion area since smaller area provides better solution.
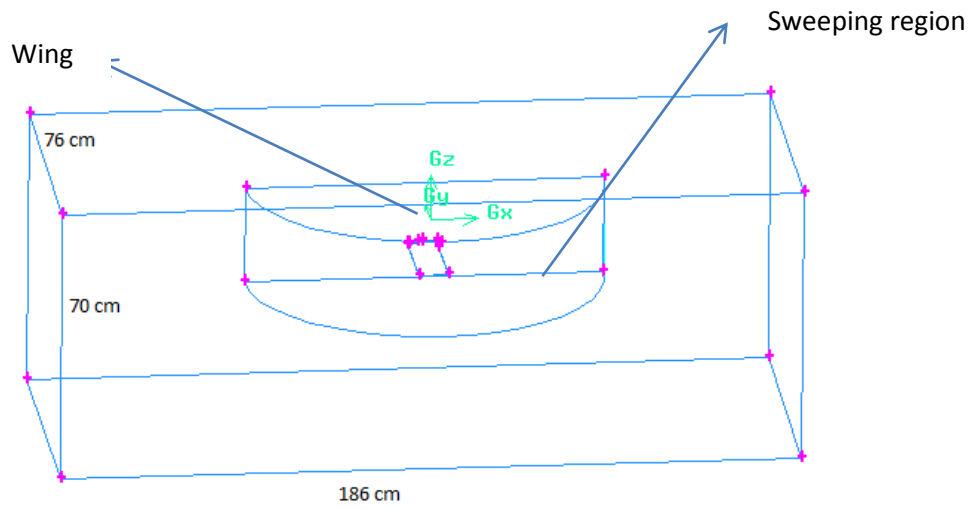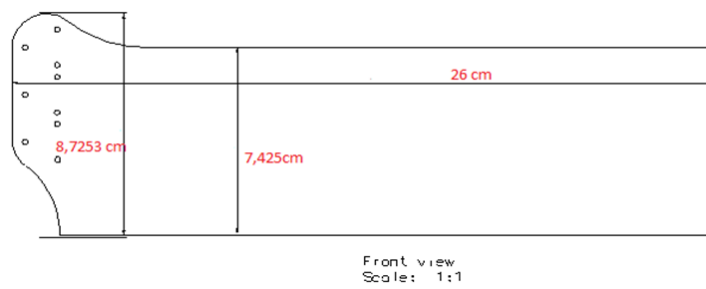
Figure 3.1 :Dimensions of water tank
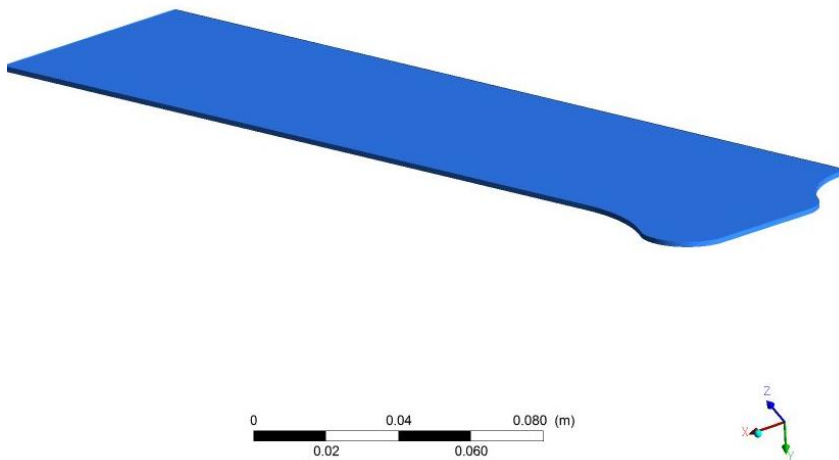

Figure 3.2 : Dimensions of flat plate

Figure 3 3:Solid 3D view of the wing

3.3 Mesh Determination

Coarse, medium and fine mesh are used for determination of better accuracy. Coarse mesh run took one and half weeks, medium mesh took two weeks and fine mesh took three weeks time period until the runs are reached desired values. When aerodynamic coefficients are plotted, it is seen that coarse, medium and fine mesh results are similar but coarse mesh have low mesh quality and fine mesh run takes too time. Medium mesh have better quality so medium mesh is chosen for our cases. Fine mesh is used in sweeping area in order to reach better accuracy around the sweeping wing since fluid interacts with wing in that region. Figures 3.4 and 3.5 show mesh configuration from Gambit and CFD Post program. Figure 3.6 shows zoom view of the mesh on the wing. Also Figure 3.7 shows mesh quality of the water tank and the wing by using orthogonality.

3.3.1 Dynamic Mesh

Dynamic moving meshes are practical for wide range applications. These applications are used for fluid structure interaction, 3D model analyses and among others. In moving boundary flow problems, grid quality is important to reach accurate solution for each time step. There are many ways for grid generation for example, grid can be generated by using Ansys and Gambit software programmes with various geometries such as hexagonal and triangular. In this study remeshing method is used for dynamic method since spring - based smoothing method can not suitable large boundary displacement. In remeshing method, mesh is updated with new cells and solution can converge easier.
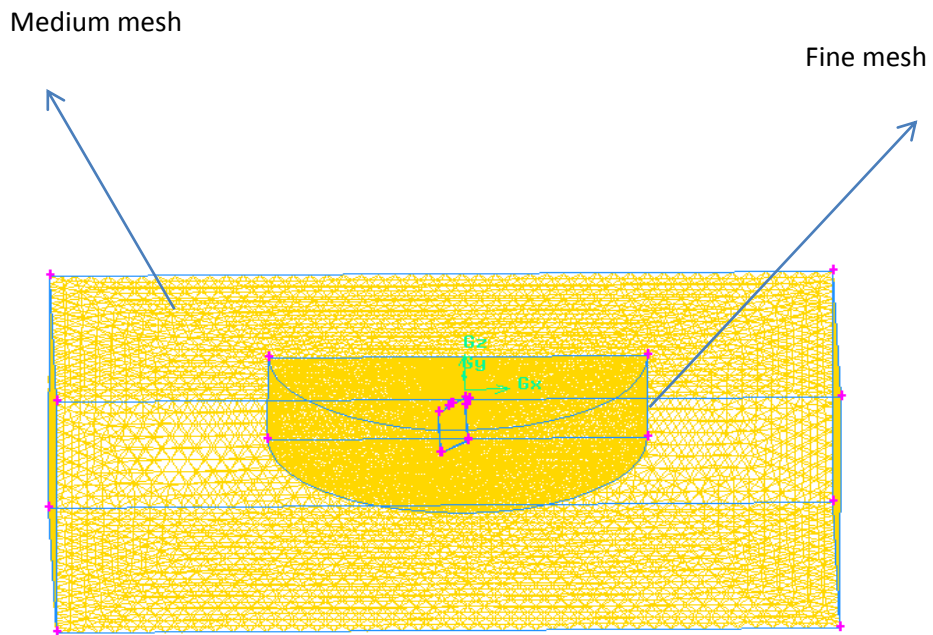
Figure 3.4: Mesh View by using Gambit Software Program
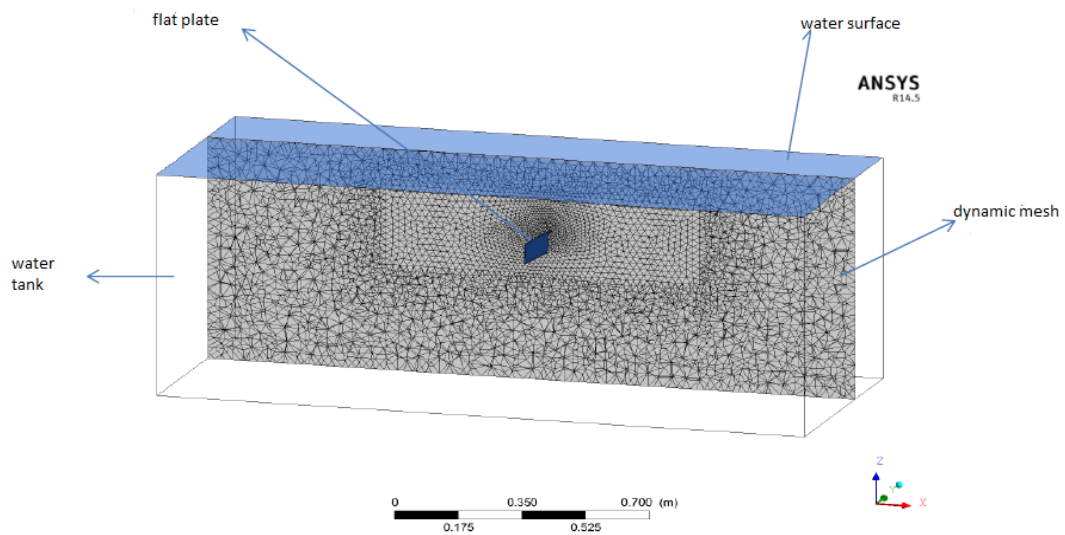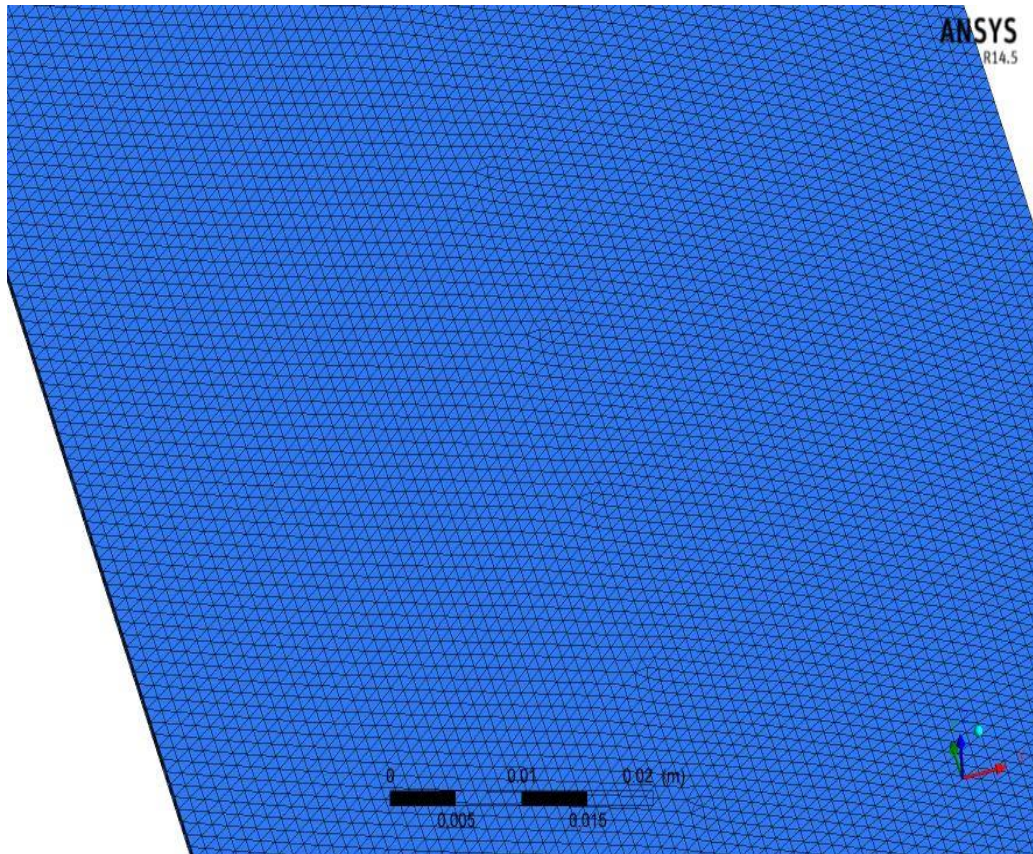

Figure 3.5 : Mesh view by using CFD post program
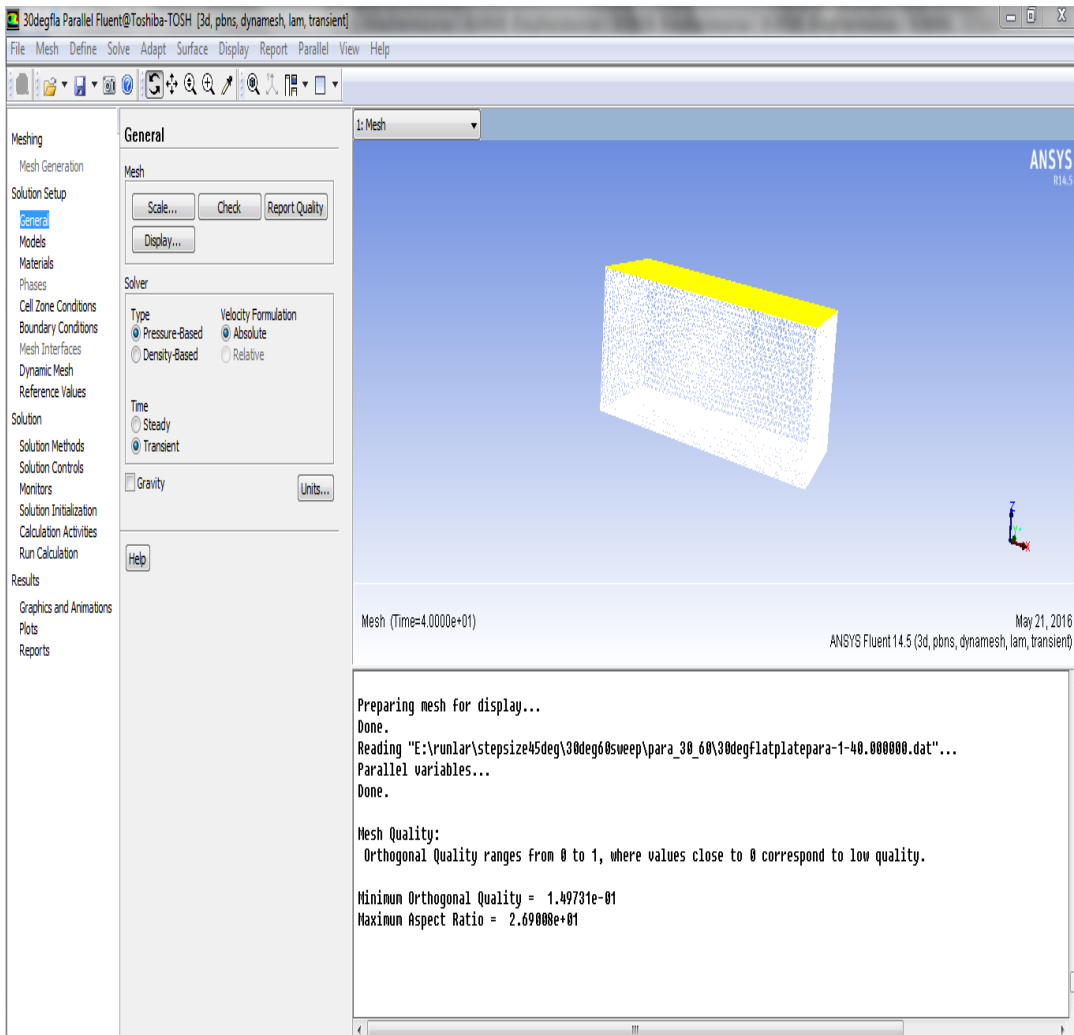
Figure 3.6:Zoom view of the mesh on the wing

Figure 3.7: ANSYS-Fluent Report Quality

Minimum orthogonality=1.49731e-1

The figure is taken from fluent software program (Figure 3.7). When the orthogonality is close to zero mesh quality is low and minimum orthogonality of this study is close to 0.7 so the mesh quality is good.

3.4 CFD Analysis of Flapping Wing Flows

In this section, details of the numerical approach used is described for the flapping wing at $5^0, 30^0, 45^0$ pitch angles with 30^0 and 60^0 sweeping angles.

3.4.1 Numerical Simulations

Computational Fluid Dynamics (CFD) is the analysis of systems by using computer based simulation. For analysis some CFD codes are used which are numerical algorithms that can tackle with fluid problems. In CFD analysis the equations used are conservation of mass (continuity equation), conservation of momentum and conservation of energy. These equations are used for complex situations which are not solved with analytical method. By using numerical methods CFD solves the equations in a discretized domain.

3.4.2 Fluent Solver

In the current study, ANSYS Fluent 14.0 [15] is used to solve unsteady, laminar, 3D Navier-Stokes equations. Finite Volume Method (FVM) is one of the tecnique used in CFD and it is a method by evaluating partial different equations. Values are calculated at discrete places on a meshed geometry. Firstly, the domain is divided into a number of control volumes (cells,elements). Then, differential form of governing equations is integrated over each control volume.

Computation domain is divided into discrete volumes and these governing equations are integrated on these control volumes. Two different solver is used in the Fluent solver as pressure based and density based. In the current study, pressure based solver is used to solve the problem. Two algorithms can be used for pressure based solver. One of them is segregated algorithm where the governing equations are solved sequentially. The other is coupled algorithm. The current problem is solved with a coupled system of equations which involve momentum equations and pressure based equation.

Implicit second order method used for the simulations. It is a method which is used in numerical analysis for obtaining numerical solutions of time-dependent ordinary and partial different equations. Implicit methods find a solution by solving an equation involving both the current state of the system and the later one.

The results are obtained by using unsteady, laminar Navier-Stokes equations. The flapping motion is defined by use of a User Defined Subroutine (UDF)

3.4.3 Governing Equations and Boundary Condition

To analyze flows around the flapping plate at low Reynolds number regime, the three-dimensional Navier-Stokes equations are chosen as governing equations for incompressible, laminar and three dimensional flow.

$$\vec{\nabla} \cdot \vec{V} = 0 \qquad\qquad [3.1]$$

$$\frac{\partial \vec{V}}{\partial t} + (\vec{V} \cdot \nabla)\vec{V} = -\frac{1}{\rho}\nabla p + \nu\nabla^2\vec{V} \qquad [3.2]$$

where $\vec{V}$ is the velocity vector, ρ is the fluid density, p is the pressure, ν is the kinematic viscosity.

ANSYS Fluent software program is used for numerical investigation. The program implements the finite-volume method to solve conservation equations above. The pressure-velocity coupling is done by means of the SIMPLE-type fully implicit algorithm. Pressure-velocity coupling is used with a predictor-corrector pressure scheme. Transient solution has been approximated using second order implicit method. The solution is second-order accurate in space and time. Pressure outlet is used at outer region.

The working fluid is water and the flow field is assumed to be incompressible and laminar. The governing equations are time dependent incompressible Navier- Stokes equations. The flow variables in the computational domain during the cyclic plunge motion of a flat plate are solved with the FLUENT commercial software based on the control volume method. Transient pressure-based solver is selected due to the flow field is assumed as incompressible unsteady flow. To model the flapping motion of flat plate , dynamic mesh method is used. The dynamic motion of flat plate was dominated by external User Defined Functions (UDFs complied with matlab program) during oscillated flapping motion with various stroke amplitudes and frequencies. Water tank walls, water surface and wing surfaces are taken as wall boundary conditions.

3. 4.4 Wing Kinematics

In present analysis, the kinematics of flat plate is defined as two rotations associated with flapping motion.
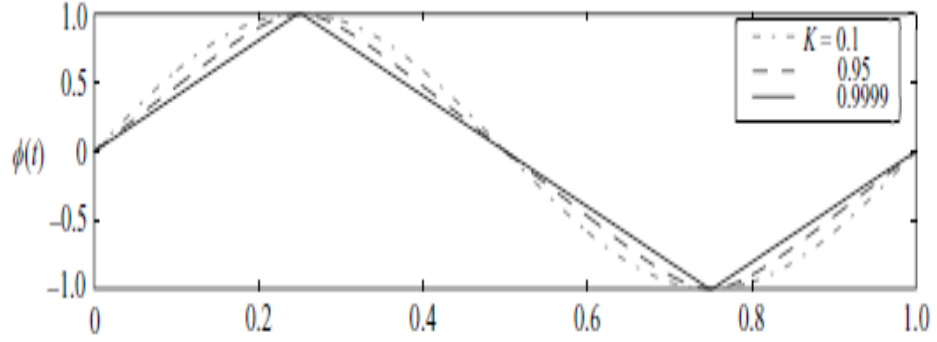

Figure 3.8: Sweeping motion plot [53]

In literature, there are different models used. A model proposed by Berman and Wang to describe the sweeping motion for hovering flight(Figure 3.8):

$$\emptyset_{(t)} = \frac{\emptyset_m}{sin^{-1}K} sin^{-1}[Ksin(2\pi ft)] \qquad [3.3]$$

To define movement of flapping wings, it is described as a sinusoidal function;

$$\theta(t) = \theta_m sin(2\pi Nft) + \phi_0 + \theta_0 \qquad [3.4]$$

In the current study, the flow around the flat plate with a chord length of 7.425 cm and   26 cm span is obtained at hover condition performing a sinusoidal sweeping motion.

This sweep motion is given to the wing by a User-Defined Function (UDF). The motion is given with an unsteady sweeping motion as in Eq. (3.5).

$$\theta = A\sin(2\pi ft) \qquad [3.5]$$

where A denotes the sweep angle amplitude which is taken 60º and 120º, f is the wing stroke cycle frequency. In the current study, the frequency is taken to be 0.1

Hz. The pitch angle α is changed as 5º, 30º and 45º and they are taken to be constant during the whole sinusoidal sweeping motion.

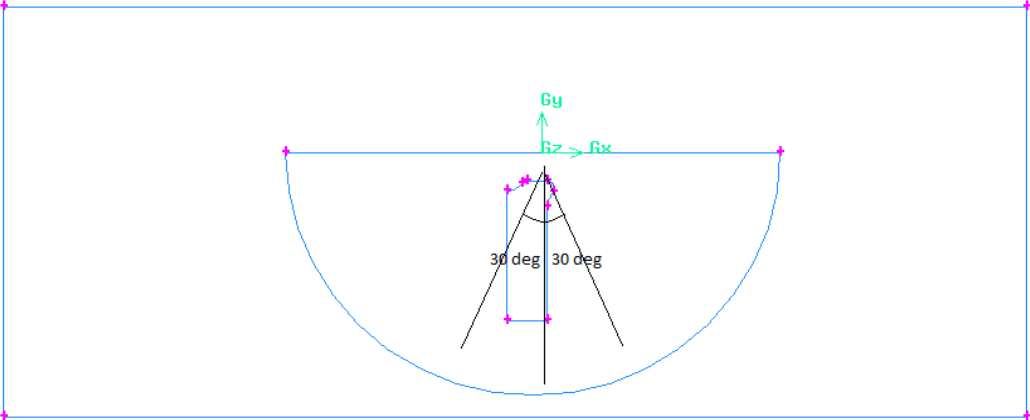Figures 3.9 and 3.10 show sinusoidal sweeping motions of the wing for two different sweeping angle amplitues.

Figure 3.9 : 60º sweep amplitude motion of flat plate $(5^0,30^0,45^0$ pitch angles)

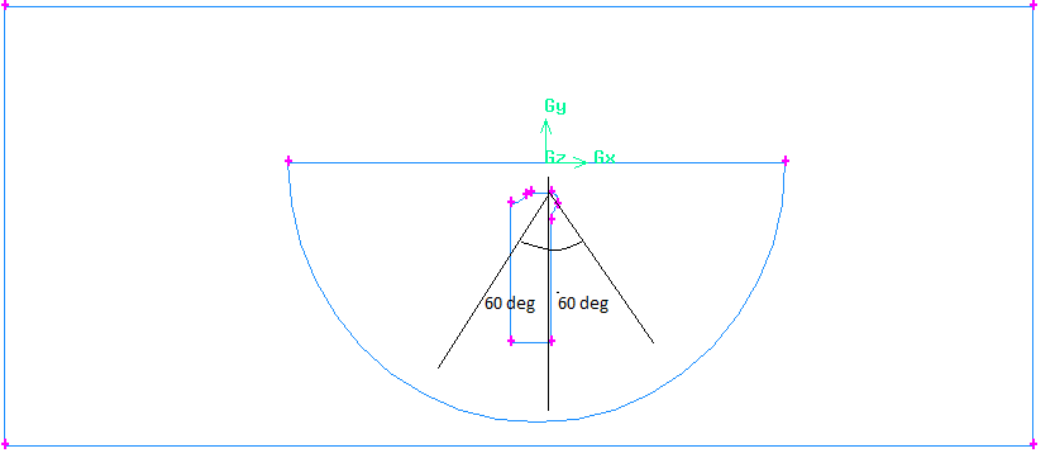Figure 3.10: 120º sweep motion of flat plate $(5^0,30^0,45^0$ pitch angles)

3.4.5 Tip Velocity

Maximum tip velocity is calculated by multiplying amplitude of sweeping angular velocity with span.

$$V = \left|\dot{\theta}\right|\mathrm{b} \qquad\qquad [3.6]$$

$$|\dot{\theta}| = 2\pi fA \qquad\qquad [3.7]$$

where $|\dot{\theta}|$ is the amplitude of sweeping angular velocity, b (26 cm) is the span of flat plate and f is the frequency. A is the sweeping amplitude which is $\pi/3$ (60^0) and $\pi/6$ (30^0) for two amplitudes.

The frequency is f=0.1 Hz and $\theta_1 = 0.327$ and $\theta_2 = 0.657$ rad/s from the angular velocity equation. As a result, the tip velocity is calculated as V_1=0.085 and V_2=0.171 m/s .

The nondimensional time t* is defined as,

$$A = \frac{t}{T} \quad \text{where} \quad T = \frac{1}{f} = 10 \ s \qquad\qquad [3.8]$$

Lift and drg coefficients are calculated with the equations 3.7 and 3.8.

$$C_L = \frac{L}{\frac{1}{2}\rho U^2 S} \qquad\qquad [3.9]$$

$$C_D = \frac{D}{\frac{1}{2}\rho U^2 S} \qquad\qquad [3.10]$$

3.4.6 Reynolds Number

Reynolds' number represents the ratio between inertial and viscous forces. L_{ref} is reference length , U_{ref} is reference velocity and v is kinematic viscosity of fluid.

$$Re_{tip} = \frac{U_{ref} L_{ref}}{\nu} \qquad\qquad [3.11]$$

L_{ref}=0.26 m , U_{ref}=0.085 and 0.171 m/s and at the ambient temperature the viscosity of water is ν=1.10^{-6} m^2/s. The maximum tip Reynolds number is calculated to be 22100 and 44460 for two cases (30^0 and 60^0 sweep angles).

Table 3.1 Reynolds Numbers at different location on the wing

Lref	Uref(30^0 sweep)	Uref(60^0 sweep)	Re(30^0 sweep)	Re(60^0 sweep)
0.26 m	0.085 m/s	0.171 m/s	22100	44460
0.20 m	0.0652 m/s	0.1314 m/s	13040	26280
0.15 m	0.0489 m/s	0.0986 m/s	7335	14790
0.10 m	0.0326 m/s	0.0657 m/s	3260	6570
0.05 m	0.0163 m/s	0.0328 m/s	815	1640

The average Re number for 30^0 sweep angle is 9310 and for 60^0 sweep angle 18748.

From the table, it is seen that Reynolds number increases from root to to tip because of the velocity and it is calculated at five locations.

3.4.7 Grid Refinement Study:

A grid refinement study is conducted to determine an optimal size mesh provide grid independent results.In Figure 3.11 and Figure 3.12 , coarse, fine and medum mesh size results are nearly similar for 30º constant pitch angle and 30 º sweep angle. Therefore, medium mesh size is used for all cases since mesh quality is good. The results are given for time increment of 0.01 s . The wing goes to original point at highest points on curves since the periods are completed and then starts to new period. Because of this, the transient region (from downstroke to upstroke) exists at that points so curve is not smooth at that regions.

Table 3.2: Grid Refinement Study

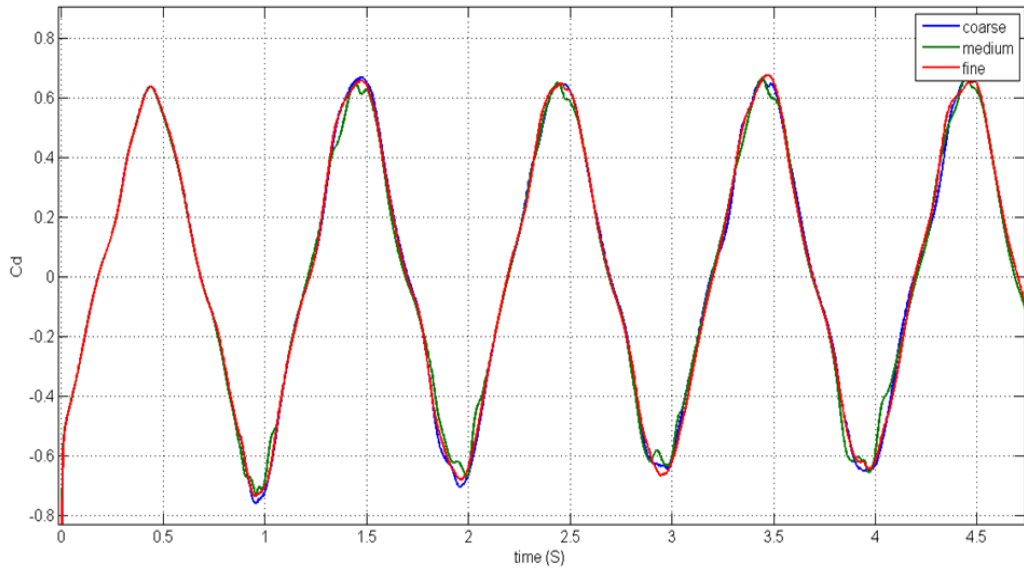|	Coarse Mesh	Medium Mesh	Fine Mesh
Elements	2569791	3926578	4364628
Nodes	462943	678735	746302
Time required	1.5 weeks	2 weeks	3 weeks

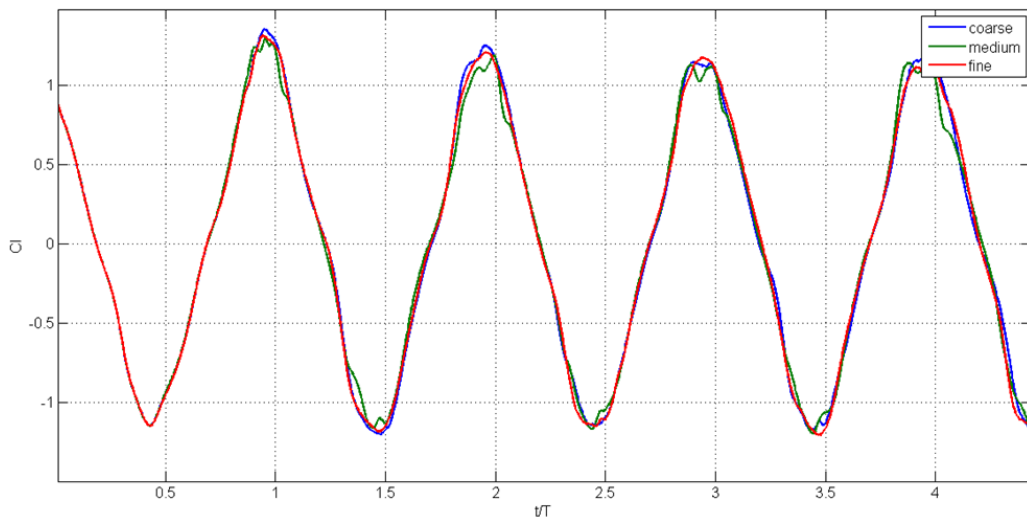Figure 3.11 : Drag coefficient for coarse , medium and fine mesh studies

Figure 3.12 : Lift coefficient for coarse . medium and fine mesh studies

3.4.8 Time Refinement Study:

A time refinement study is conducted to determine a optimal step size to provide time independent results.In Figure 3.13 and Figure 3.14 , 0.01, 0.02 and 0.005 step size results are same for 45º constant pitch angle and 30 sweep angle. Therefore, 0.01 step size and medium mesh are used for all cases investigated current study.
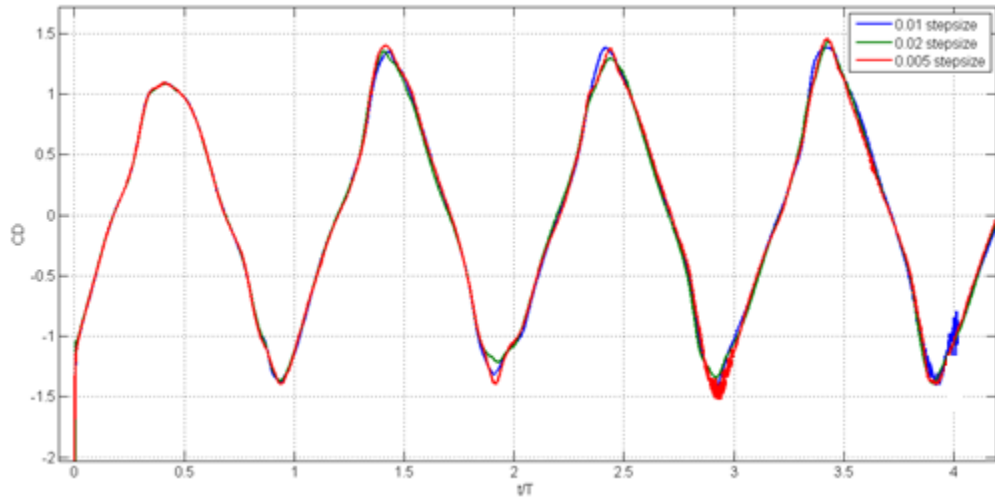
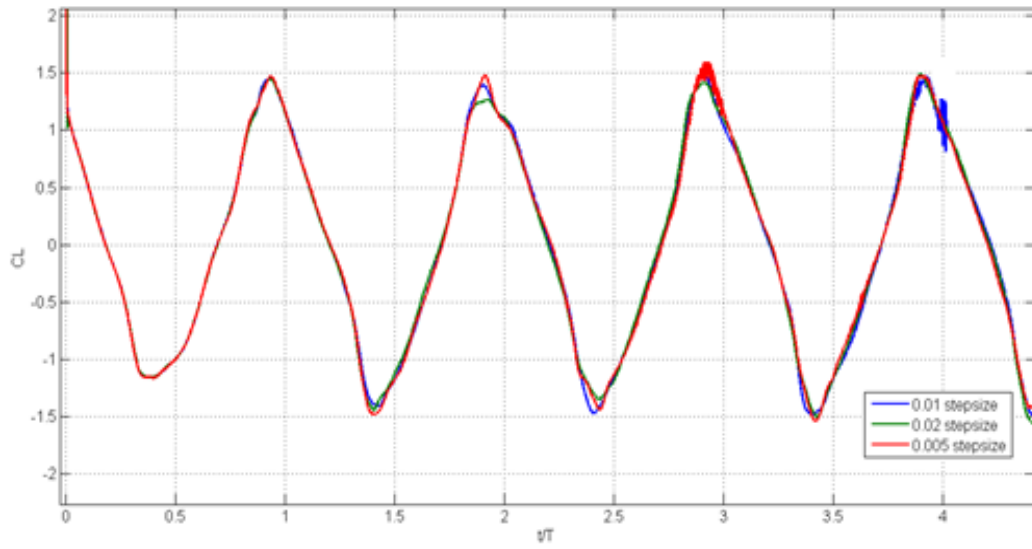Figure 3. 13: Drag coefficient for time refinement studies

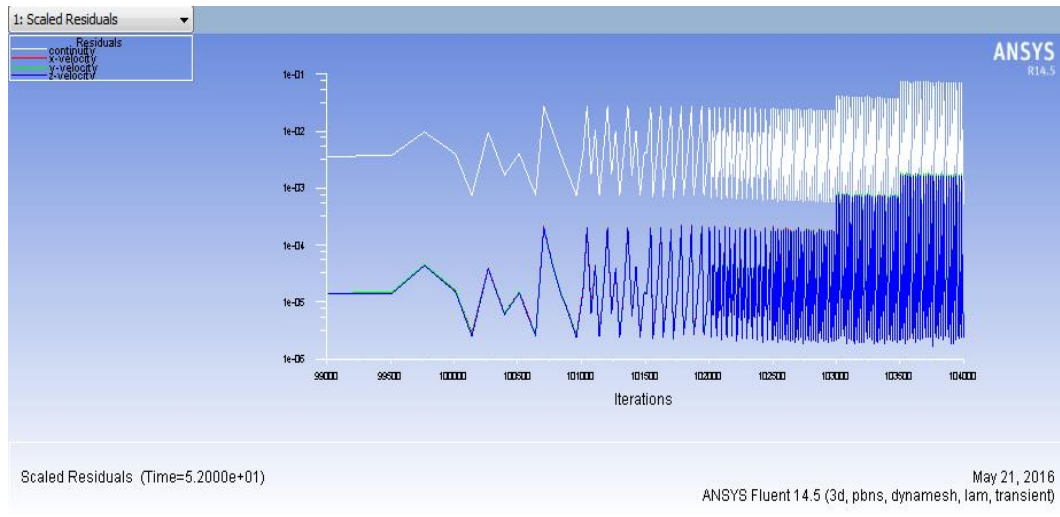Figure 3. 14: Lift coefficient for time refinement studies

Figure 3.15: Scaled Residuals

Scaled residuals show that the investigation is convergent or not. It is seen from the convergence history both velocity and continuity residuals start fluctuating a relatively low values.

CHAPTER 4

RESULTS AND DISCUSSION

4.1 Numerical Results and Discussion:

The unsteady results are investigated for different sweep and pitch angles. The cases that are analyzed are given in Table 4.1. t* is defined as t*=t/T where T is period time (10s) and t is instant time (32 s,33 s,34 s,35 s,36 s,39 s,40 s) Wing position is same at t*=3.2 and 3.3 . Also when t*=3.5 and 4.0 and t*=3.6 and 3.9, wing is same position for two different time points. Inlet conditions are chosen due to the wing dimensions and water properties at the ambient temperature. Velocity for inlet condition is given 1 m/s to start the sweeping motion.

Table 4.1: Inlet Conditions for CFD Simulation

Area(m^2)	0.02
Density (kg/m^3)	998.2
Enthalpy	0
Length(m)	0.26
Pressure (pascal)	0
Tempereture(K)	288.16
Velocity(m/s)	1
Viscosity(kg(m-s)	0.001003
Ratio of specific heats	1.4

Table 4.2. Different Cases

Cases	Pitch Angle, α [°]	Sweep Amplitude, A [°]
Case 1	5	30
Case 2	30	30
Case 3	45	30
Case 4	5	60
Case 5	30	60
Case 6	60	60

In this study, sweeping wing is analyzed at different pitch and sweeping angles numerically. An experiment method was performed at same conditions by Çakır [47]. But order of magnitudes are not consistent because of the inertial forces. The inertial force is a force which considers equal to mass and accelerating object or changing velocity of an object and it relates to Newton's Second Law (Eq. 4.1). In other words, inertial force is acting on the wing owing to the acceleration of flapping mechanism and wing related to exposed motion at the mechanism and wing root.The wing generates aerodynamic forces but in the same time the inertial forces. Flapping mechanism generated only inertial force.

$$F=m.a \qquad\qquad [4.1]$$

The C_L result is plotted in Figure 4.1 for 30^0 pitch angle and 30^0 sweep angle (Case 2) for first period (T=0-10 s , t*/T=0 -1).
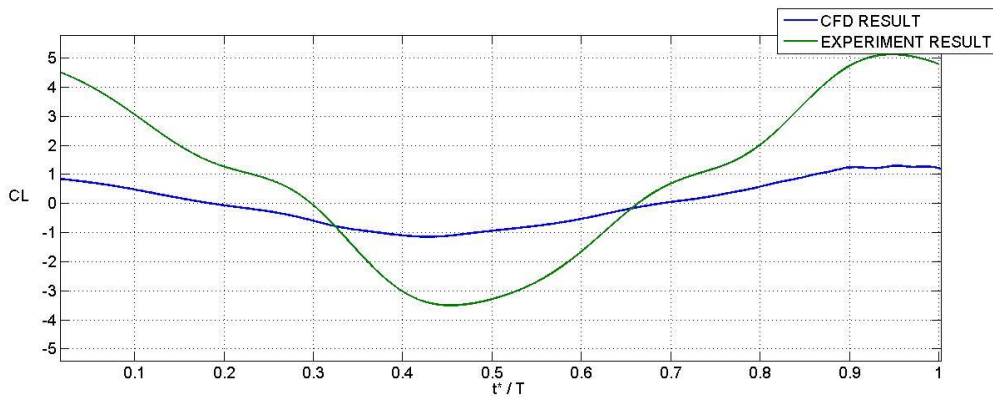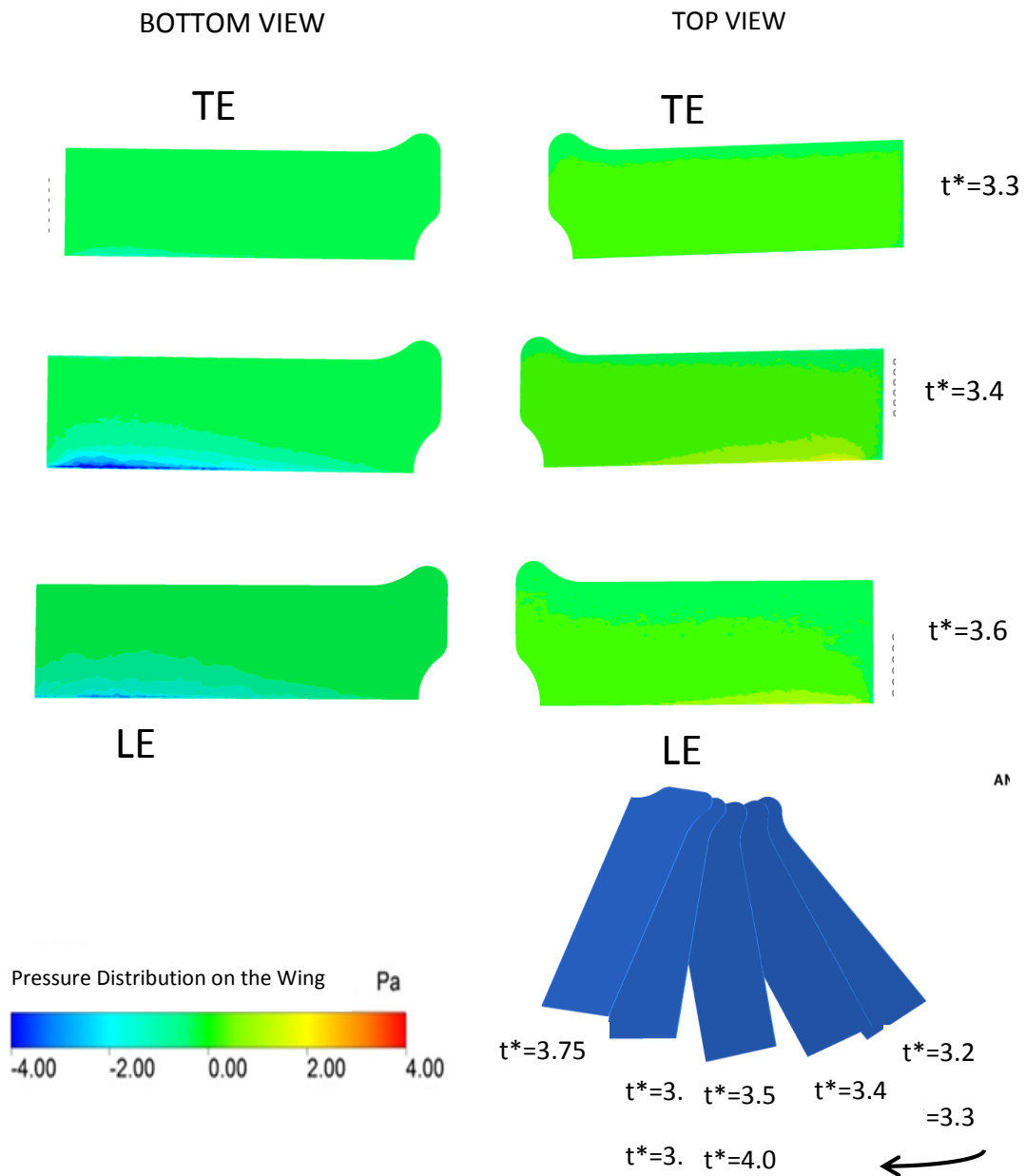

Figure 4.1 : CFD and Experiment Results Comparison

Figure 4.2: Top and bottom views at downstroke of 4th period for Case 1

Figure 4.2 shows pressure distribution at the top and bottom surface of the wing at t^*=3.3, 3.4 , 3.6 at downstroke of the 4th period. The wing pressure contours are plotted from −4 Pa to +4 Pa at given positions. High pressure denotes the red color and suction pressure denotes the blue color. High pressure where C_L (Fgure 4.4) is minimum and C_D (figure 4.5) is maximum is observed at leading edge of the top surface at t^*= 3.6. On the other hand, a suction region is visualized at the bottom

surface of the wing when t* is 3.4. In addition, Figure 4.6 and 4.7 show that the wing goes to original starting point and sweeping velocity is low at that point.
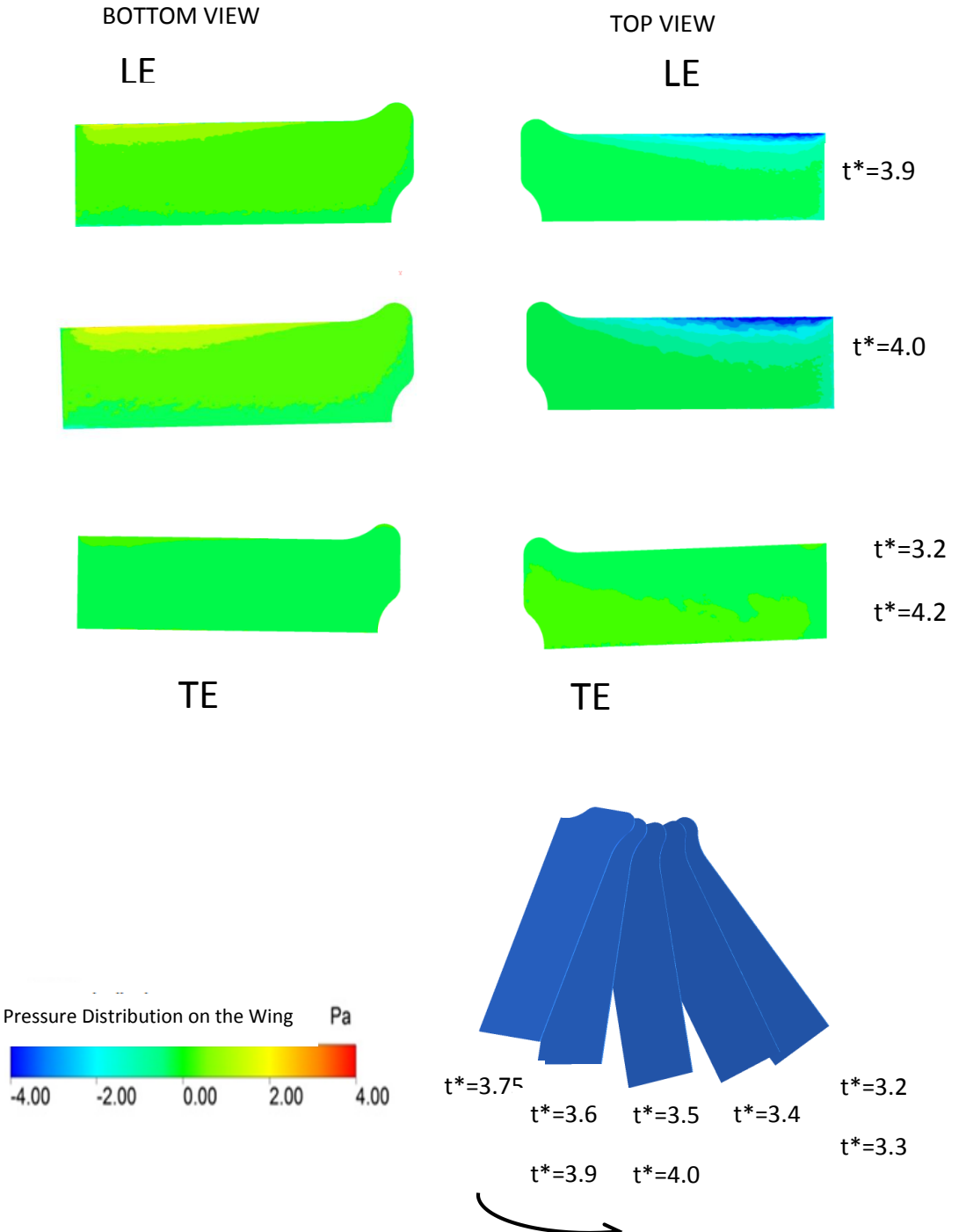
BOTTOM VIEW

TOP VIEW

LE

LE

t*=3.9

t*=4.0

t*=3.2

t*=4.2

TE

TE

Pressure Distribution on the Wing   Pa

-4.00   -2.00   0.00   2.00   4.00

t*=3.75   t*=3.2

t*=3.6   t*=3.5   t*=3.4

t*=3.3

t*=3.9   t*=4.0

Figure 4.3 Top and bottom views at upstroke of 4th period for Case 1

Figure 4.3 shows pressure distribution at the top and bottom surface of the wing at t*=3.9 , 4.0,3.2=4.2 at the upstroke of the 4th period. Suction pressure where C_L (Figure 4.4) is maximum and C_D (Figure 4.5) is minimum is observed at the leading edge of the top surface when t* is 4.0. On the other hand, a high pressure region is

44

visualized at the bottom surface at t*=4.0. In addition, Figures 4.6 and 4.7 show that when t* is equal to 4.0, the wing is in the original point and sweeping velocity is high at that point.
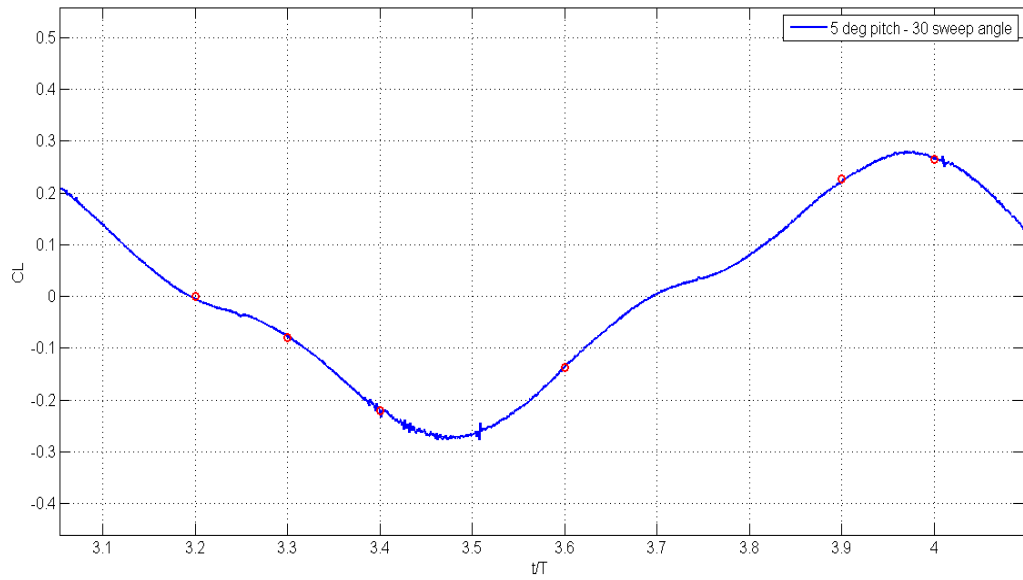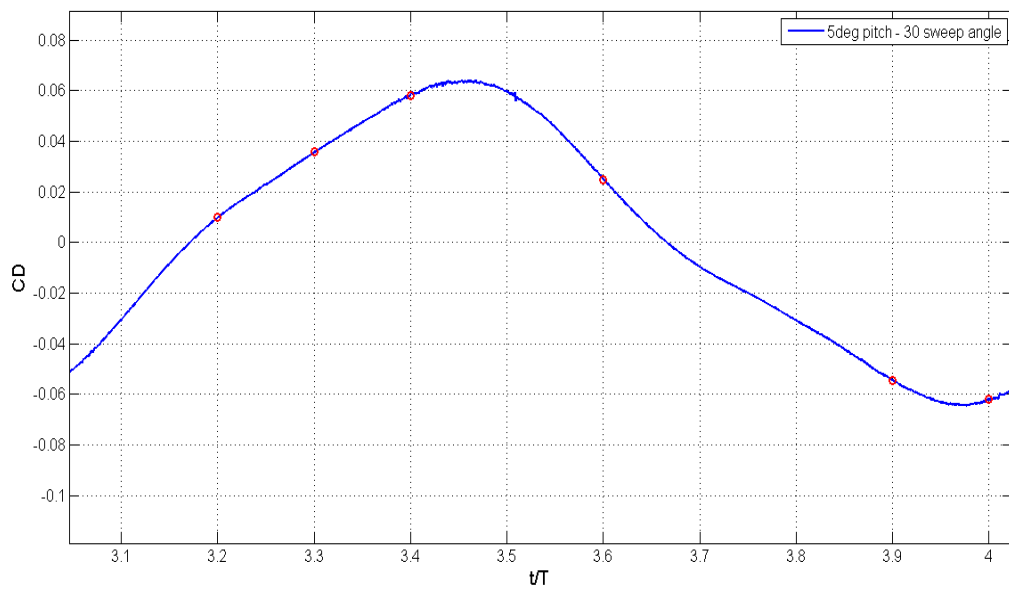

Figure 4.4 Lift coefficient for 4th Period at case 1

Figure 4.5 Drag coefficient for 4th Period at case 1

Figures 4.4 and 4.5 show lift and drag coefficient variations for 5 º pitch angle and 30 º sweep angle at 4th period during upstroke and downstroke motion. According to

plots when C_D is increasing, C_L is decrasing from t*=3.2 to t*=3.4. On the other hand, when C_L is increasing, C_D is decreasing from t*=3.6 to t*=4.0.
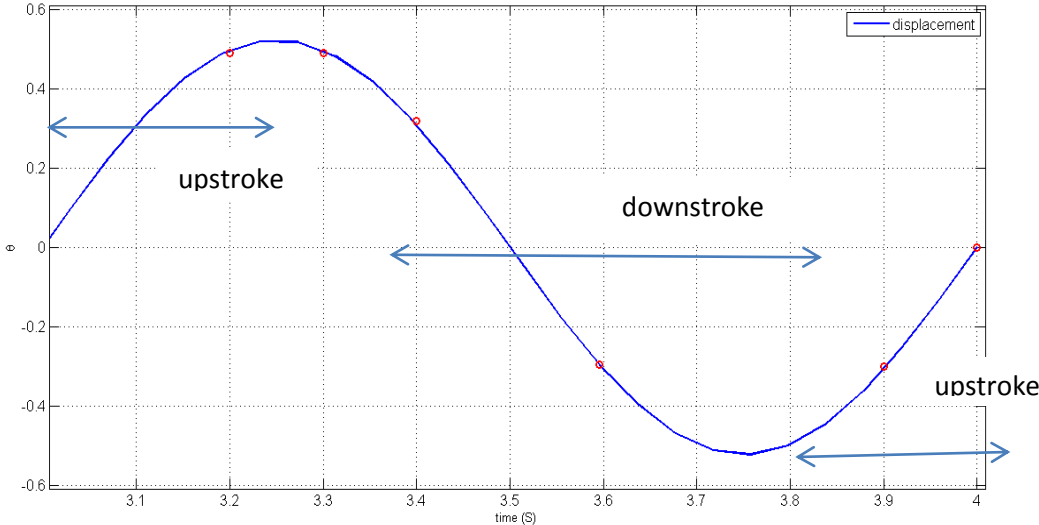

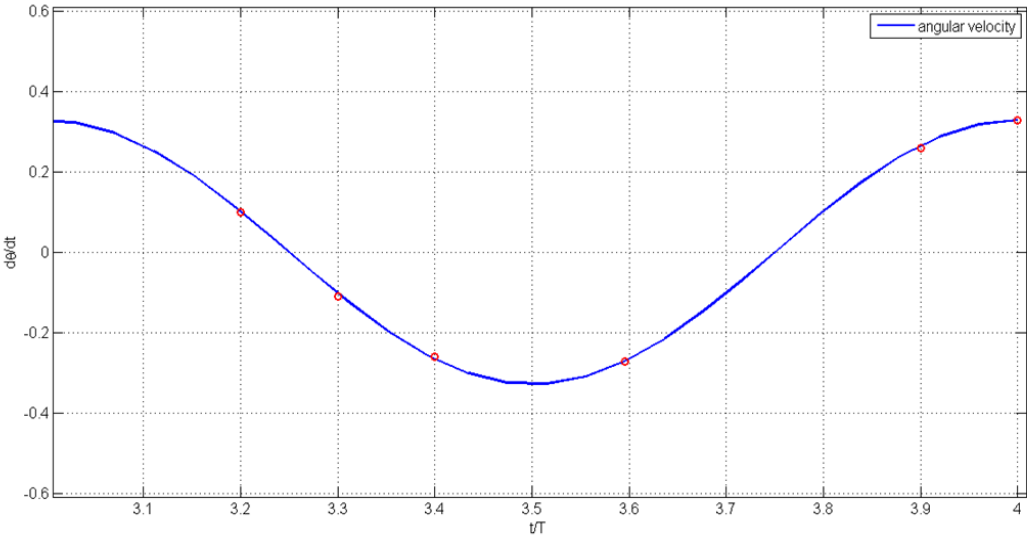Figure 4.6 Angular displacement for 4th Period at case 1

Figure 4.7Angular velocity for 4th Period at case 1

Figures 4.6 and 4.7 show sweeping displacement and velocity at 4th period for Case 1. Figure 4.6   is a sinusoidal function and Figure 4.7 is a cosine function. The sinusoidal and cosine equations for Case 1, Case 2 and Case 3 are given as follows:

$$\theta = 30.\pi/180*\sin(2\pi ft) \qquad\qquad\qquad [4.2]$$

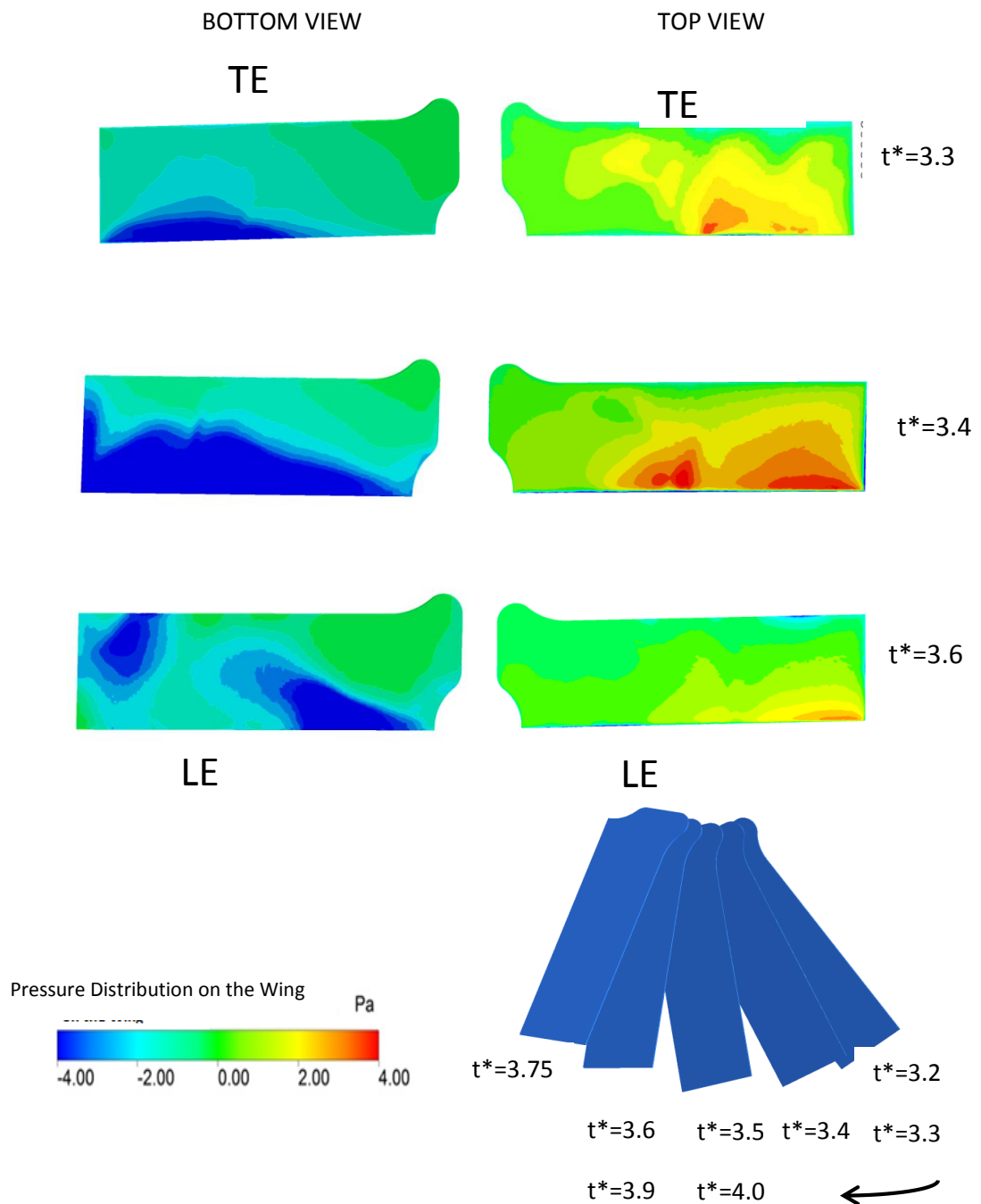$$d\theta/dt = 2\pi f*30.\pi/180*\cos(2\pi ft) \qquad\qquad [4.3]$$

Figure 4.8 Top and bottom views at downstroke of 4th period for Case 2

Figure 4.8 shows pressure distribution at the top and bottom surface of the wing at t*=3.3, 3.4, 3.6 at downstoke of the 4th period for case 2. High pressure where C_L (Figure 4.10) is nearly minimum and C_D (Figure 4.11) is nearly maximum is observed at leading edge of the top surface at t*= 3.4. On the other hand , a suction

region is visualized at the leading edge of the bottom surface of the wing at t*= 3.4. In addition, Figure 4.12 and 4.13 show that the wing goes to original starting point and sweeping velocity is low at that point.
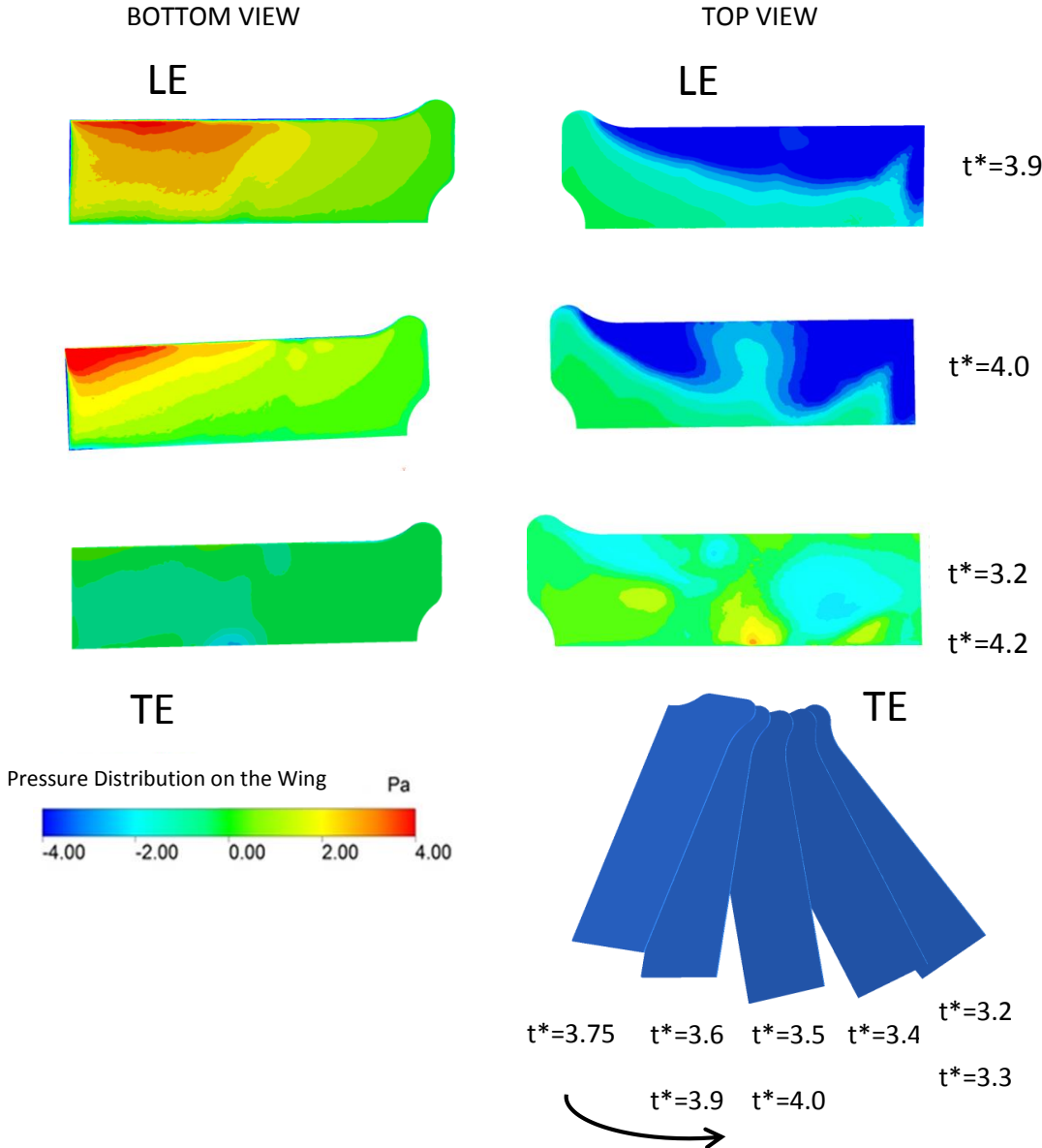

Figure 4.9 Top and bottom views at upstroke of 4th period for Case 2

Figure 4.9 shows pressure distribution at the top and bottom surface of the wing at t*=3.9, 4.0, 3.2=4.2 at upstoke of the 4th period. Suction pressure where C_L (Figure 4.10) is nearly maximum and C_D (Figure 4.11) is nearly minimum is observed at leading edge of the top surface and center of the wing surface at t*= 4.0. On the other hand, a high pressure region is visualized at the bottom surface at leading edge of the wing at t*= 4.0. Because fluid flows over the leading edge of the wing for the first time and the effect of the fluid effect is dominant at that region. When the flow cross

48

over the leading edge, a shock wave can be occured and for this reason pressure effect can be dominant at that region. Then at t*=4.2 wing goes from upstroke position to the downstroke position. So a transient region can be observed at that point. In addition, Figures 4.12 and 4.13 show that at t*=4.0, the wing is in the original point and sweeping velocity is high at that point.
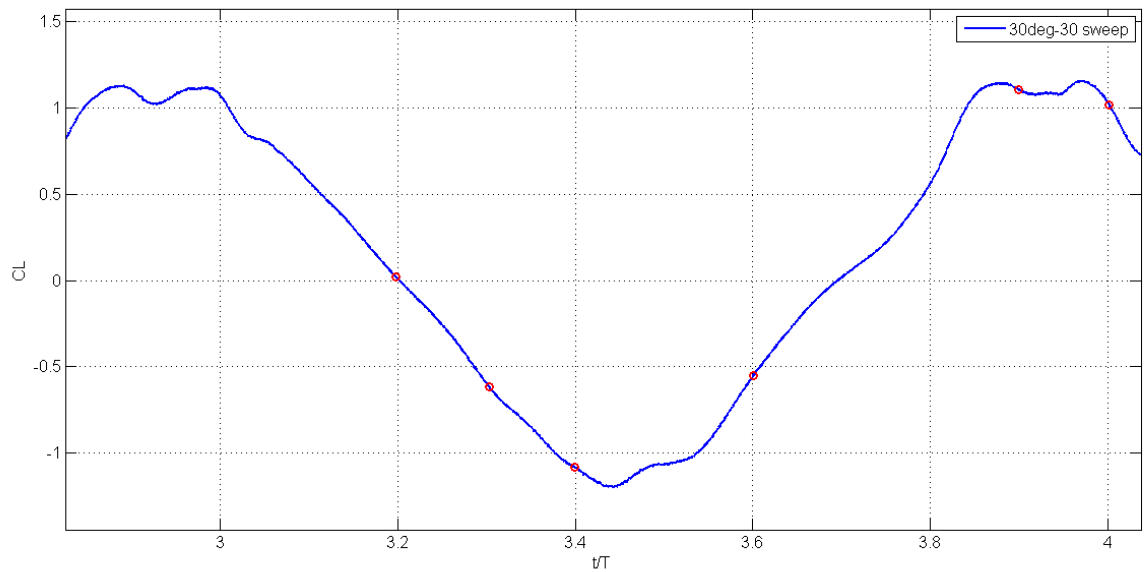

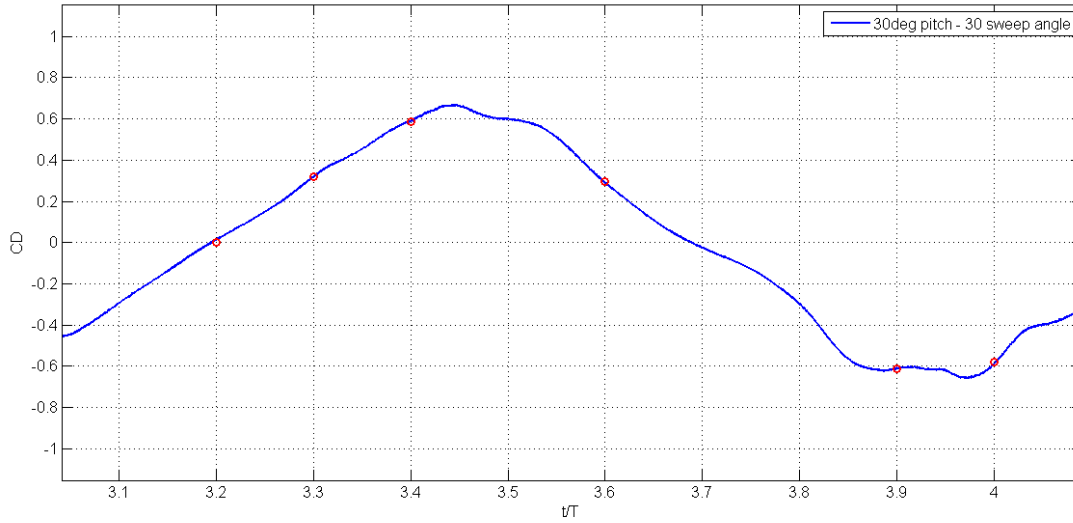Figure 4.10: Lift coefficient for 4th Period at case 2

Figure 4.11: Drag coefficient for 4th Period at case 2

Drag coefficient and lift coefficients are plotted for 4th Period at case 2 . Figures 4.10 and 4.11 show lift and drag coefficient variations for 5º pitch angle and 30º sweep angle at 4th period during upstroke and downstroke. According to plots when C_D is increasing , C_L is decrasing from t*=3.2 to t*=3.4 . On the other hand , when C_L is increasing, C_D is decreasing from t*=3.6 to t*=4.0.
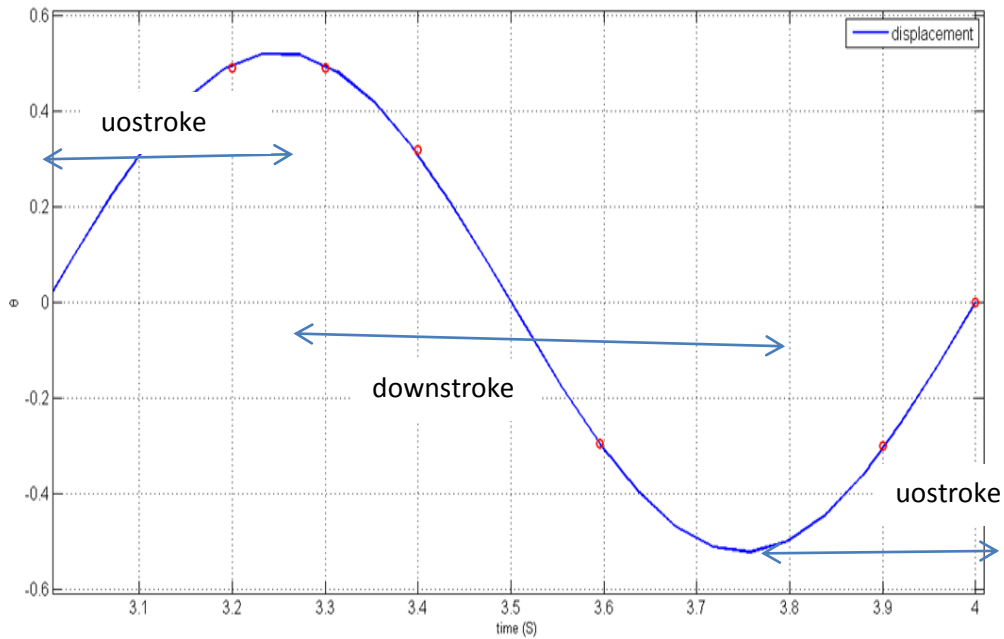

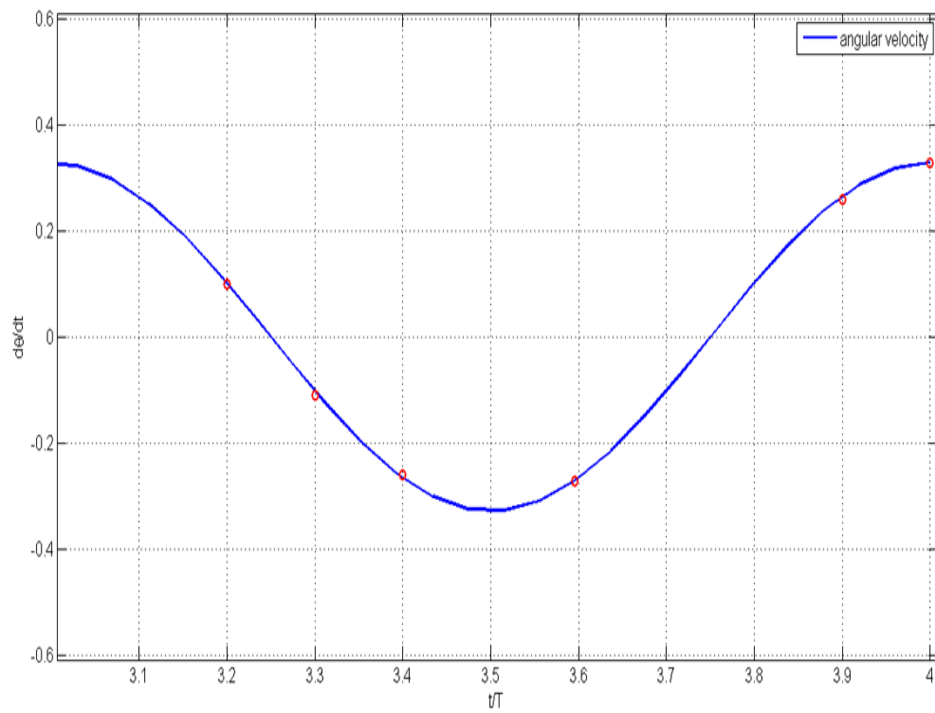Figure 4.12: Sweeping position for 4th Period at case 2

Figure 4.13: Sweeping velocity for 4th Period at case 2

Figure 4.12 and 4.13 show sweeping displacement and velocity at 4th period for Case 2. Figure 4.12 is a sinusoidal function and figure 4.13 is a cosine function.
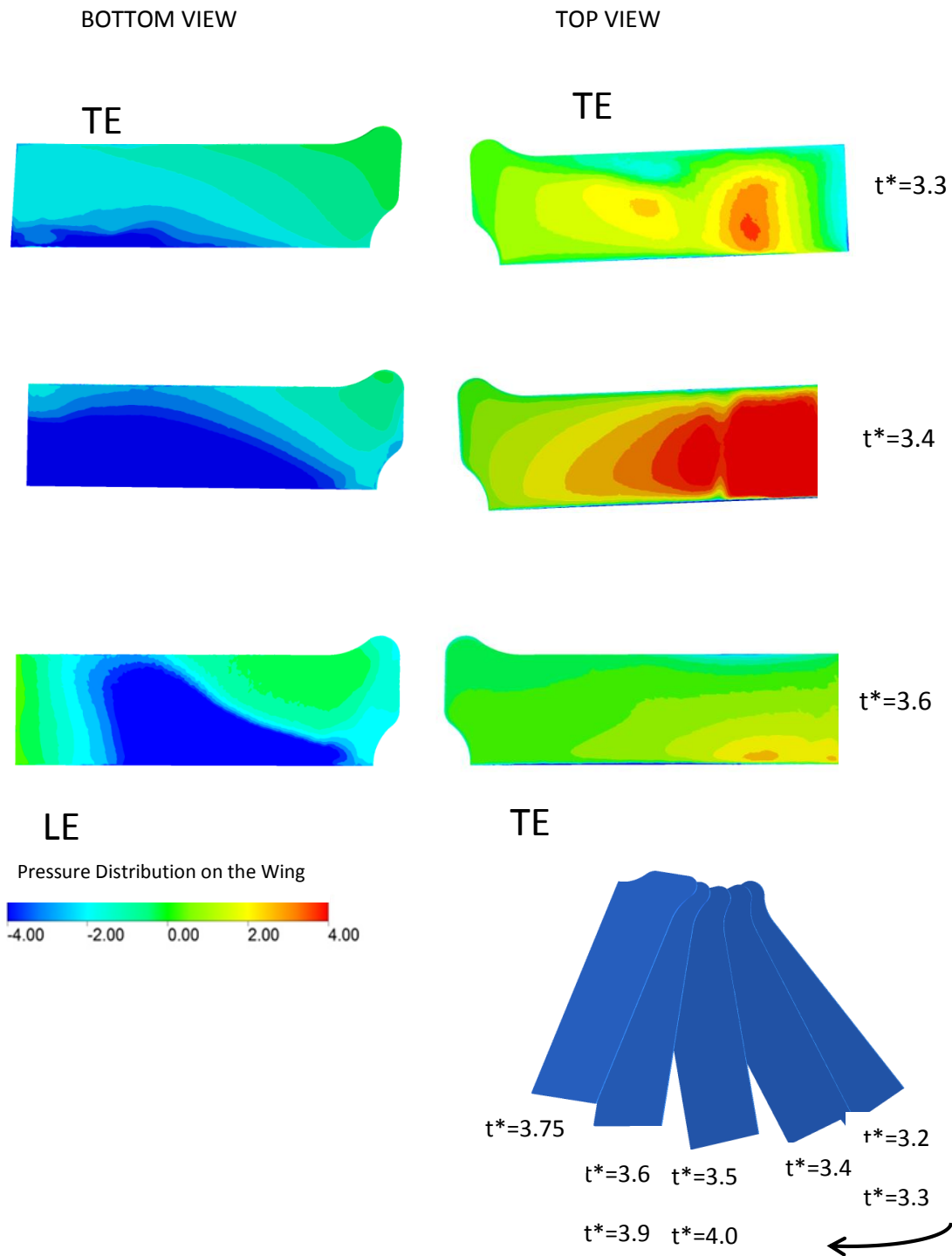
Figure 4.14: Top and bottom views at downstroke of 4th period for Case 3

Figure 4.14 shows pressure distribution at the top and bottom surface of the wing at t*=3.3, 3.4, 3. at downstroke of the 4th period for case 3. High pressure where C_L (Figure 4.16) is nearly minimum and C_D (Figure 4.17) is nearly maximum is observed at a location close to the wing tip of the top surface at=3.4. On the other hand , a suction region starts from at t*=3.3 at leading edge and grows to center at

the bottom surface at t*=3.4. Pressure is starting to decrease at t*3.6. In addition, Figures 4.18 and 4.19 show that the wing goes to original starting point and sweeping velocity is low at that point.
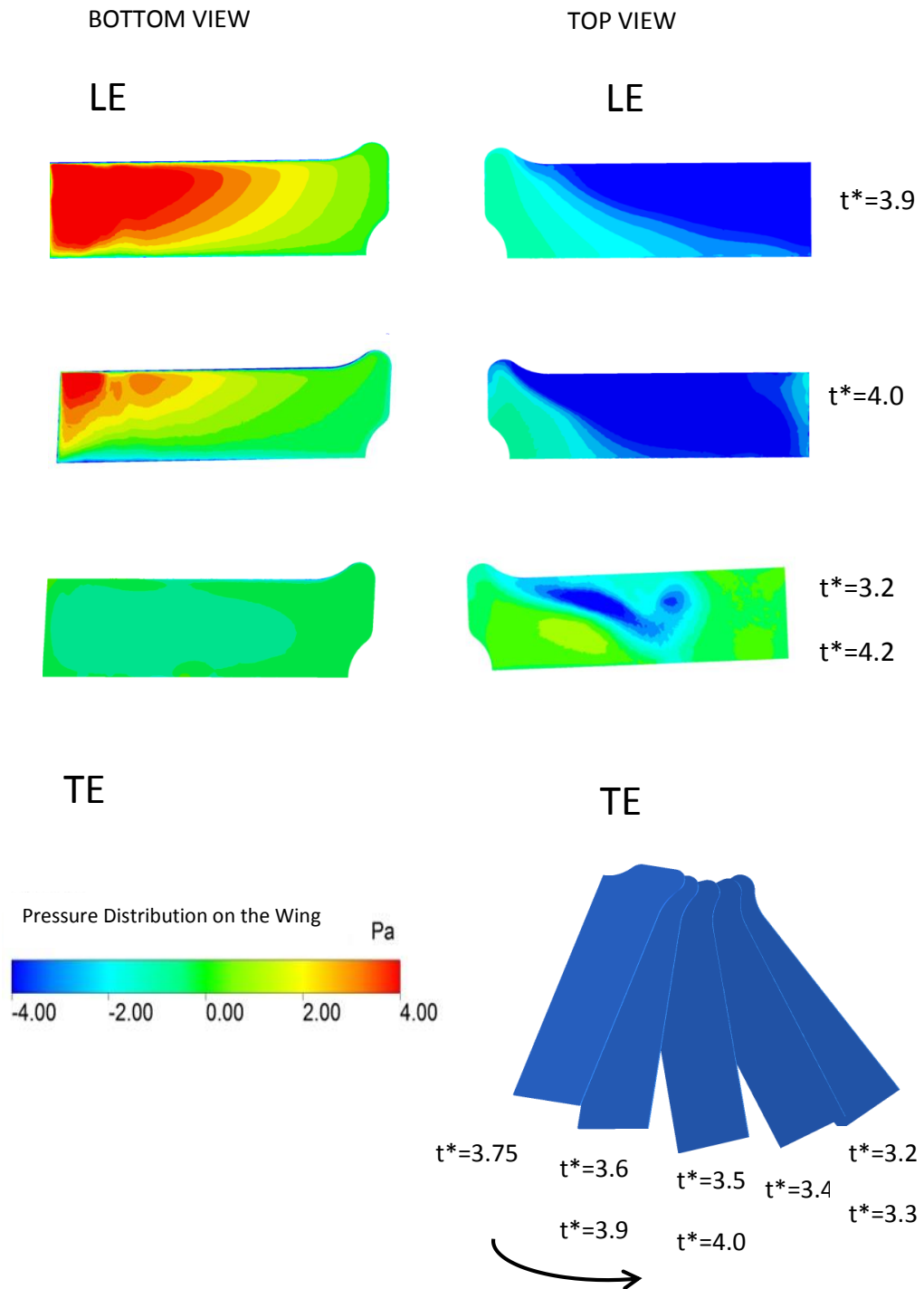

Figure 4.15:Top and bottom views at upstroke of 4th period for Case 3

Figure 4.15 shows pressure distribution at the top and bottom surface of the wing at t*=3.9, 4.0, 3.2=4.2 at upstroke of the 4th period. Suction pressure where C_L (Figure 4.16) is nearly maximum and C_D (Figure 4.17) is nearly minimum is observed at a large area of the wing which is close to leading edge of the top surface at t*=4.0. On the other hand, a high pressure region is visualized that is starts from leading edge of the bottom surface at t*=3.9 and grows to the center of the wing when t* is equal to 4.0. The reason is because fluid cross over the leading edge of the wing and the effect of the pressure is dominant due to the shock wave propagation. At t*=3.2, pressure enters the transition region. In addition, Figures 4.18 and 4.19 shows that at t*=4.0, the wing is in the original point and sweeping velocity is high at that point.
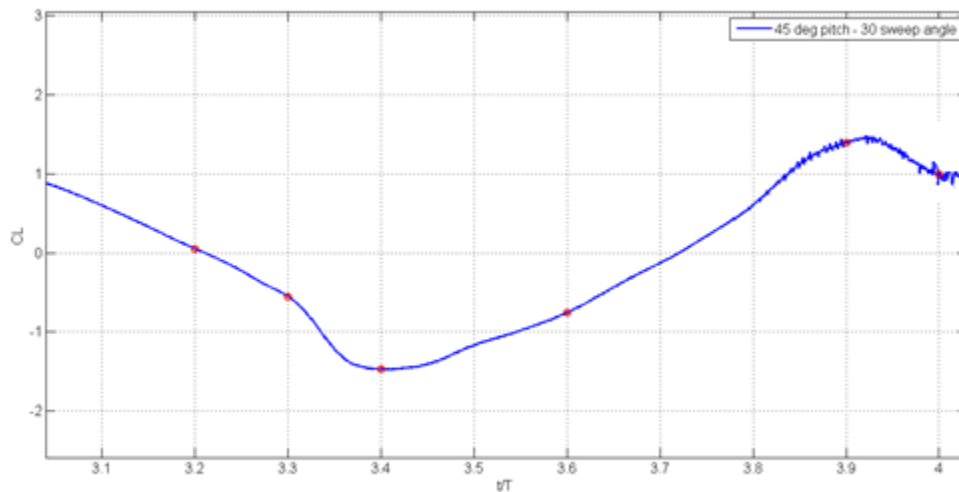

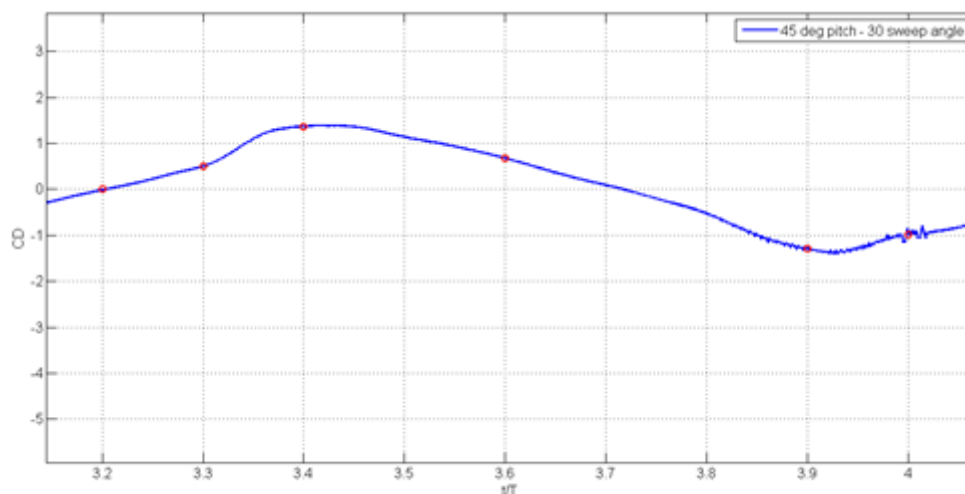Figure 4.16:Lift coefficient for 4th Period at case 3

Figure 4.17: Drag coefficient for 4th Period at case 3

Drag coefficient and lift coefficients are plotted for 4th Period at case 2 . Figures 4.16 and 4.17 show lift and drag coefficient variations for 45 º pitch angle and 30 º sweep angle at 4th period during upstroke and downstoke. According to plots when C_D is increasing , C_L is decreasing when t* is equal to 3.2 to t*=3.4. On the other hand , when C_L is increasing, C_D is decreasing from t*=3.6 to t*=4.0. The coefficients are opposite each other.
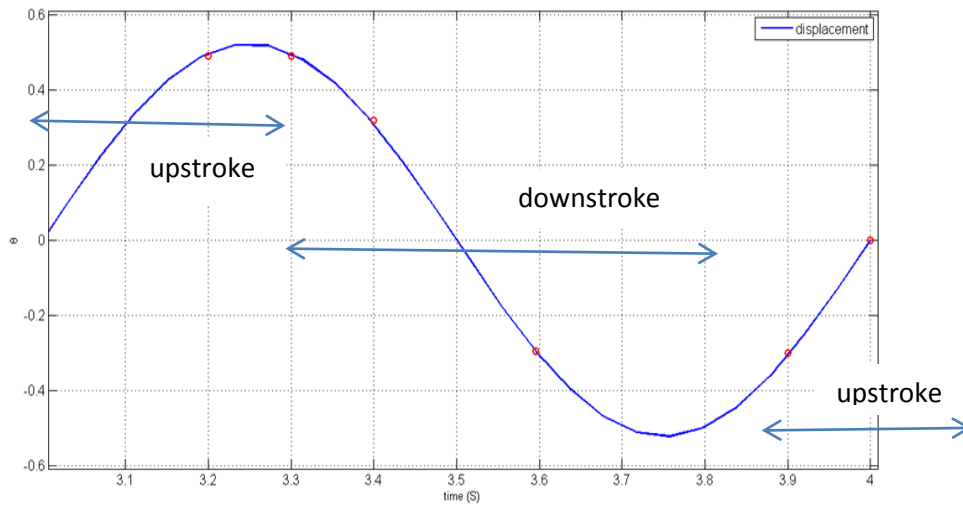

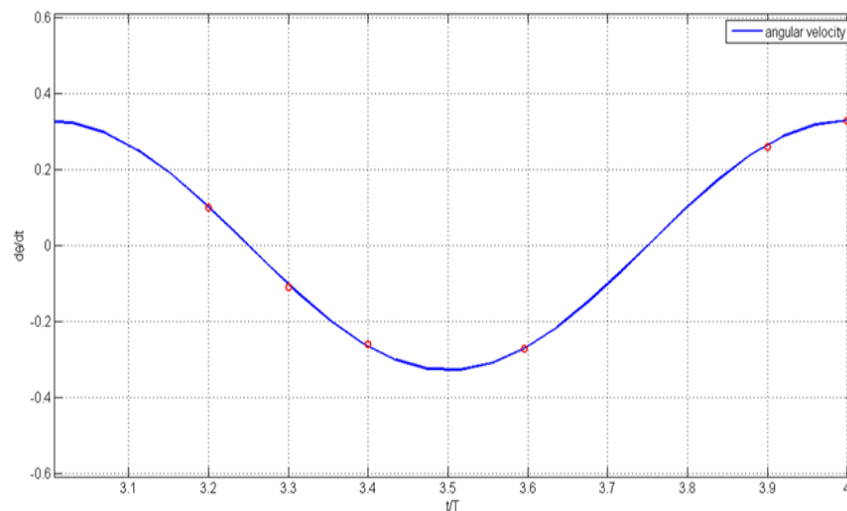Figure 4.18: Sweeping position for 4th Period at case 3

Figure 4.19: Sweeping velocity for 4th Period at case 3

Figure 4.18 and 4.19 show sweeping displacement and velocity at 4th period for Case 3. Figure 4.18 is a sinusoidal function and Figure 4.19 is a cosine function. When the plots are observed, the sweeping position and velocity can be investigated by looking these plots.
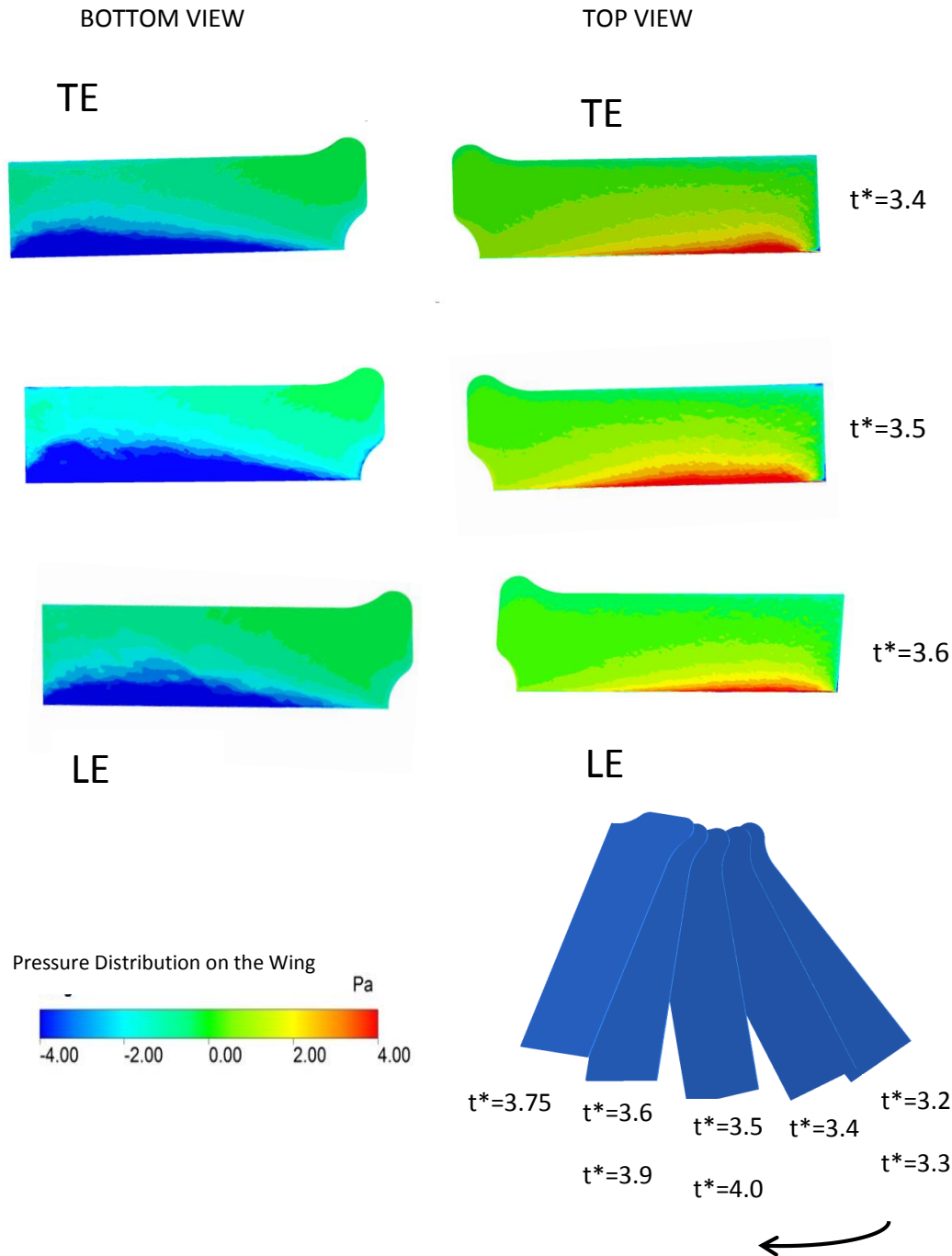
Figure 4.20: Top and bottom views at downstroke of 4th period for Case 4

Figure 4.20 shows pressure distribution at the top and bottom surface of the wing when t* is equal to 3.4 , 3.5 and 3.6 positions at downstroke of the 4th period when sweeping amplitude 120 ^{0}. The wing pressure contours are plotted from –4 Pa to +4 Pa at given positions. High pressure is maximum where C_L (Figure 4.22) is minimum and C_D (Figure 4.23) is maximum and it is observed that is started from leading edge of the wing at t*= 3.4 and grows to center of the top surface at t*= 3.5

position. At t*=3.6, pressure effect starts to decrease when C_D starts to decrease. On the other hand , a suction region is visualized at the bottom surface at t*=3.5. In addition, Figures 4.24 and 4.25 show that the wing is in original starting point and sweeping velocity is minimum at that point.

BOTTOM VIEW   TOP VIEW

LE   LE

t*=3.9

t*=4.0

t*=3.2
t*=4.2

TE   TE

Pressure Distribution on the Wing   Pa

-4.00   -2.00   0.00   2.00   4.00

t*=3.75   t*=3.6   t*=3.2
                        t*=3.5   t*=3.4
            t*=3.9   t*=3.3
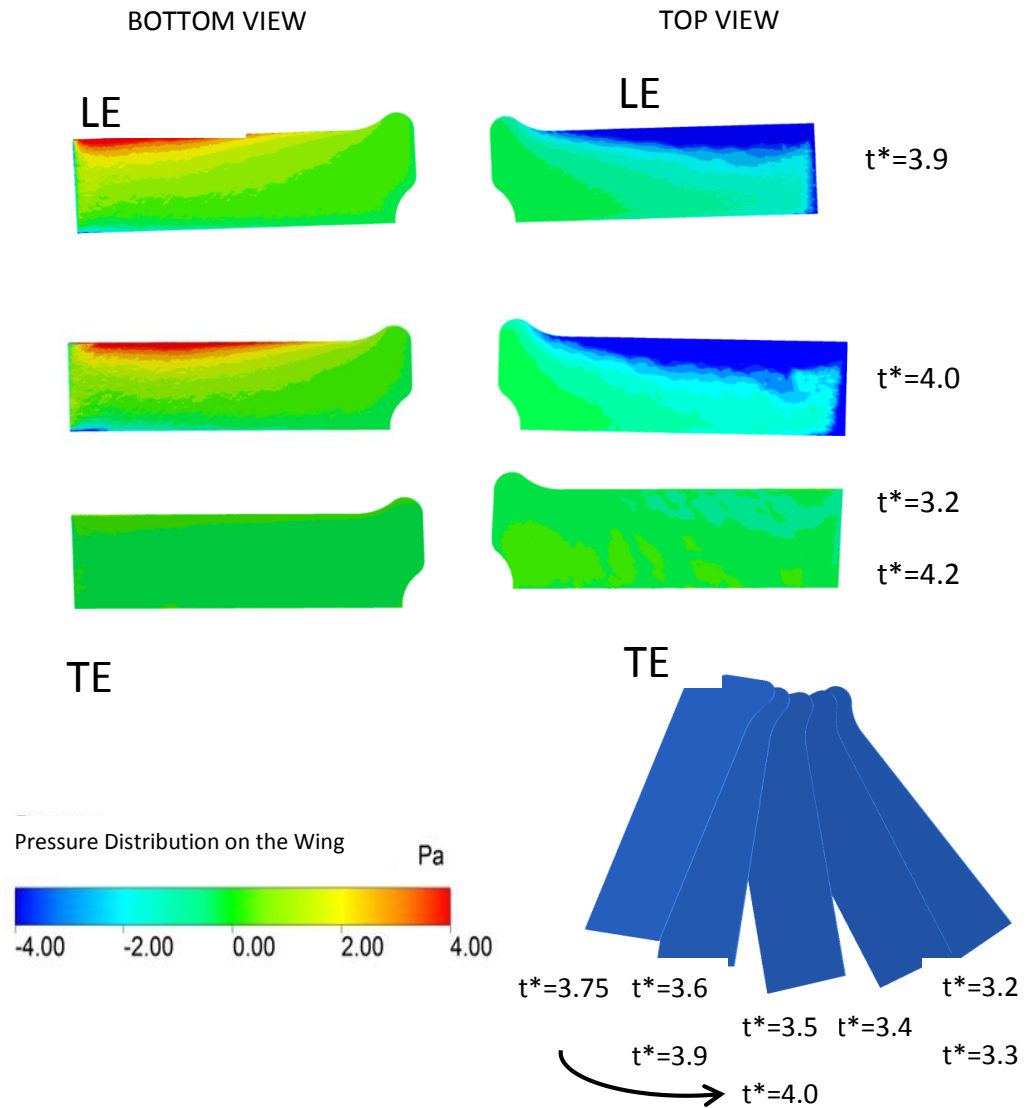   t*=4.0

Figure 4.21: Top and bottom views at upstroke of 4th period for Case 4

Figure 4.21 shows pressure distribution at the top and bottom surface of the wing at t*=3.9 , 4.0 , 3.2=4.2 at upstoke of the 4th period. Suction pressure is visualized where C_L (Figure 4.22) is nearly maximum and C_D (Figure 4.23) is nearly minimum is observed at leading edge of the bottom surface at t*=3.9 and grows at t*=4.0. Because fluid flows over the leading edge of the wing initially, the pressure effect can be observed dominantly at that region when the fuid molecules collide the

surface of the leading edge with a velocity. After the collision velocity of fluid molecules start to decrease so the pressure effect also decreases. On the other hand, a high pressure region is visualized that is starts from leading edge of the bottom surface at t*=3.9 and grows at t*= 4.0. At t*=3.2=4.2 wing position changes from upstroke to downstroke positon. So a transient region is observed at that point. In addition, Figures 4.24 and 4.25 show that at t*=4.0, the wing is in the original point and sweeping velocity is maximum at that point.
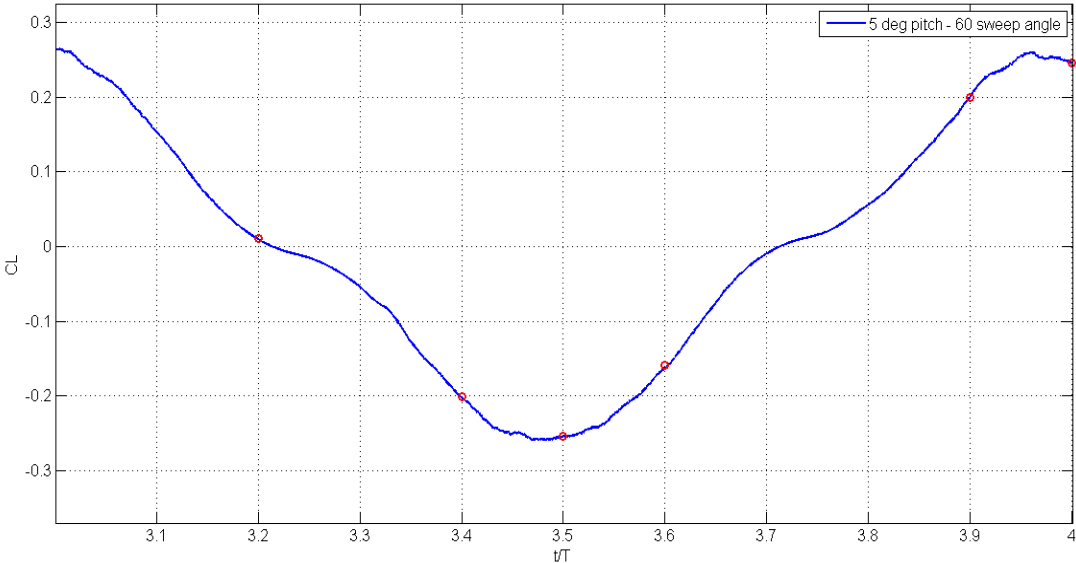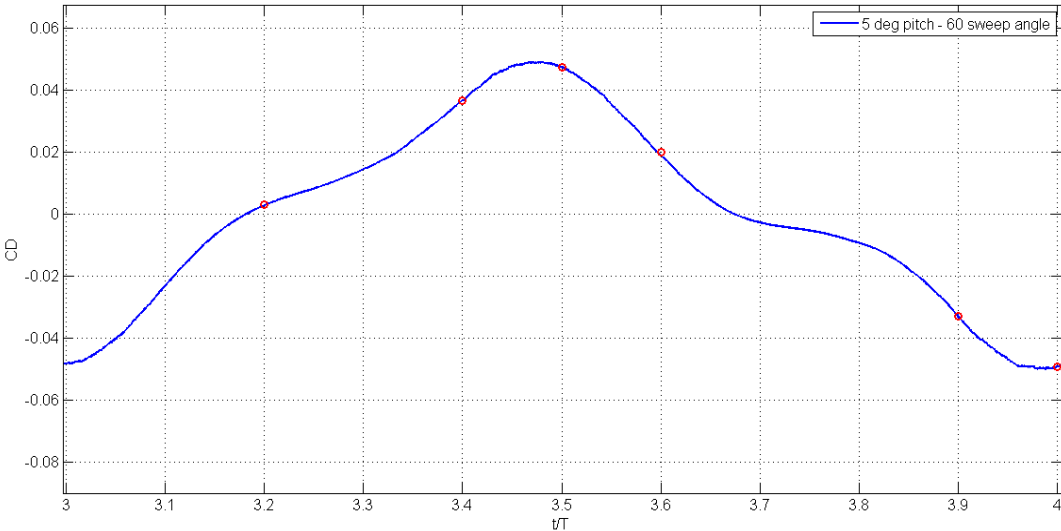

Figure 4.22: Lift coefficient for 4th Period at case 4

Figure 4 23: Drag coefficient for 4th Period at case 4

58

Drag coefficient and lift coefficients are plotted for 4th Period at case 4 . Figures 4.22 and 4.23 show lift and drag coefficient variations for 5^0 pitch angle and 60^0 sweep angle at 4th period during upstroke and downstroke motion. According to plots when C_D is increasing , C_L is decreasing from $t*=3.2$ to $t*=3.5$ positon. On the other hand , when C_L is increasing, C_D is decreasing from $t*=3.6$ to $t*=4.0$. The coefficients are opposite the each other.
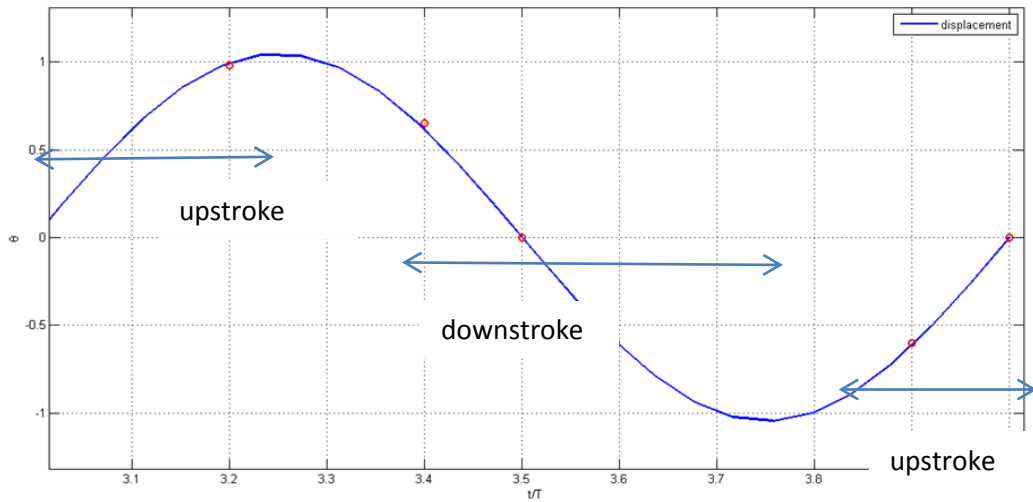

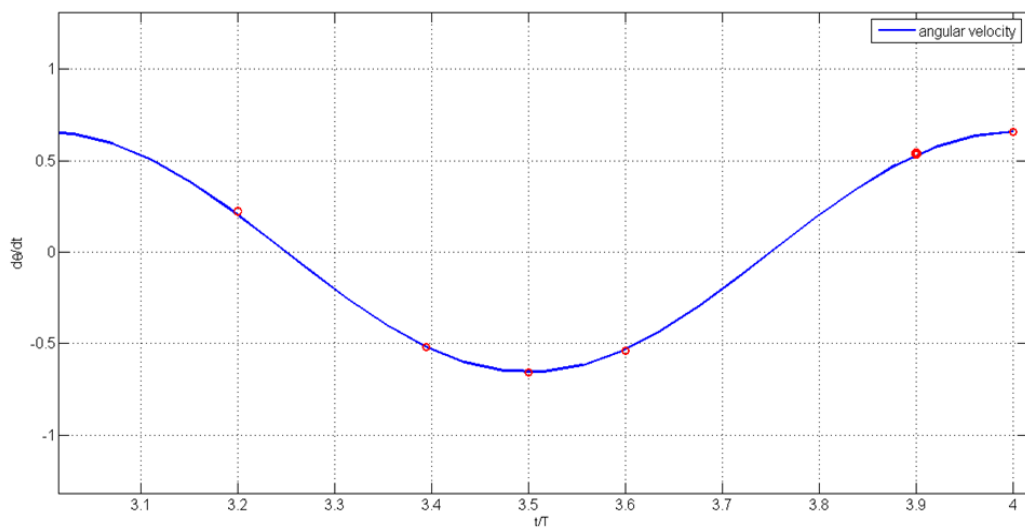Figure 4.24: Sweeping position for 4th Period at case 4

Figure 4.25: Sweeping velocity for 4th Period at case 4

Figure 4.24 and 4.25 shows sweeping displacement and velocity at 4th period for Case 4. Figure 4.24 is a sinusoidal function and Figure 4.25 is a cosine function. The equations of plots are shown as follows:

$$\theta = 60.\pi/180*\sin(2\pi ft) \qquad\qquad [4.4]$$

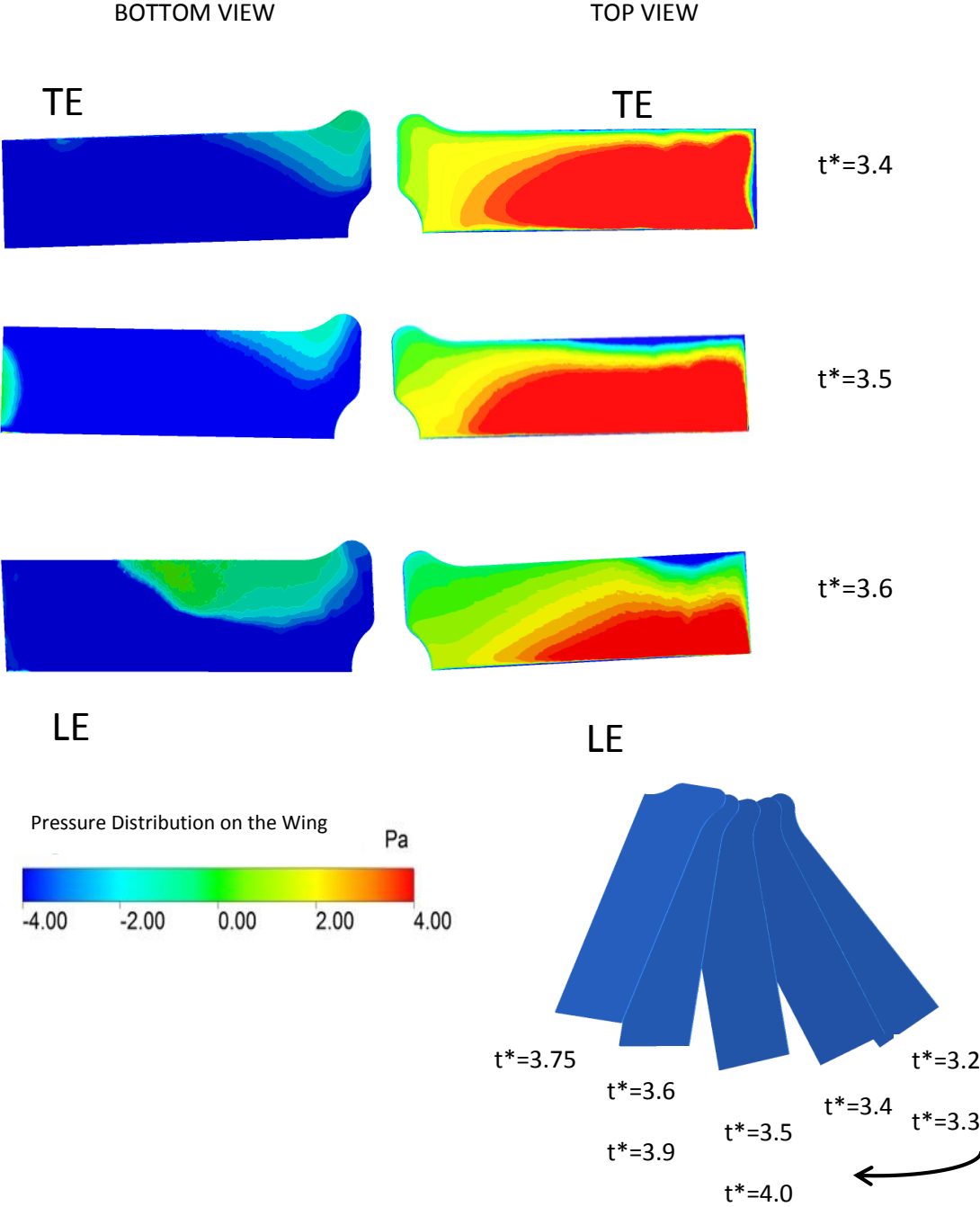$$d\theta/dt = 2\pi f*60.\pi/180*\cos(2\pi ft) \qquad\qquad [4.5]$$

Figure 4.26: Top and bottom views at downstroke of 4th period for Case 5

60

Figure 4.26 shows pressure distribution at the top and bottom surface of the wing at t*=3.4 , 3.5,3.6 at downstroke of the 4th period when sweeping amplitude is 120 ⁰. High pressure is maximum where C_L (Figure 4.28) is minimum and C_D (Figure 4.29) is maximum and it is observed that is started from the leading edge at t*=3.4 and grows to center of top surface in at t*=3.5. On the other hand , a suction region is visualized at the bottom surface at t*=3.4 and 3.5. At t*=3.6, pressure starts to decrease where C_D starts to decrease. In addition, Figures 4.30 and 4.31 show that the wing is in original starting point and sweeping velocity is minimum at t*=3.5.
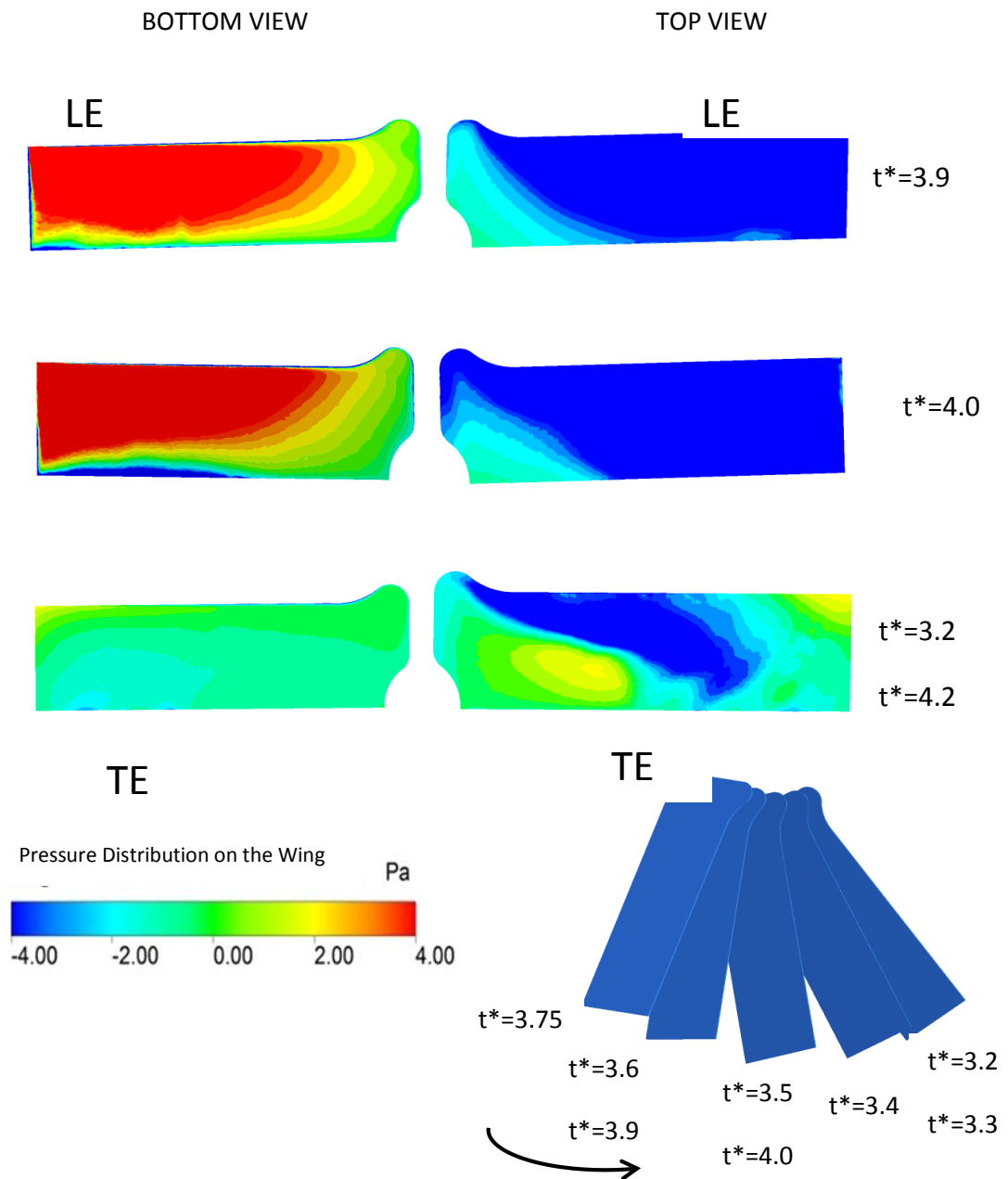

Figure 4.27: Top and bottom views at upstroke of 4th period for Case 5

Figure 4.27 shows pressure distribution at the top and bottom surface of the wing when t* is equal to 3.9 , 4.0 , 3.2=4.2 at upstroke of the 4th period. Suction pressure is visualized where C_L (Figure 4.28) is nearly maximum and C_D (Figure 4.29) is nearly minimum at a large area of the bottom surface at t*=3.9 and grows at t*= 4.0. On the other hand, a high pressure region is visualized and that is starts from leailing edge of the bottom surface at t*= 3.9 and grows to the center at t*=4.0. At t*=3.2, pressure distribution enters the transition region. In addition, from Figures 4.30 and 4.31 show that at t*=4.0 ,the wing is in the original point and sweeping velocity is maximum at that point.
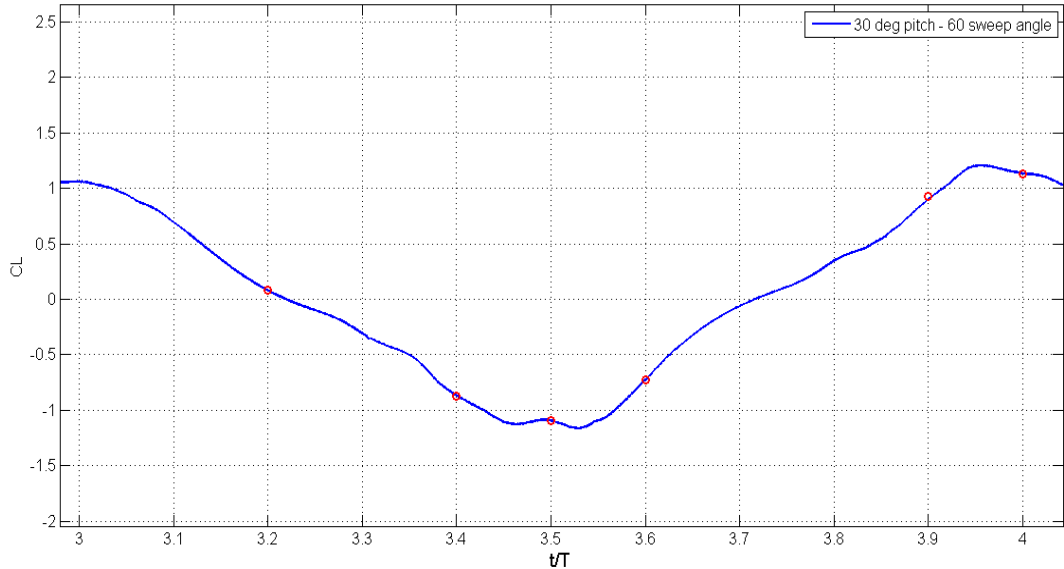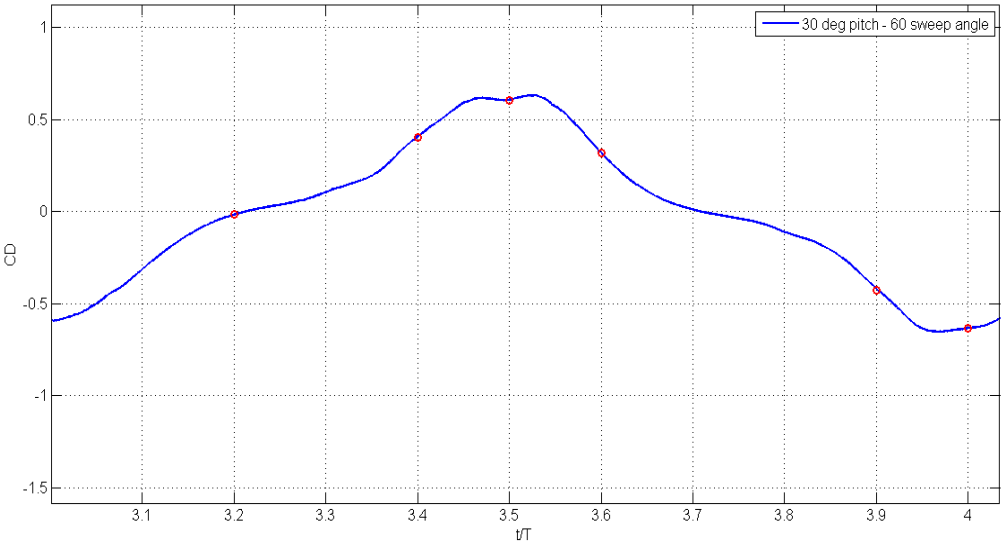

Figure 4.28: Lift coefficient for 4th Period at case 5

Figure 4.29: Drag coefficient for 4th Period at case 5

62

Drag coefficient and lift coefficients are plotted for 4th Period at case 5 . Figures 4.28 and 4.29 show lift and drag coefficient variations for 5^0 pitch angle and 60^0 sweep angle at 4th period during upstroke and downstroke. According to plots when C_D is increasing , C_L is decrasing from t*=3.2 to t*=3.5. On the other hand , when C_L is increasing, C_D is decreasing from t*=3.6th to t*=4.0.
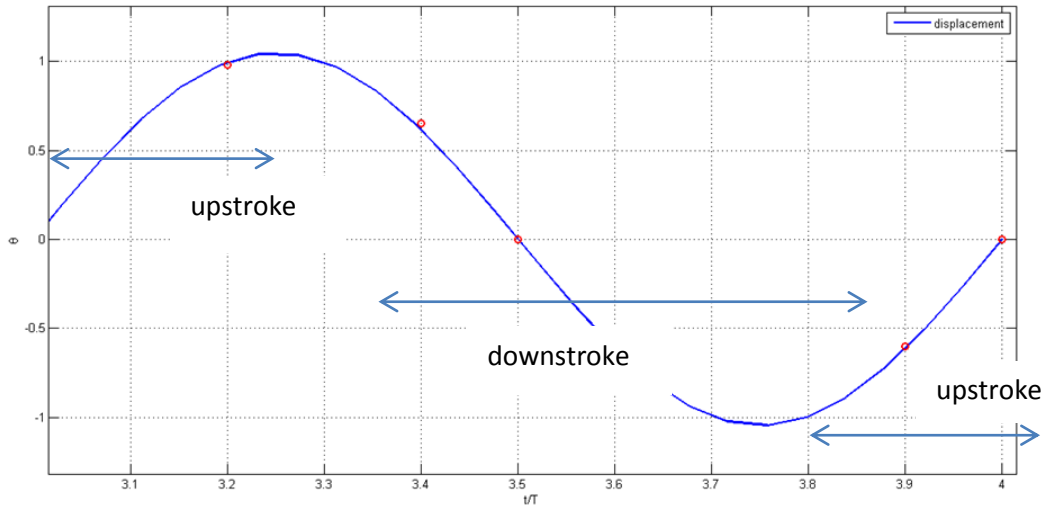

Figure 4.30: Sweeping position for 4th Period at case 5
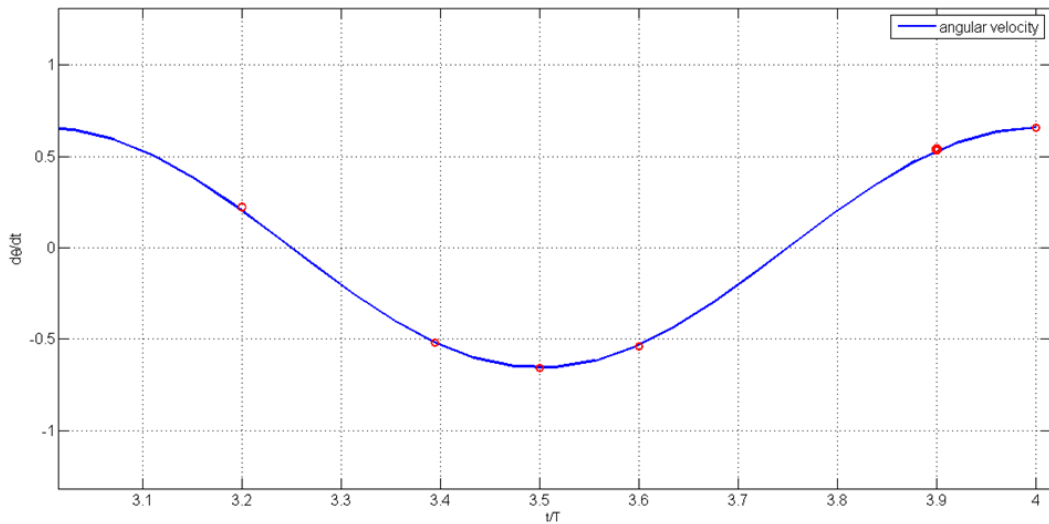

Figure 4.31: Sweeping veolcity for 4th Period at case 5

Figure 4.30 and 4.31 show sweeping displacement and velocity at 4th period for Case 5. Figure 4.30 is a sinusoidal function and Figure 4.31 is a cosine functio
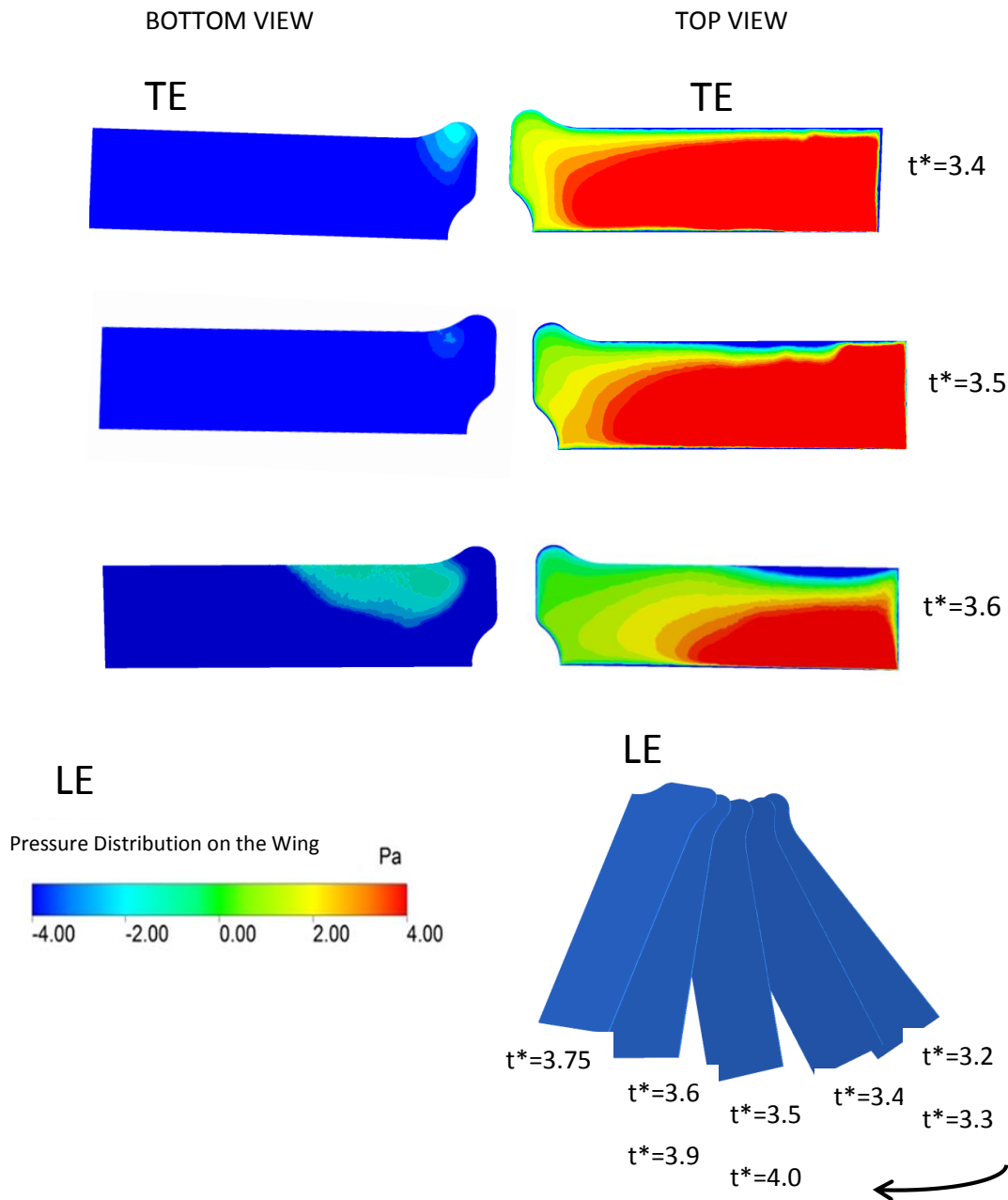
Figure 4.32: Top and bottom views at downstroke of 4th period for Case 6

Figure 4.32 shows pressure distribution at the top and bottom surface of the wing at t*=3.4, 3.5, 3.6 at downstroke of the 4th period when sweeping amplitude is 120^0. High pressure is maximum where C_L (Figure 4.34) is minimum and C_D (Figure 4.35) is maximum is observed that is started from the leading edge at t*= 3.4 and grows to center of top surface at t*=3.5. On the other hand, a suction region is visualized at the bottom surface at t*= 3.4 and 3.5. In addition, Figures 4.36 and 4.37 shows that the wing is in original starting point and sweeping velocity is minimum at t*=3.5.

BOTTOM VIEW

TOP VIEW

LE

LE

t*=3.9

t*=4.0

t*=3.2

t*=4.2

TE

TE

Pressure Distribution on the Wing

Pa

-4.00   -2.00   0.00   2.00   4.00

t*=3.75

t*=3.6

t*=3.2
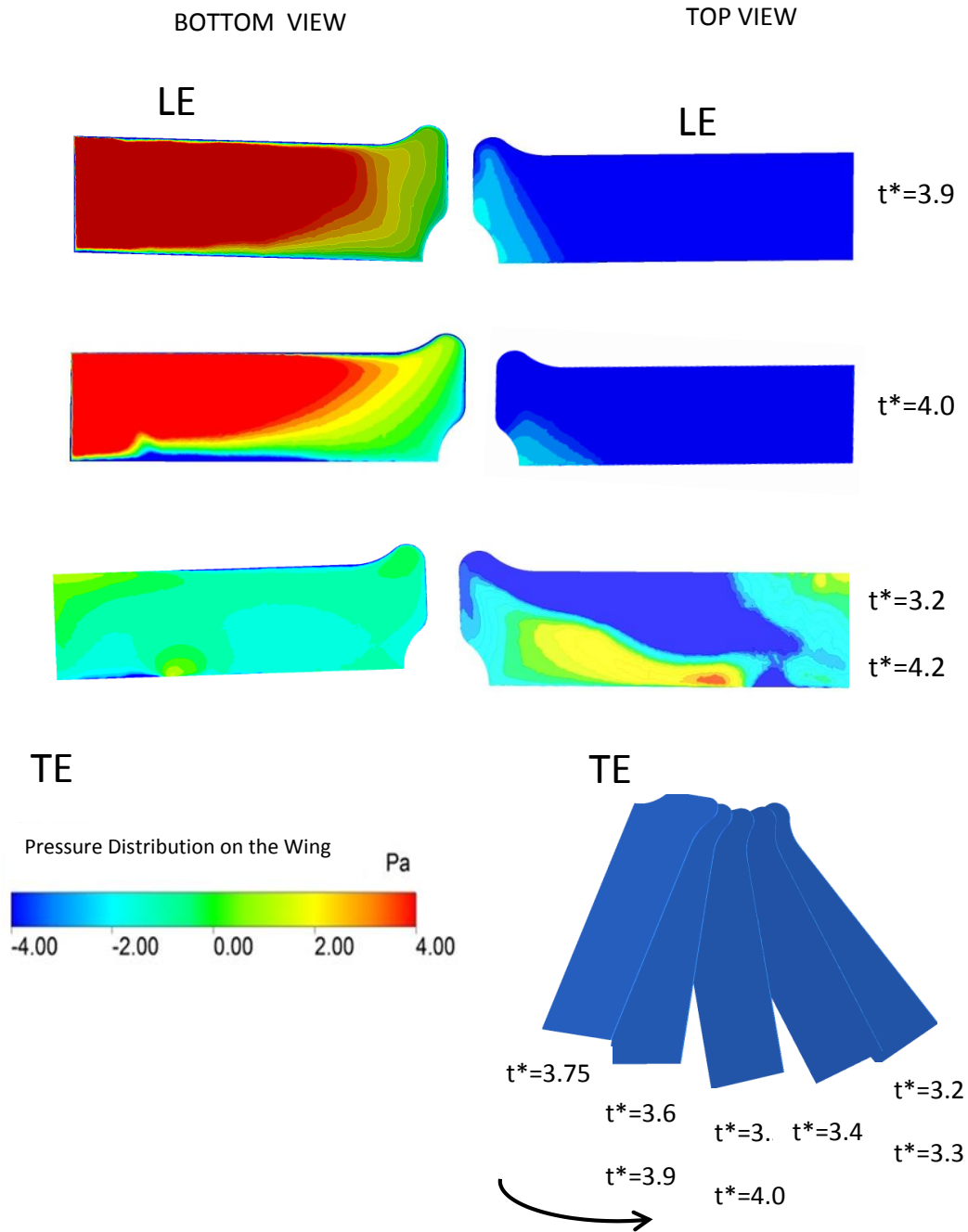
t*=3.   t*=3.4

t*=3.3

t*=3.9

t*=4.0

Figure 4.33: Top and bottom views at first second stroke of 4th period for Case 6

Figure 4.33 shows pressure distribution at the top and bottom surface of the wing at t=3.9 , 4.0 ,3.2=4.2 positions at upstroke of the 4th period. Suction pressure where C_L (Figure 4.34) is maximum and C_D (Figure 4.35) is minimum is observed at a large area which is close to the leading edge of the top surface at t*= 3.9 position and grows at t*=4.0. On the other hand, a high pressure region is visualized and that is also large area of the bottom surface at t*=3.9 and grows to the center at t*=4.0. At

t*=3.2=4.2 , the wing enters the transient region. The wing position changes from upstroke to downstroke position. So pressure distribution also enters a trainsient region. In addition, figures 4.36 and 4.37 shows that at t*=4.0 , the wing is in the original point and sweeping velocity is maximum at that point.
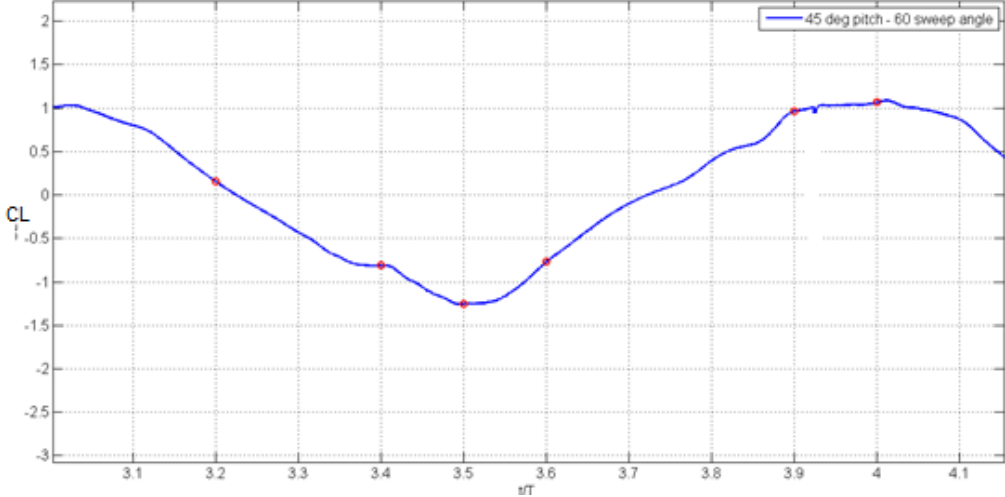

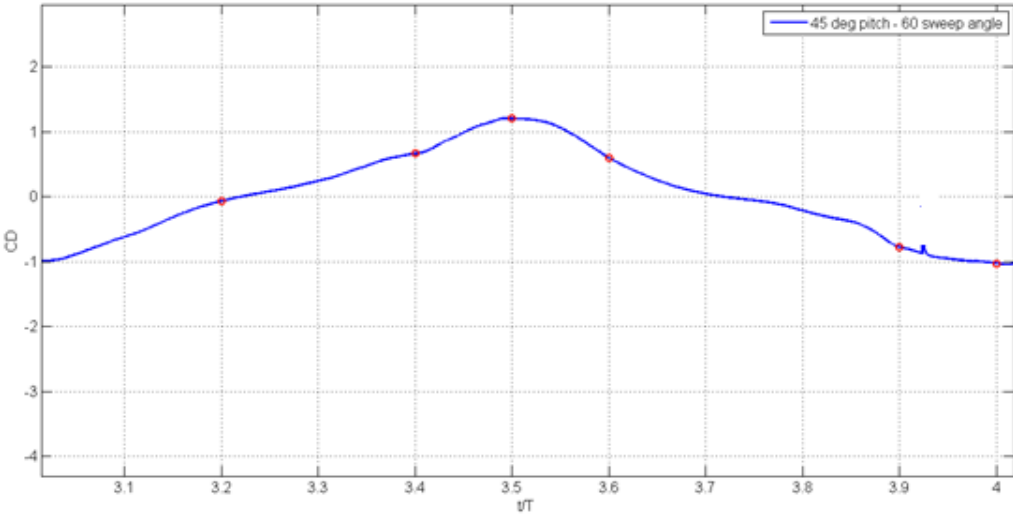Figure 4.34:Lift coefficient for 4th Period at case 6

Figure 4.35: Drag coefficient for 4th Period at case 6

 Drag coefficient and lift coefficients are plotted for 4th Period at case 6. Figures 4.34 and 4.35 show lift and drag coefficient variations for 5^0 pitch angle and 60^0 sweep angle at 4th period during uostroke and downstroke motion. According to plots when C_D is increasing , C_L is decreasing from t*=3.2 seconds to t*=3.5 position. On the other hand , when C_L is increasing, C_D is decreasing from t*=3.6 to 4.0.
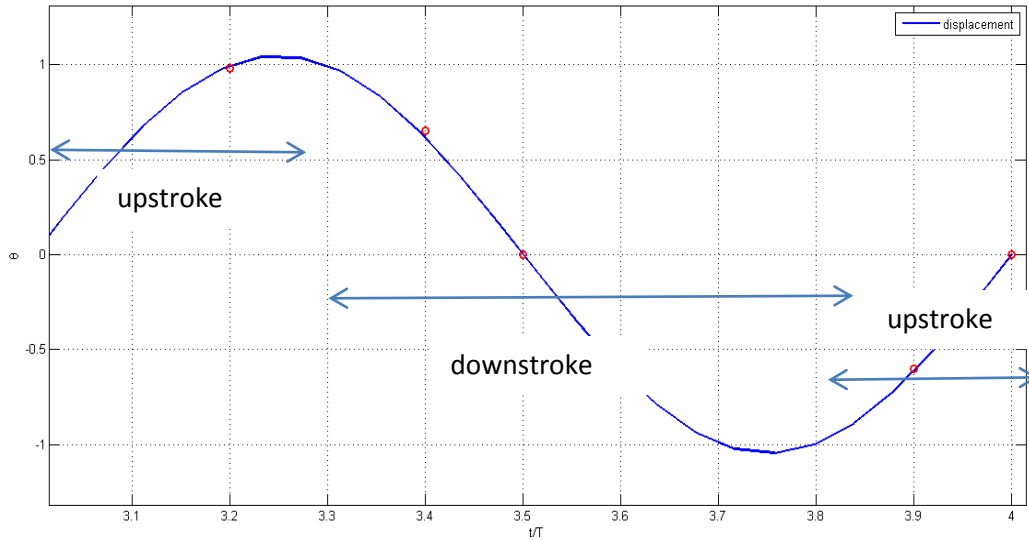
66

Figure 4.36: Sweeping position for 4th Period at case 6
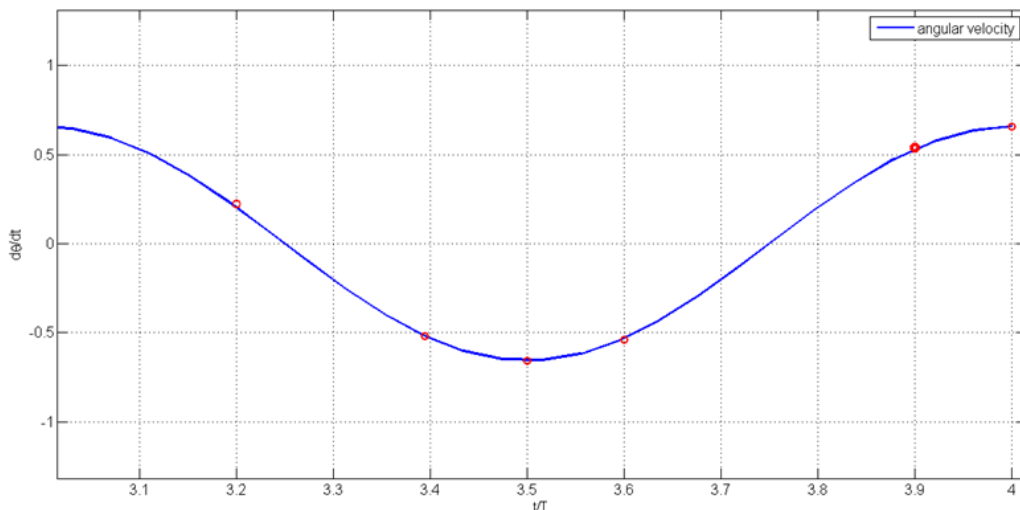
Figure 4.37: Sweeping velocity for 4th Period at case 6

Figure 4.36 and 4.37 shows sweeping displacement and velocity at 4th period for Case 6. Figure 4.36 is a sinusoidal function and figure 4.37 is a cosine function.

4.2 Comparison of Aerodynamic Force Coefficients:

The result are given during four periods in Figures 4.38 - 4.41 for three different pitch angle configurations (α=5º, 30º and 45º).

The results are analysed during the 4th of the period of the motion after the impusive effect is dissappeared. Figures 4.38 - 4.41 show the comparison of aerodynamic

forces for Case 1, Case 2, Case 3, Case 4, Case 5 and Case 6. The figures also show the time dependent sweeping angular displacement, θ and angular velocities, $\dot{\theta}$.

Pressure distribution is examined by using ANSYS CFD Post package program at three different constant pitch angles (5º,30 º,45º) for two sweep angles (60 º and 120^0 º). According to the results, pressure change is low at 5º constant pitch angle for two sweep angles. However, for 30º and 45º constant pitch angles, pressure distribution on flat plate is highy remarkable especially at 120º sweep angle. Pressure distribution is observed that it is much higher where C_L is minimum and C_D is maximum. Pressure distribution is highest at 45^0 constant pitch angle with a 120^0 sweep angle.

Lift and drag force coefficients are plotted for two different sweep angles (60º and 120º) at three different constant pitch angles (5 º, 30º and 45º).for four periods. From the plots, it is seen that at 45º pitch angle produces more lift and drag coefficient. In order to fly efficiently lift coefficient must be sufficiently high to design better MAV's. So 45º is efficient for both cases to produce better aerodynamic outputs.
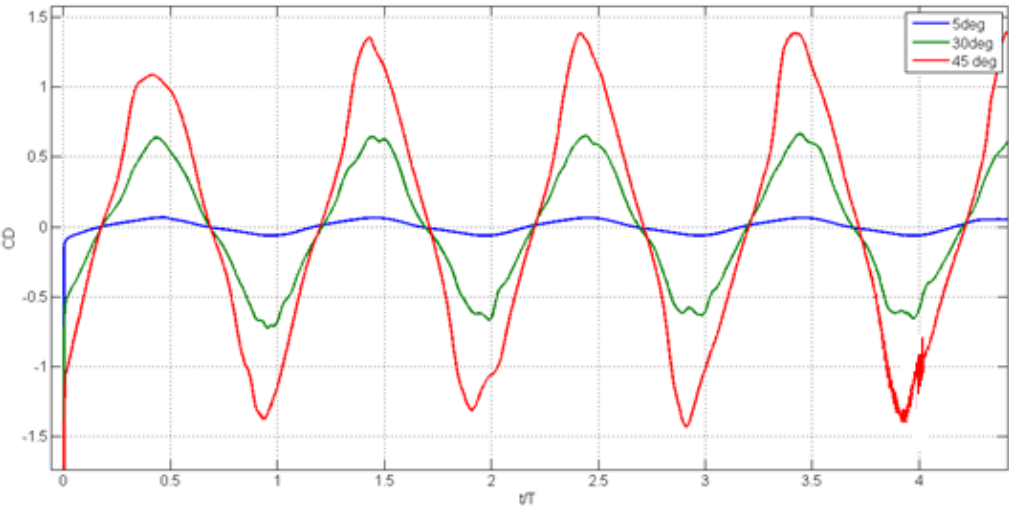

Figure 4.38: Drag coefficients at 30 deg sweep angle
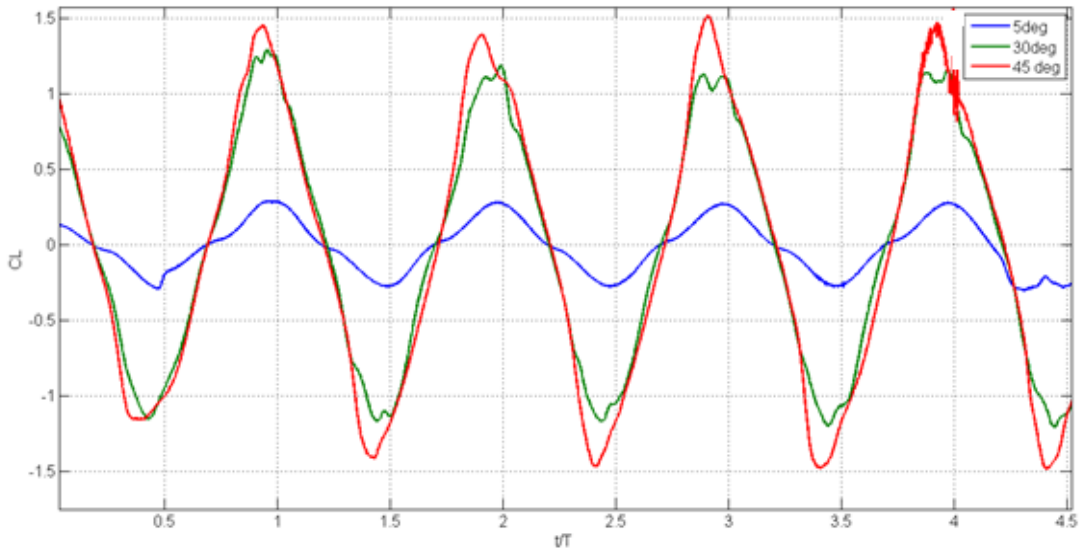(blue:5deg,green:30deg,red:45deg)

Figure 4.39: Lift coefficients at 30 deg sweep angle
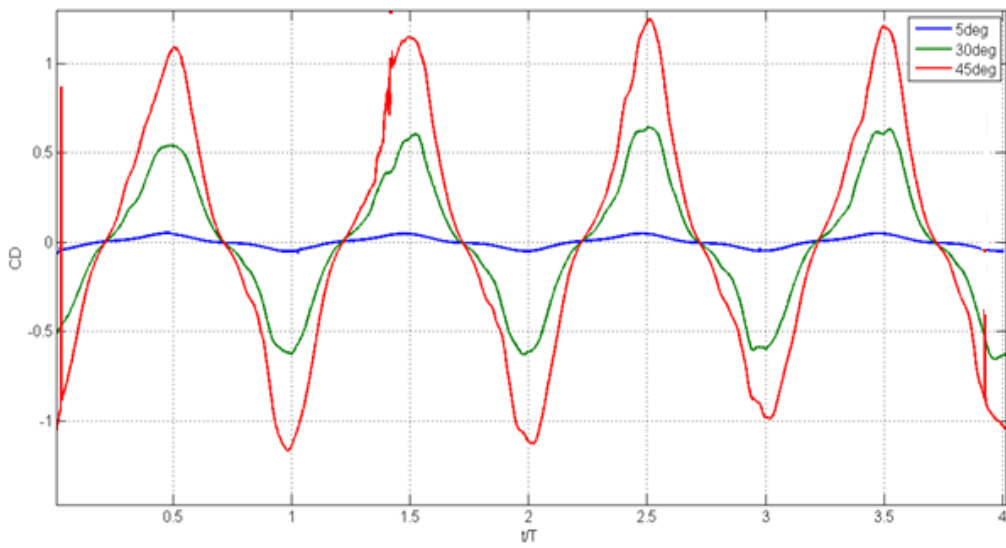
(blue:5deg,green:30deg,red:45deg)

Figure 4.40: Drag coefficients at 60 deg sweep angle

(blue:5deg green:30deg, red:45deg)
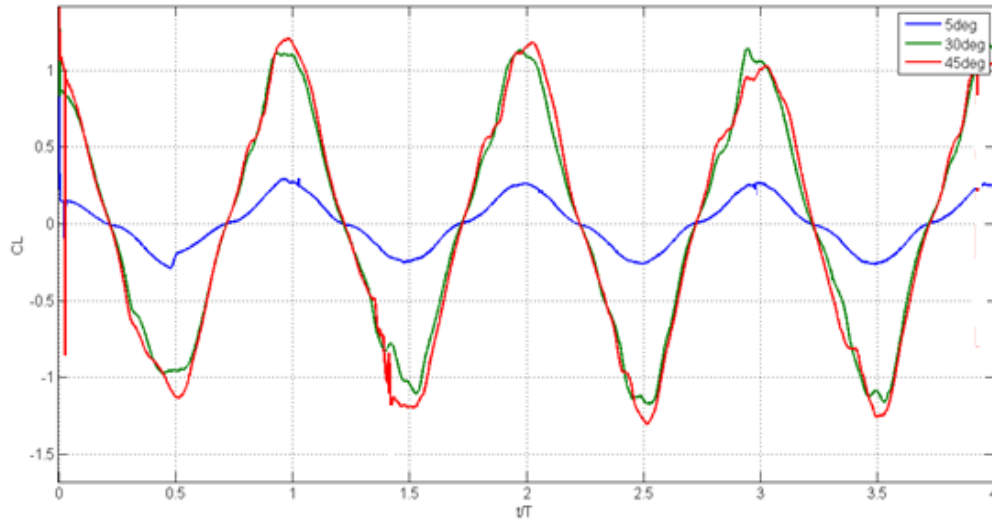
Figure 4.41: Lift coefficients at 30 deg sweep angle

(blue:5deg, green:30deg, red:45deg)

The aim in this investigation is to see the effect of different pitch angles on lift and drag generated during 3D flapping motion. From the results, it is observed that lift coefficient (z force) is highest value at 45° pitch angle. Also at this pitch angle, X force (drag coefficient) curves have higher peak values than at 5^0 and 30^0 angles. On the other hand, at 5° pitch angle lift force coefficient (Z force) is nearly zero. In addition, lift and drag coefficients attain a periodic behaviour with respect to flapping motion and their cycles are similar, regardless of the motion type.

Figure 4.42 Pressure contours at t*=3 (top surface)

Figure 4.43 Pressure contours at t*=3 (bottom surface)

Top surface t*=3.5
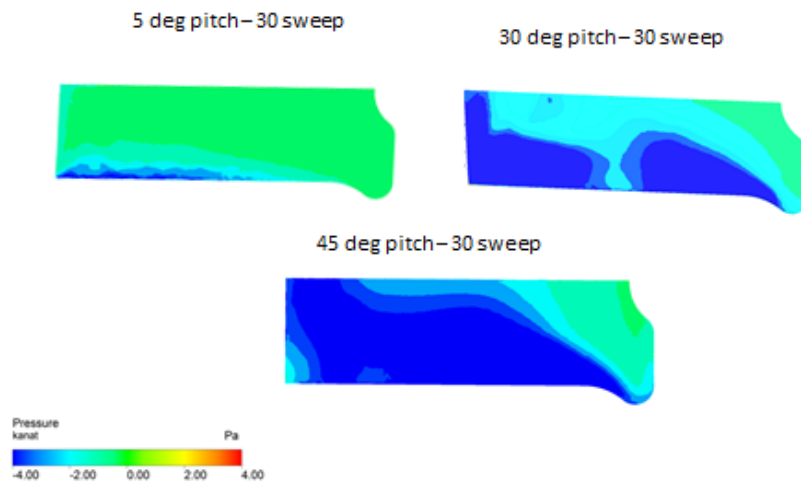
5 deg pitch–30 sweep

30 deg pitch–30 sweep

45 deg pitch–30 sweep

Pressure
kanat   Pa

-4.00   -2.00   0.00   2.00   4.00
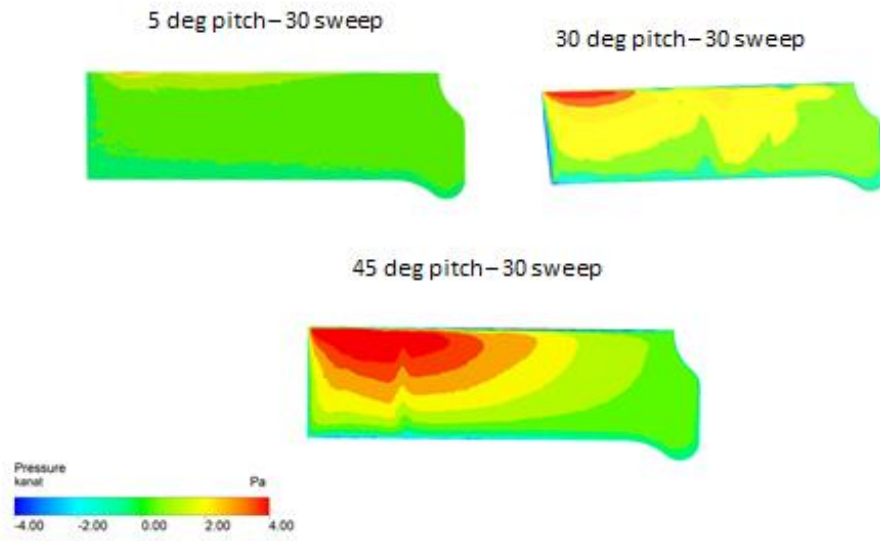
Figure 4.44 Pressure contours at t*=3.5   (top surface)

Bottom surface t*=3.5

5 deg pitch–30 sweep

30 deg pitch–30 sweep

45 deg pitch–30 sweep

Pressure
kanat   Pa

-4.00   -2.00   0.00   2.00   4.00

Figure 4.45 Pressure contours at t*=3.5   (bottom surface)

Figures 4.42-4.45 show pressure contours at the same time (t*=3 -3.5) for three different pitch angles (5^0, 30^0, 45^0) and for bottom and top surfaces. As it can be seen from the figures, when pitch angle increases , pressure becomes much higher on the top surface whereas it becomes much lower on the bottom surface. In addition,

72

Figure 4.42 and 4.43 show maximum negative C_D and maximum C_L location and Figure 4.44 and 4.45 show minimum C_L and maximum C_D location.

4.3 Velocity vectors and Streamlines on three different planes :

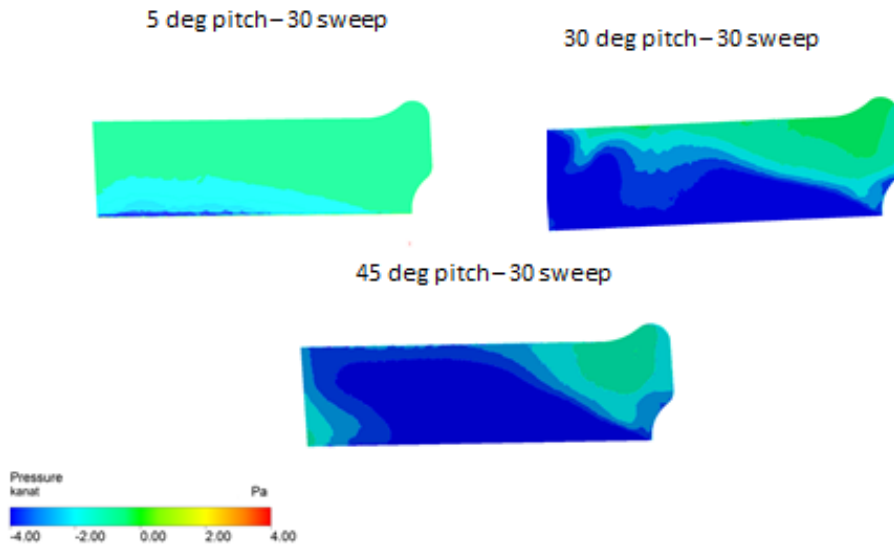Three planes (plane1,plane2, plane3) are located at x= - 0.1m, x=0.0m and x= 0.1 m. The velocity vectors and streamlines are plotted on these planes and then investigation are performed at different instantenous time points.
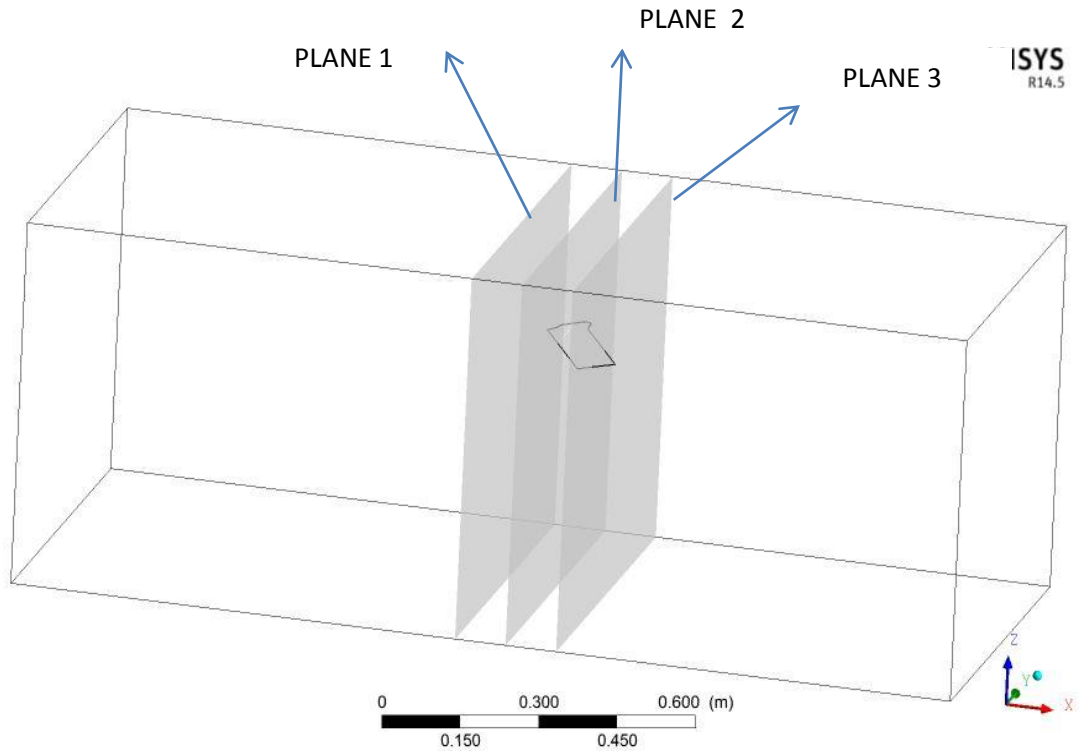
Figure 4.46: Three planes at different locations (x=-0.1 m,0 m,0.1 m)

Plane 1: -0.1 m

Plane 2: 0.0 m

Plane 3: 0.1 m

Case 1:

At t*=3.2 :

<div align="center">a)x=-0.1 m   b)x=0.0 m   c)x=0.1 m</div>
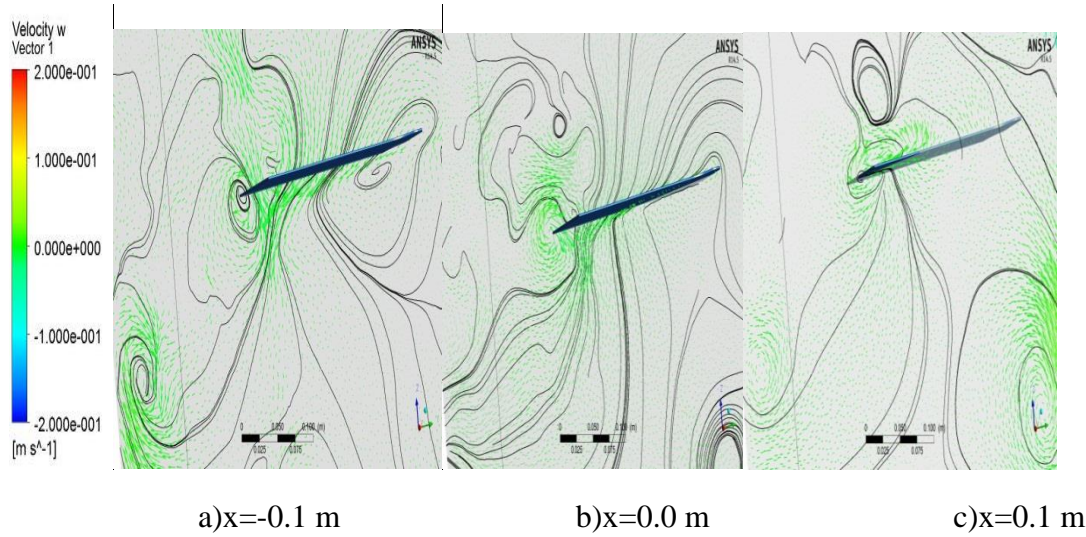
Figure 4.47 :Streamlines and velocity vectors at 5^0 pitch angle and 30^0 sweep angle (t*=3.2)

At t*=3.3 :

<div align="center">a)x=-0.1 m   b)x=0.0 m   c)x=0.1 m</div>
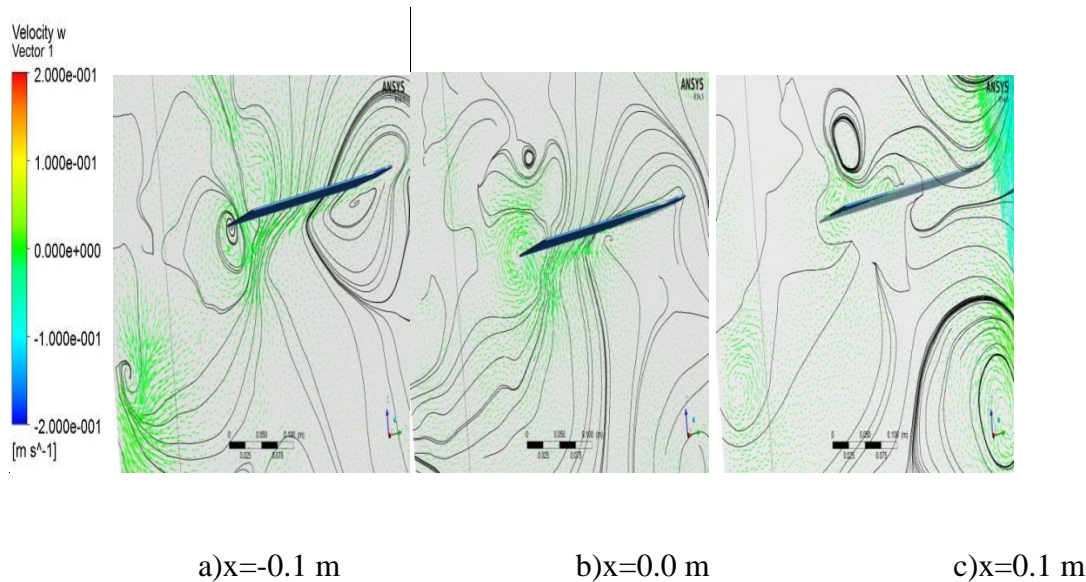
Figure 4.48 :Streamlines and velocity vectors at 5^0 pitch angle and 30^0 sweep angle (t*=3.3)

At t*= 3.4

<div align="center">a)x=-0.1 m   b)x=0.0 m   c)x=0.1 m</div>
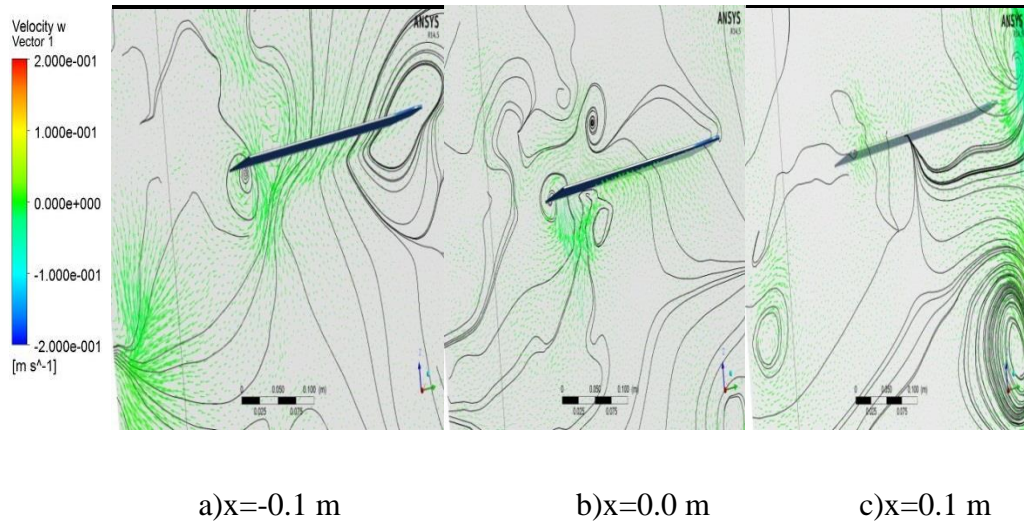
Figure 4.49 :Streamlines and velocity vectors at 5^0 pitch angle and 30^0 sweep angle (t*=3.4)

At t*=3.6

<div align="center">a)x=-0.1 m   b)x=0.0 m   c)x=0.1 m</div>
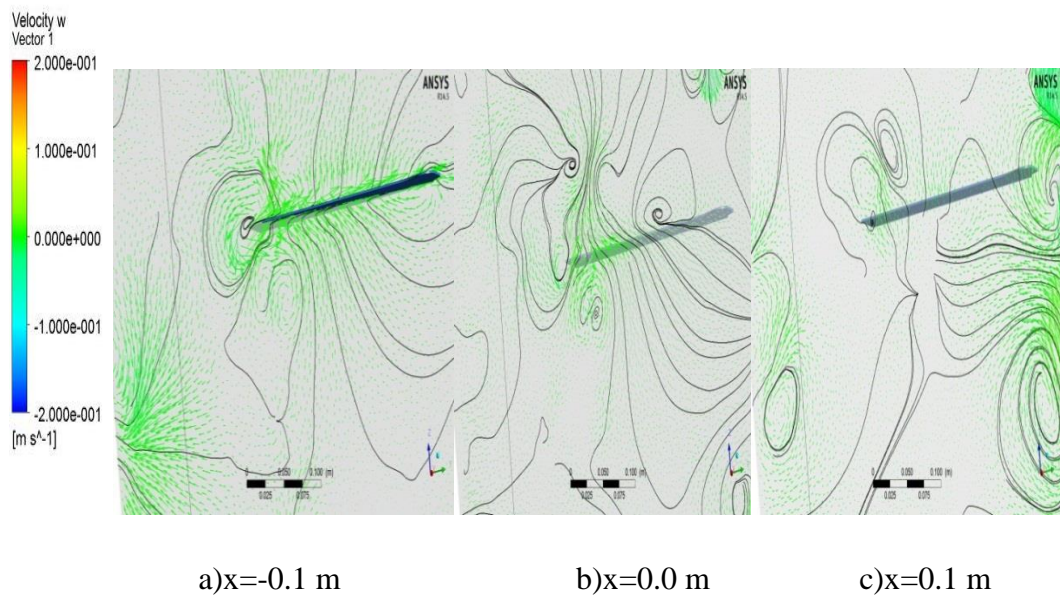
Figure 4.50 :Streamlines and velocity vectors at 5^0 pitch angle and 30^0 sweep angle (t*=3.6)

At t*=3.9

<div align="center">a)x=-0.1 m   b)x=0.0 m   c)x=0.1 m</div>
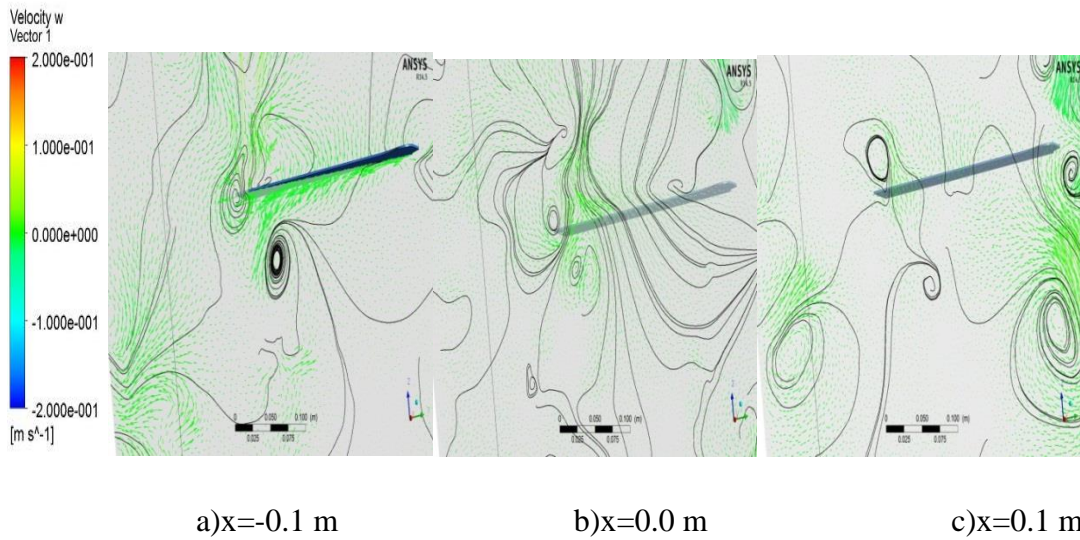
Figure 4.51 :Streamlines and velocity vectors at 5^0 pitch angle and 30^0 sweep angle (t*=3.9)

At t*=4.0

<div align="center">a)x=-0.1 m   b)x=0.0 m   c)x=0.1 m</div>
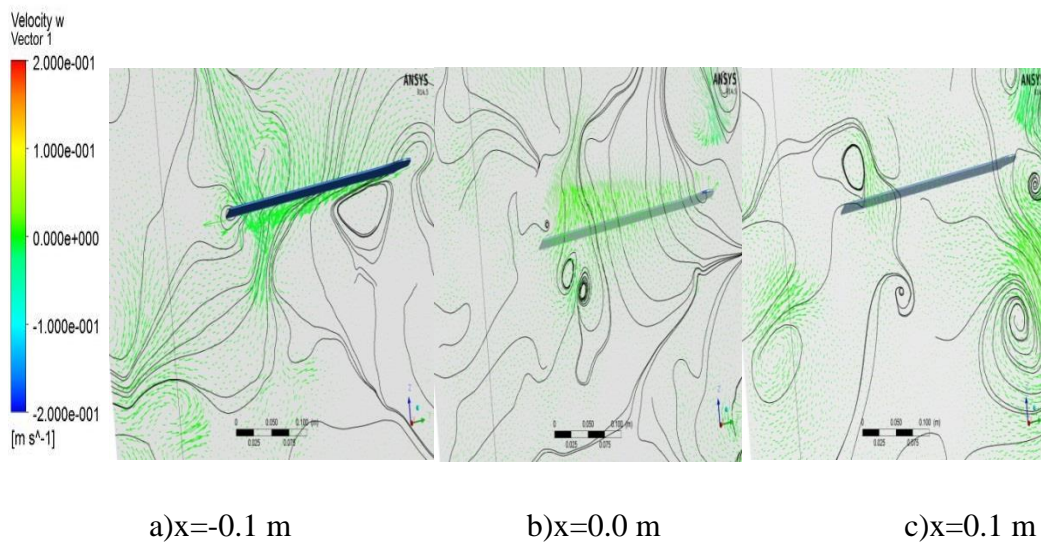
Figure 4.52:Streamlines and velocity vectors at 5^0 pitch angle and 30^0 sweep angle (t*=4.0)

Instantaneous velocity vectors and surface steramlines are plotted for three different planes at t*=3.2,3.3,3.4,3.6 ,3.9 and 4.0. Center plane (Plane 2) is located at the center of the tank (x=0.0m) and the other planes (Plane 1 and Plane 3) are located at x=- 0.1m and x=+0.1m respectively. Plane 1, Plane 2 and Plane 3 intersects with

wing at some t* points. At t*=3.2 , Plane 1 shows clockwise and counterclockwise vortex at the center and left hand side of the plane and where numbers of the streamlines are much more , numbers of velocity vectors are also much more there. The fluid structure is complex at the intersection region. Also, the number of velocity vectors are considerable at the intersection region because of the wing and fluid interaction. In addition, speed of the wing moves the fluid at that region. Also laminar flow exists left hand side of the plane 2 at t*=3.2 But from t*=3.2 to t*=4.0 flow separation occurs since wing intersects with plane 2 at t*=3.4 . When t* goes from 3.2 to 4.0 numbers of vortex increases and also fluid gets more complex because wing makes sweeping motion.

Case 2:

At t*:3.2
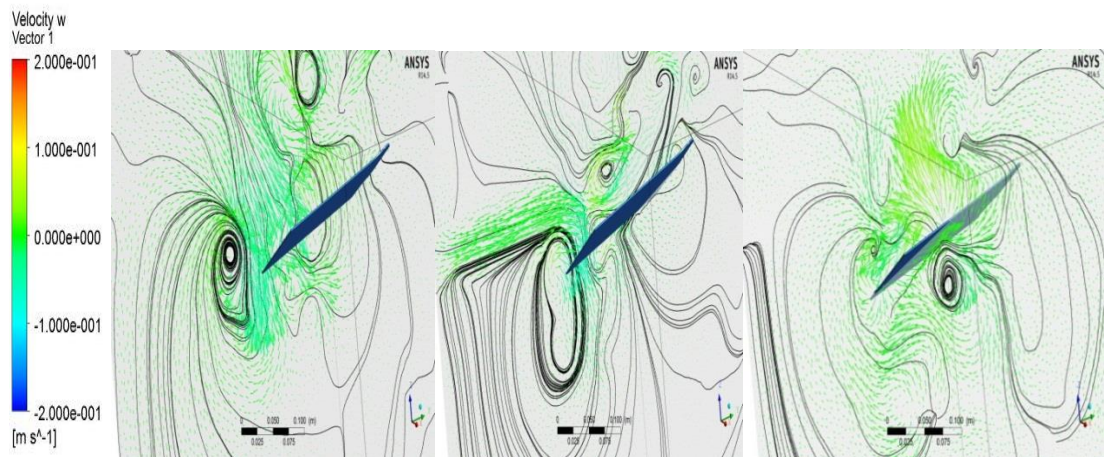
a)x=-0.1 m   b)x=0.0 m   c)x=0.1 m

Figure 4.53 :Streamlines and velocity vectors at 30^0 pitch angle and 30^0 sweep angle (t*=3.2)

At t*:3.3

<div align="center">a)x=-0.1 m   b)x=0.0 m   c)x=0.1 m</div>
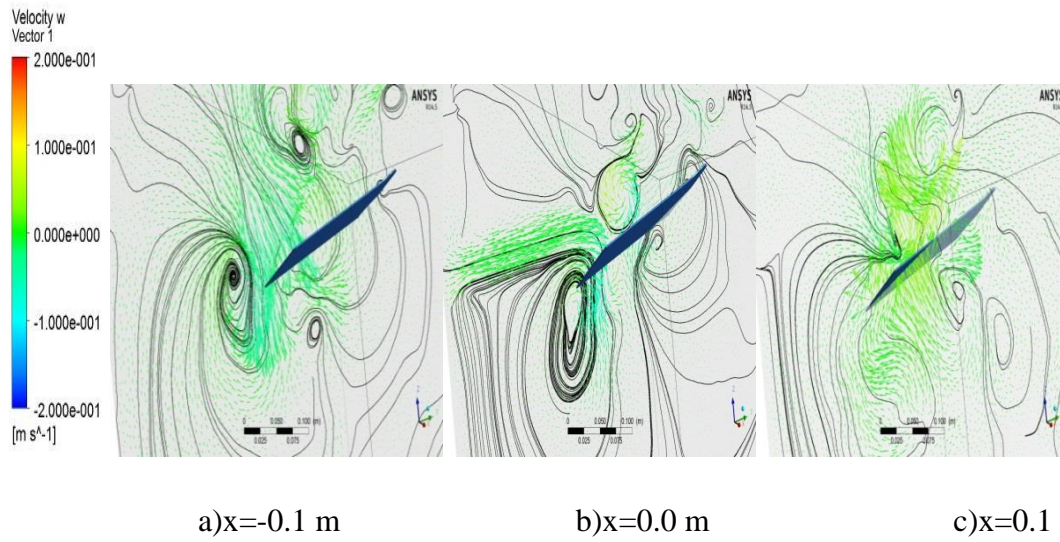
Figure 4.54 :Streamlines and velocity vectors at 30^0 pitch angle and 30^0 sweep angle (t*=3.3)

At t*:3.4

<div align="center">a)x=-0.1 m   b)x=0.0 m   c)x=0.1 m</div>
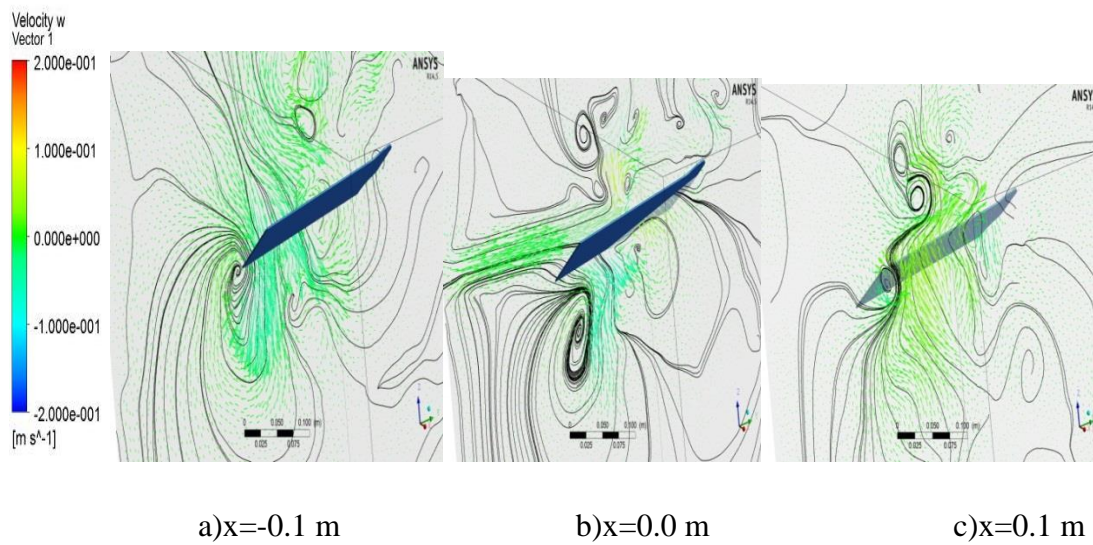
Figure 4.55:Streamlines and velocity vectors at 30^0 pitch angle and 30^0 sweep angle (t*=3.4)

At t*:3.6

<div align="center">a)x=-0.1 m   b)x=0.0 m   c)x=0.1 m</div>
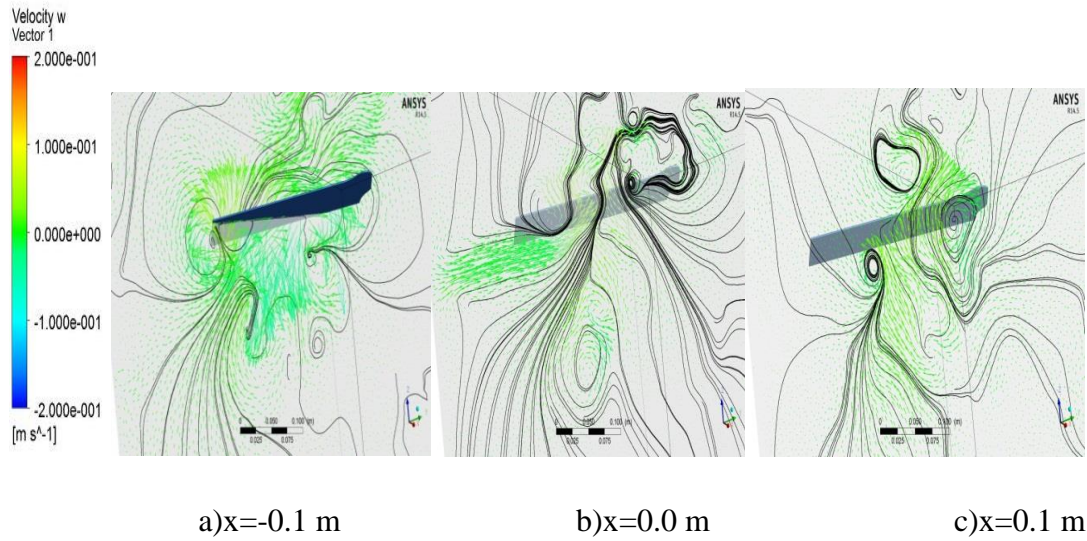
Figure 4.56 :Streamlines and velocity vectors at 30^0 pitch angle and 30^0 sweep angle (t*=3.6)

At t*:3.9

<div align="center">a)x=-0.1 m   b)x=0.0 m   c)x=0.1 m</div>
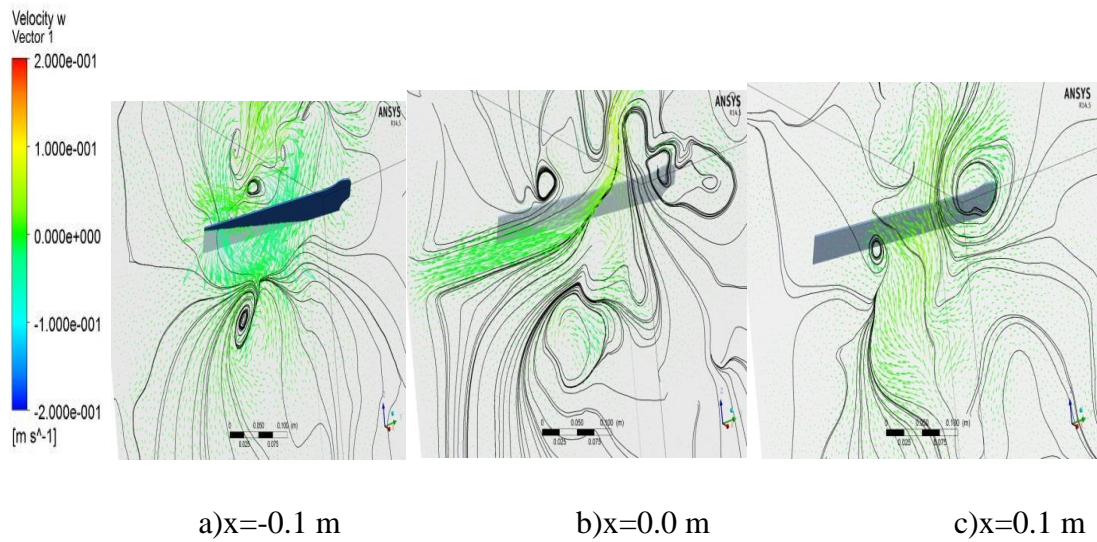
Figure 4.57 :Streamlines and velocity vectors at 30^0 pitch angle and 30^0 sweep angle (t*=3.9)

At t*=4.0

a)x=-0.1 m   b)x=0.0 m   c)x=0.1 m
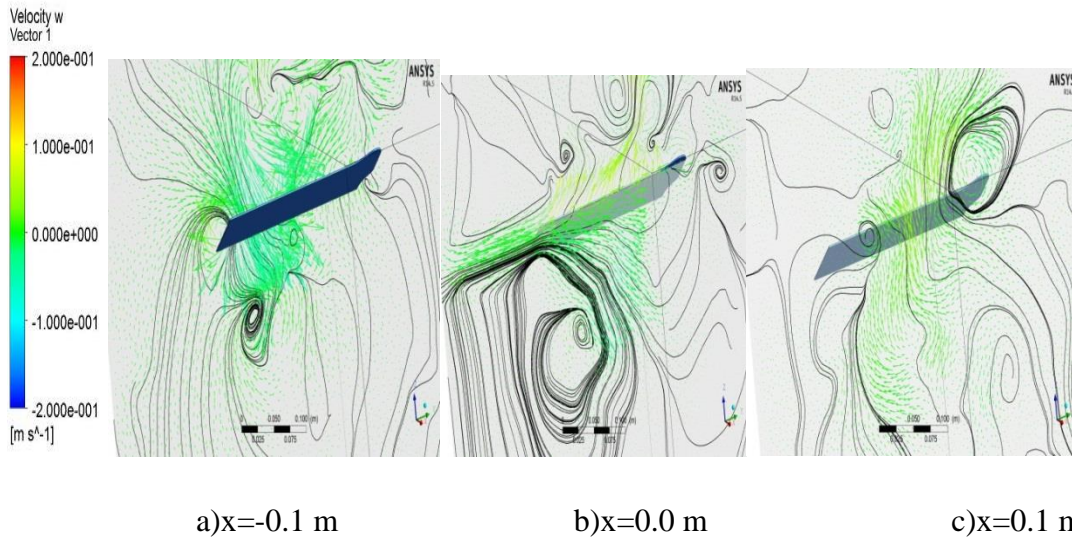
Figure 4.58 :Streamlines and velocity vectors at 30^0 pitch angle and 30^0 sweep angle (t*=4.0)

At t*=3.2 and 3.3, plane 3; at t*=3.4 and t*=4.0 , Plane 2; at t*=3.6 and 3.9, Plane 1 intersects with wing. At the interaction region, fluid direction is outward and also complex. Plane 2 shows clockwise vortex near the wing . At t*=3.4 wing intersects with plane at vortex region and decomposition occurs at vortex region at t*=3.6 Clockwise and counterclockwise vortices are more dominant on Plane 2 and Plane 3 at t*=3.6, 3.9 and 4.0.

Case 3:

At t*=3.2
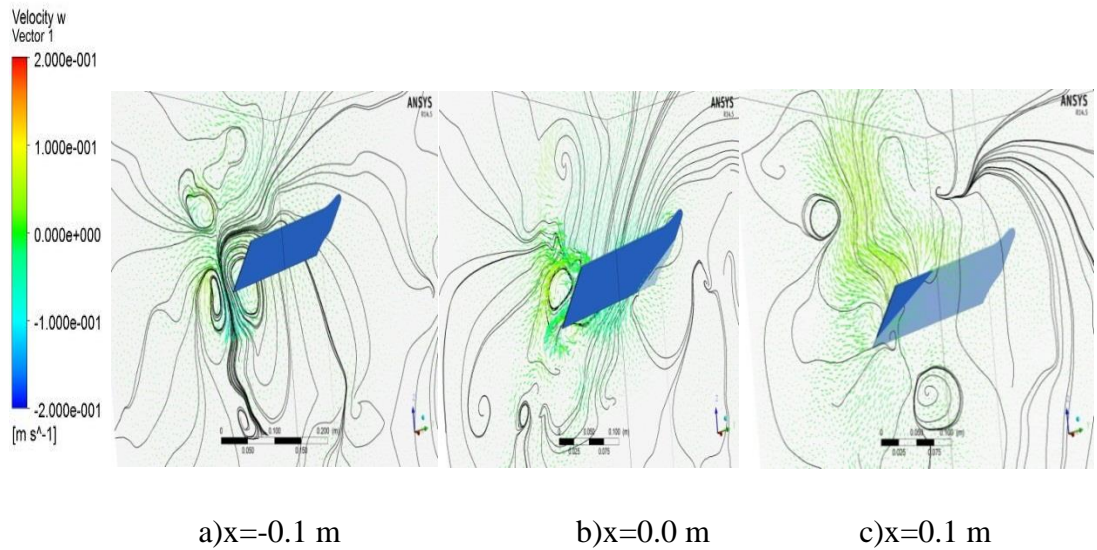
a)x=-0.1 m   b)x=0.0 m   c)x=0.1 m

Figure 4.59 :Streamlines and velocity vectors at 45^0 pitch angle and 30^0 sweep angle (t*=3.2)

At t*=3.3

a)x=-0.1 m   b)x=0.0 m   c)x=0.1 m

Figure 4.60 :Streamlines and velocity vectors at 45^0 pitch angle and 30^0 sweep angle (t*=3.3)

At t*=3.4

<div align="center">

a)x=-0.1 m   b)x=0.0 m   c)x=0.1 m

</div>

Figure 4.61:Streamlines and velocity vectors at 45^0 pitch angle and 30^0 sweep angle (t*=3.4)

At t*=3.6

<div align="center">

a)x=-0.1 m   b)x=0.0 m   c)x=0.1 m

</div>

Figure 4.62 :Streamlines and velocity vectors at 45^0 pitch angle and 30^0 sweep angle (t*=3.6)

At t*=3.9

a)x=-0.1 m   b)x=0.0 m   c)x=0.1 m
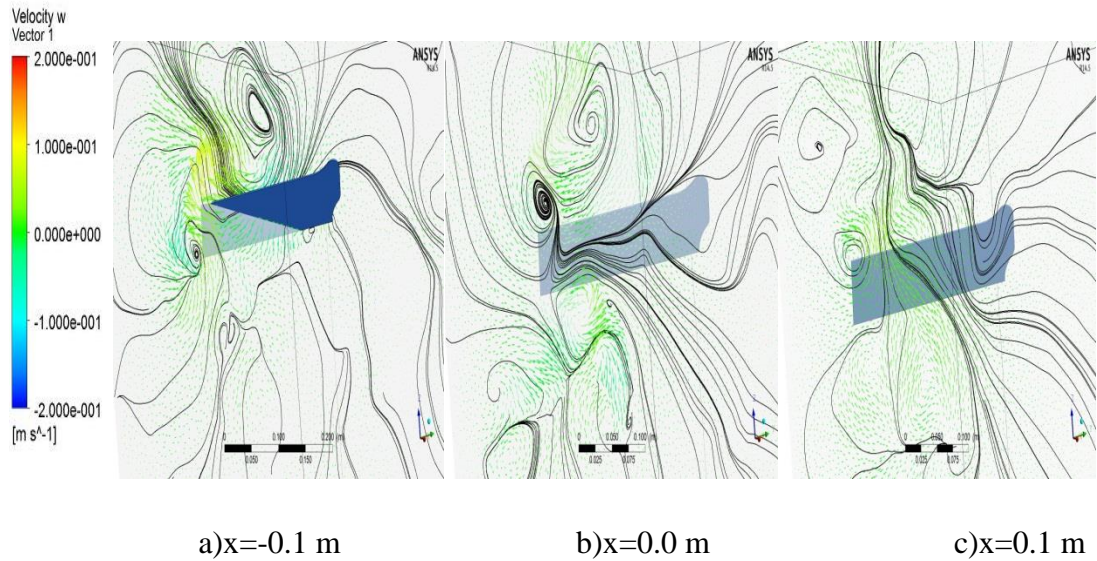
Figure 4.63 :Streamlines and velocity vectors at 45^0 pitch angle and 30^0 sweep angle (t*=3.9)

At t*=4.0

a)x=-0.1 m   b)x=0.0 m   c)x=0.1 m
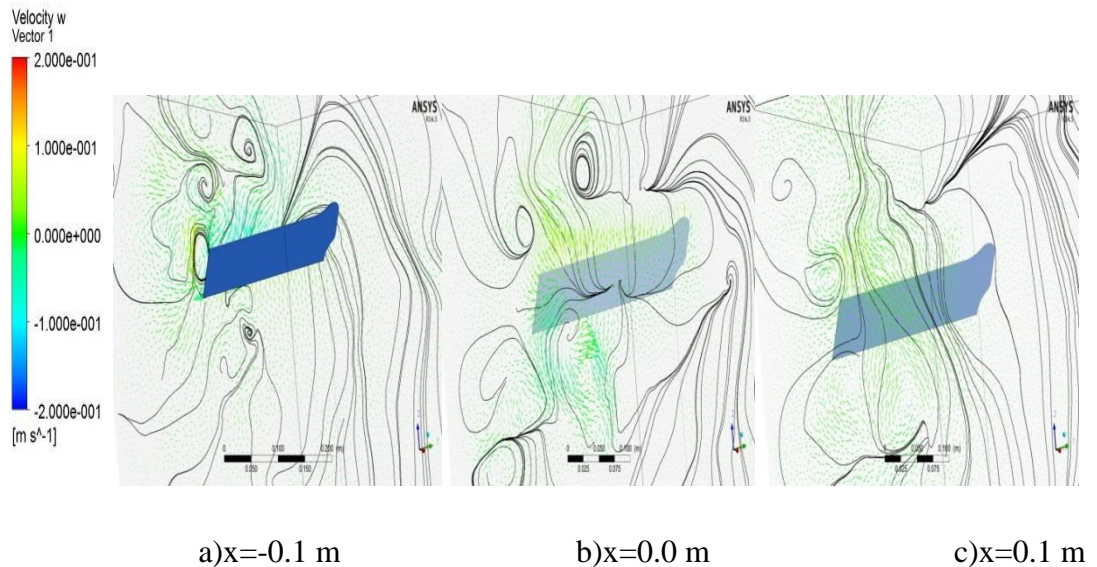
Figure 4.64 :Streamlines and velocity vectors at 45^0 pitch angle and 30^0 sweep angle (t*=4.0)

At the intersection region, numbers of velocity vectors are much more and direction of velocity vectors are also outward. Some clockwise and counterclockwise vortices

are exist on planes. In addition on some planes flow is uniform. At t*=3.2 Plane 1 and at t*=3.6 plane 2 show similar to doublet configuration. Some vortices exist at other planes and when pitch angle increases, fluid flow gets more complex and vortices gets bigger .

Case 4:

At t*=3.2
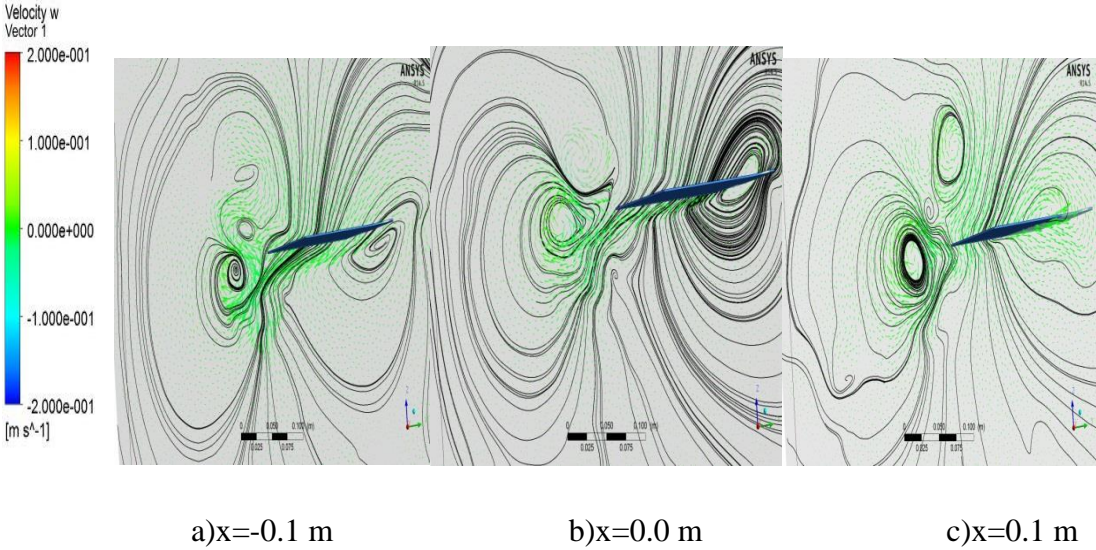
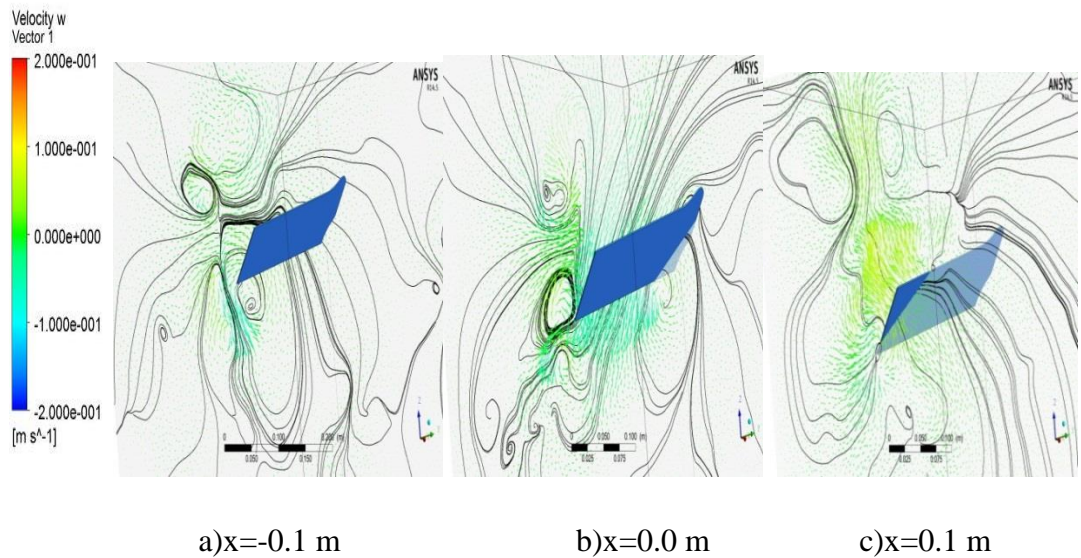<div align="center">a)x=-0.1 m   b)x=0.0 m   c)x=0.1 m</div>

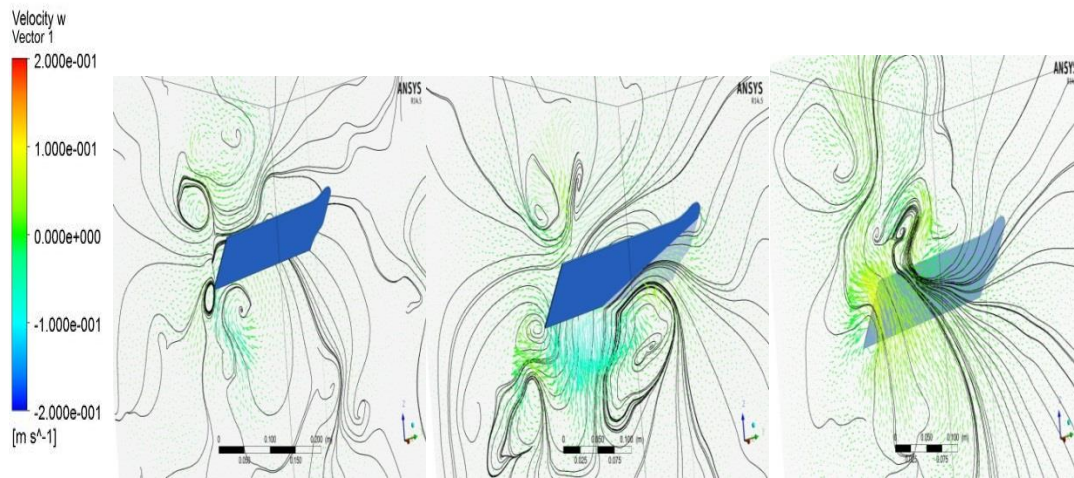Figure 4.65 :Streamlines and velocity vectors at 5^0 pitch angle and 60^0 sweep angle (t*=3.2)

At t*=3.4
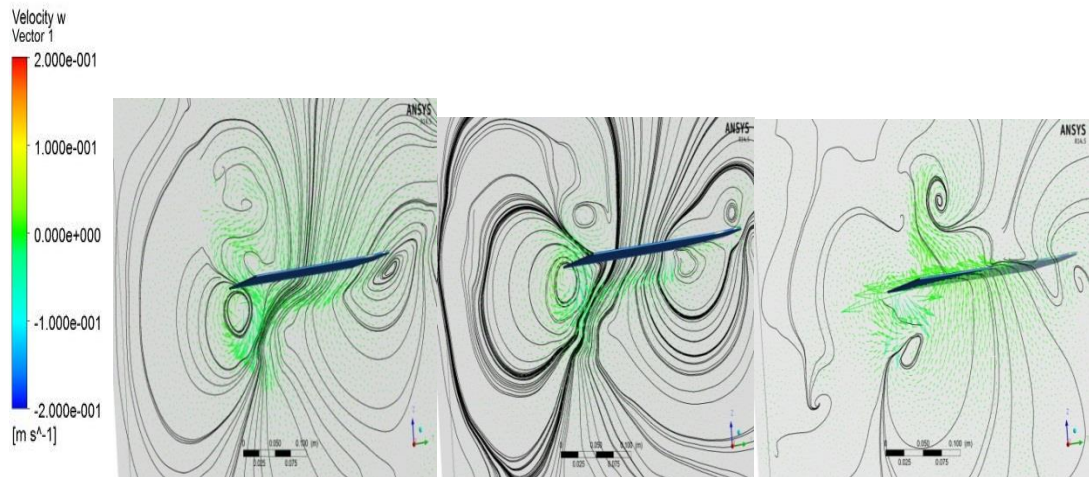
<center>a)x=-0.1 m   b)x=0.0 m   c)x=0.1</center>

Figure 4.66 :Streamlines and velocity vectors at 5^0 pitch angle and 60^0 sweep angle (t*=3.4)

At t*=3.5

<center>a)x=-0.1 m   b)x=0.0 m   c)x=0.1 m</center>

Figure 4.67 :Streamlines and velocity vectors at 5^0 pitch angle and 60^0 sweep angle (t*=3.5)

At t*=3.6

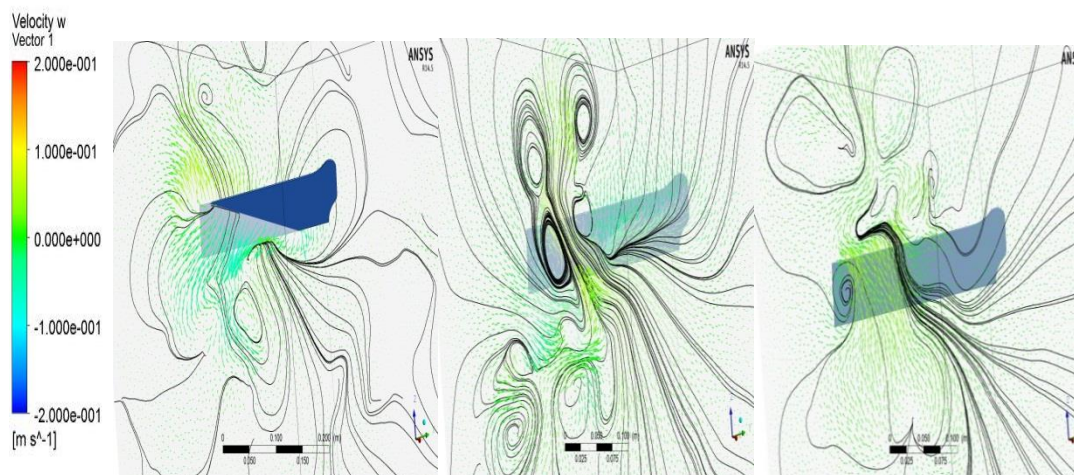a)x=-0.1 m   b)x=0.0 m   c)x=0.1 m
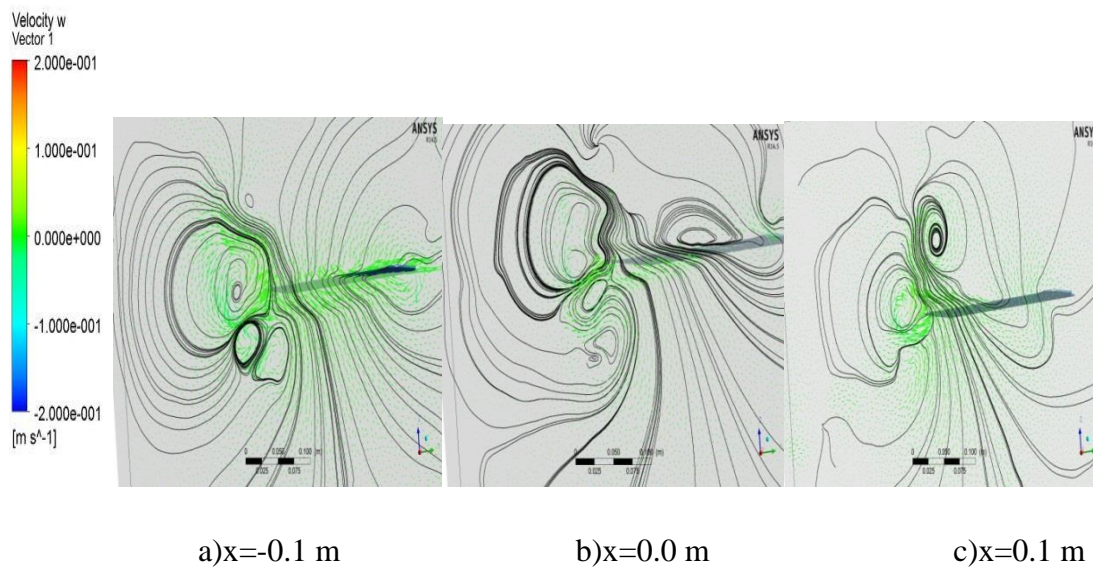
Figure 4.68 :Streamlines and velocity vectors at 5^0 pitch angle and 60^0 sweep angle (t*=3.6)

At t*=3.9

a)x=-0.1 m   b)x=0.0 m   c)x=0.1 m
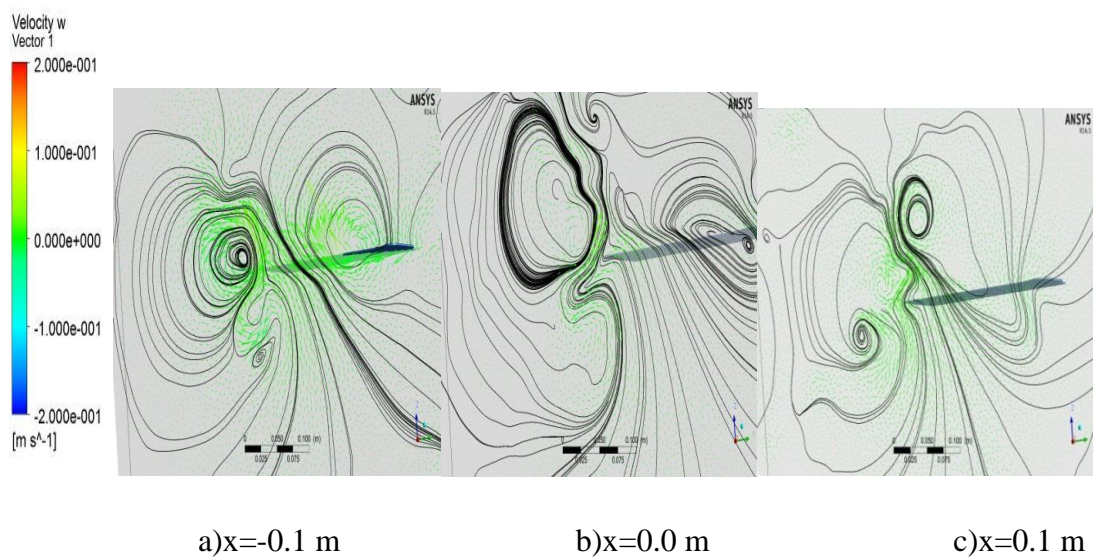
Figure 4.69 :Streamlines and velocity vectors at 5^0 pitch angle and 60^0 sweep angle (t*=3.9)

At t*=4.0

$\quad$ a)x=-0.1 m $\qquad\qquad$ b)x=0.0 m $\qquad\qquad$ c)x=0.1 m
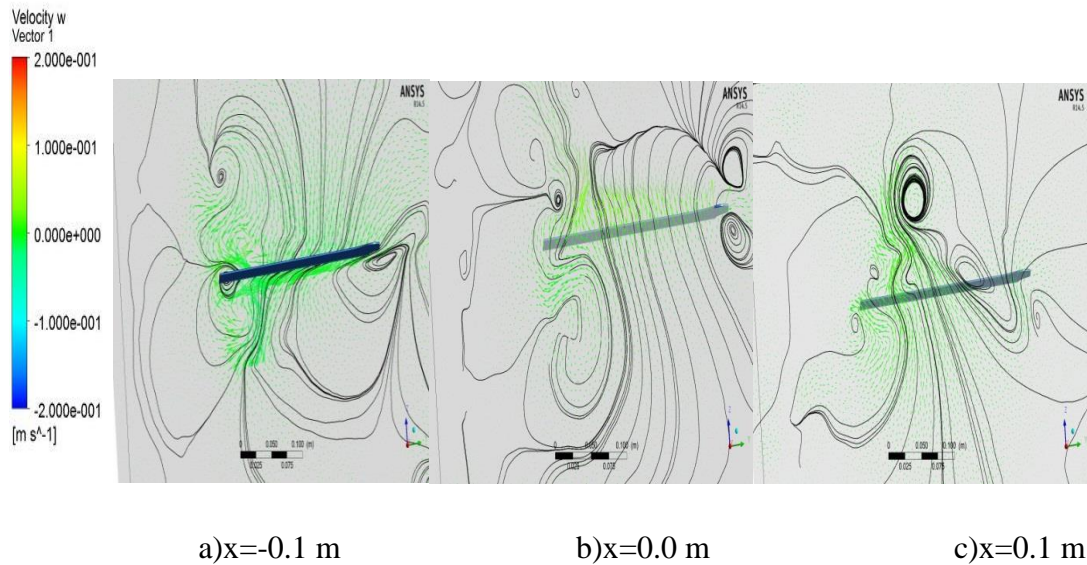
Figure 4.70 :Streamlines and velocity vectors at 5^0 pitch angle and 60^0 sweep angle (t*=4.0)

When fluid structure is compared with 5^0 pitch angle and $30^{\ 0}$ sweep angle, fluid structure of $5^{\ 0}$ sweep angle and 60^0 is more complex because of the sweep angle. Sweep angle is bigger so velocity is faster for same period time. Flow configuration is similar to doublet configuration from t*=3.2 to 4.0. Also counterclockwise and clockwise vortices exist on all planes. In addition, where streamlines are densed, velocity vectors are also much more there.

Case 5:

At t*=3.2

a)x=-0.1 m   b)x=0.0 m   c)x=0.1 m
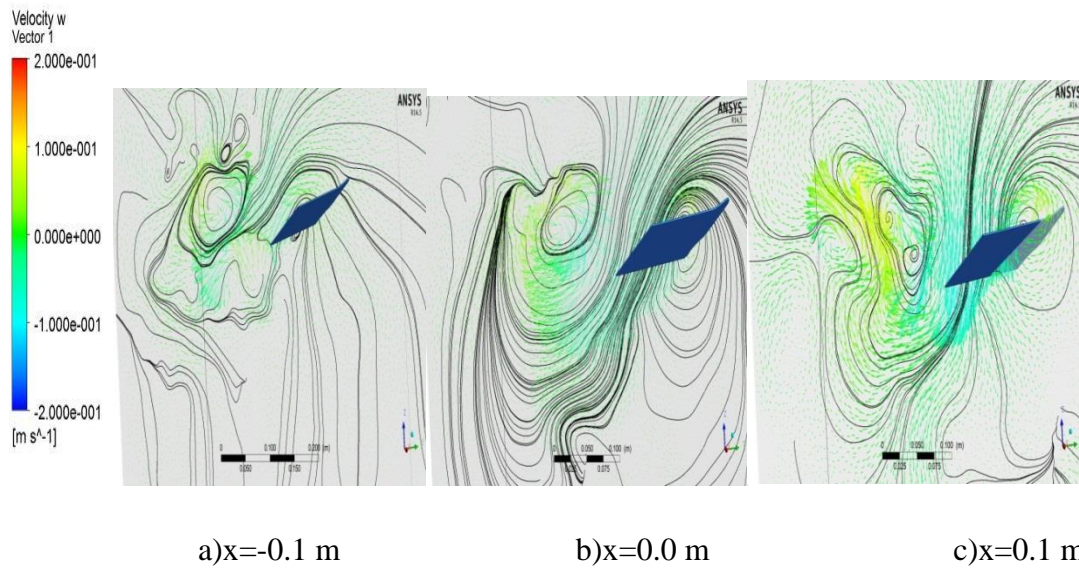
Figure 4.71 :Streamlines and velocity vectors at 30^0 pitch angle and 60^0 sweep angle (t*=3.2)

At t*=3.4

a)x=-0.1 m   b)x=0.0 m   c)x=0.1 m
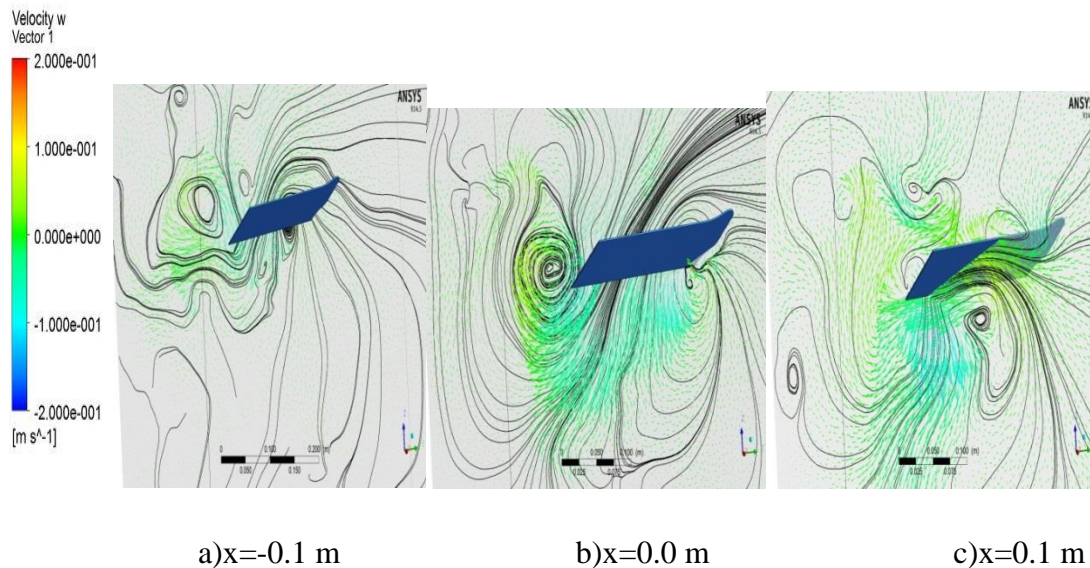
Figure 4.72 :Streamlines and velocity vectors at 30^0 pitch angle and 60^0 sweep angle (t*=3.4)

At t*=3.5

<div align="center">a)x=-0.1 m   b)x=0.0 m   c)x=0.1 m</div>
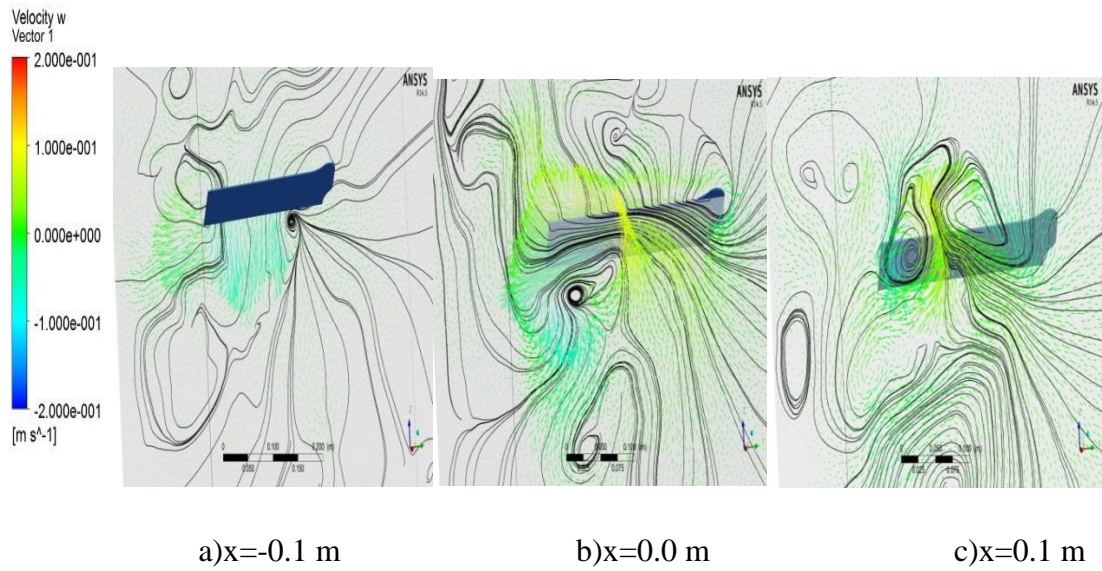
Figure 4.73 :Streamlines and velocity vectors at 30^0 pitch angle and 60^0 sweep angle (t*=3.5)

At t*=3.6
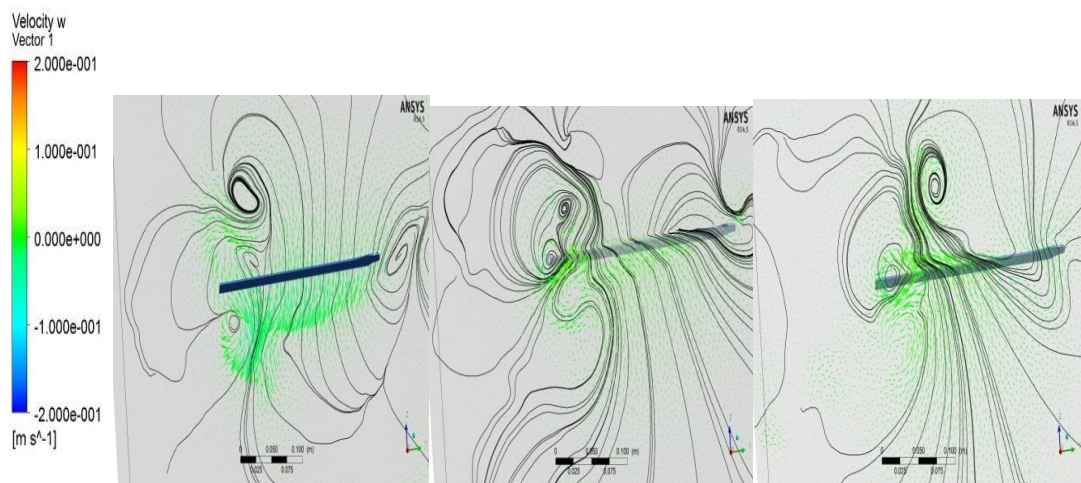

<div align="center">a)x=-0.1 m   b)x=0.0 m   c)x=0.1 m</div>
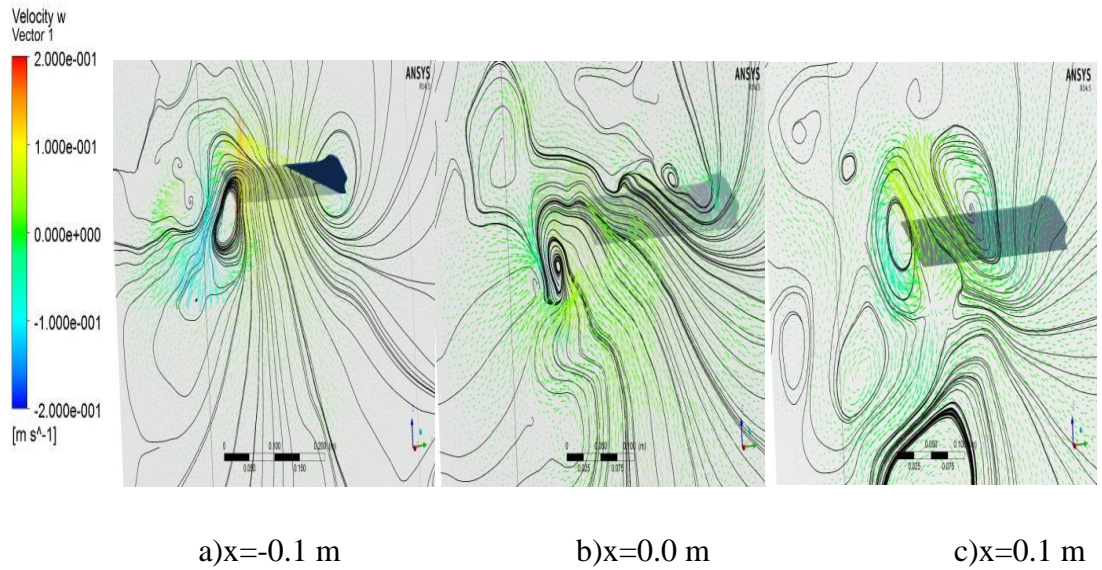
Figure 4.74 :Streamlines and velocity vectors at 30^0 pitch angle and 60^0 sweep angle (t*=3.6)

At t*=3.9

<table>
<tr><td>a)x=-0.1 m</td><td>b)x=0.0 m</td><td>c)x=0.1 m</td></tr>
</table>
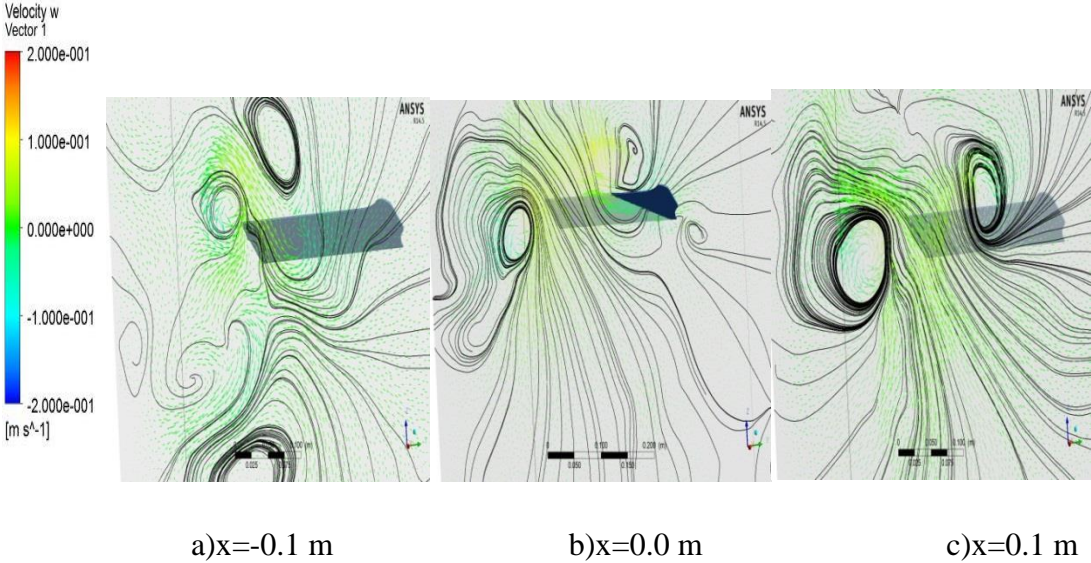
Figure 4.75 :Streamlines and velocity vectors at 30^0 pitch angle and 60^0 sweep (t*=3.9)

At t*=4.0

<table>
<tr><td>a)x=-0.1 m</td><td>b)x=0.0 m</td><td>c)x=0.1   m</td></tr>
</table>
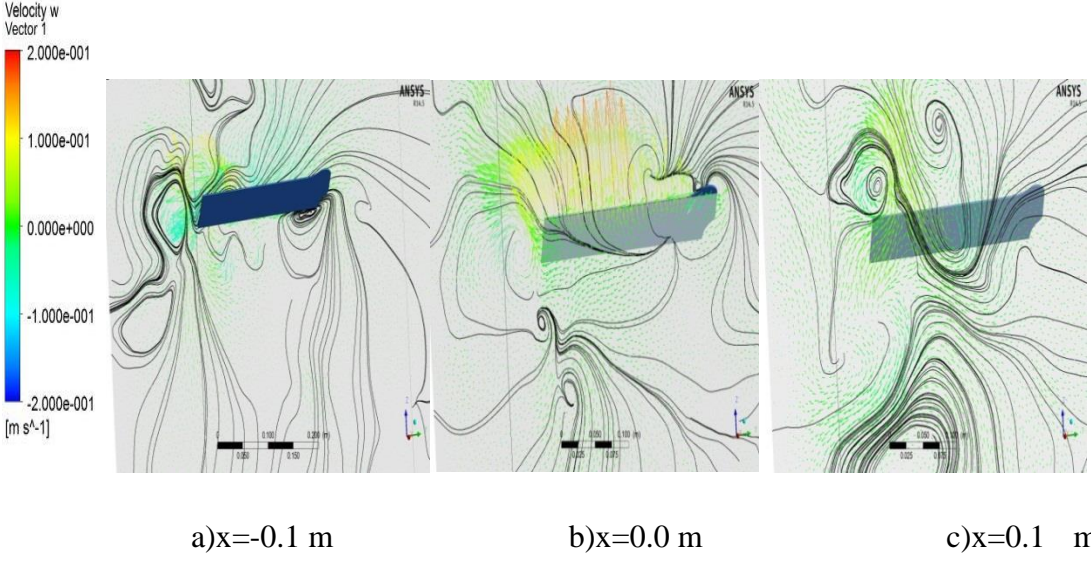
Figure 4.76 :Streamlines and velocity vectors at 30^0 pitch angle and 60^0 sweep angle (t*=4.0)

At t*=3.2 , plane 3 shows negative and positive velocity vectors at the intersection region between wing and plane 3. At t*=3.2 sweeping velocity is faster . Plane 1,2 and 3 have clockwise vortex. When the wing intersects and passes the Plane 3 fluid gets more complex but after passing the Plane 3 flow becomes laminar. In addition ,streamlines show that counterclockwise vortices exist on Plane3. Also at t*=3.6 and 3.9 flow is similar to doublet configuration on Plane 3.   Streamlines show that whether the fluid is uniform or not and vectors show the direction of flow. Magnitude of velocity vectors have greater positive value due to fast sweeping velocity.

Case 6:

At t*=3.2

a)x=-0.1 m   b)x=0.0 m   c)x=0.1 m
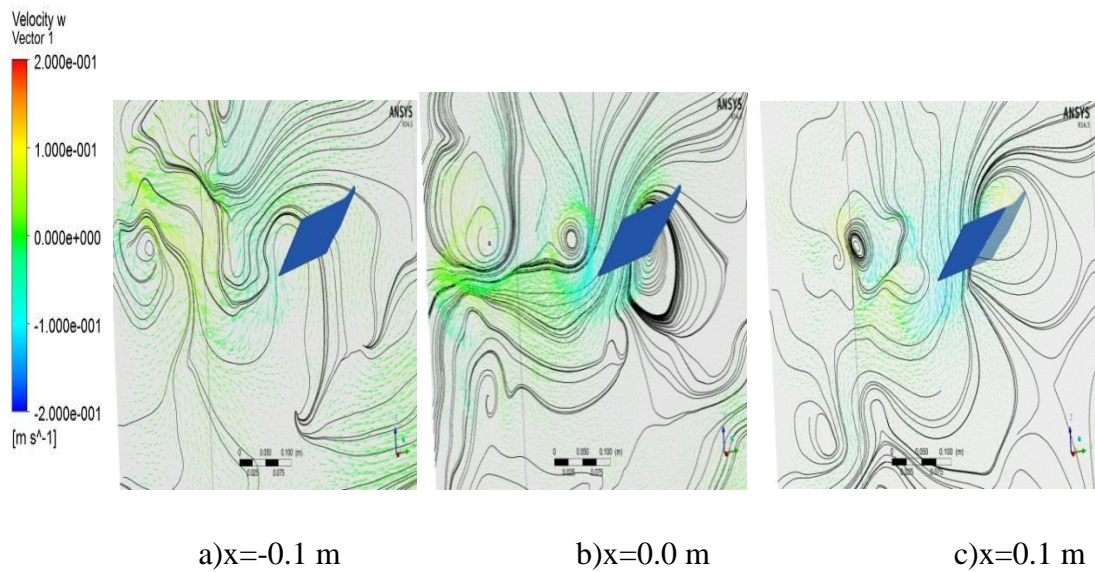
Figure 4.77 :Streamlines and velocity vectors at 45^0 pitch angle and 60^0 sweep angle (t*=3.2)

At t*=3.4

<p align="center">a)x=-0.1 m   b)x=0.0 m   c)x=0.1 m</p>
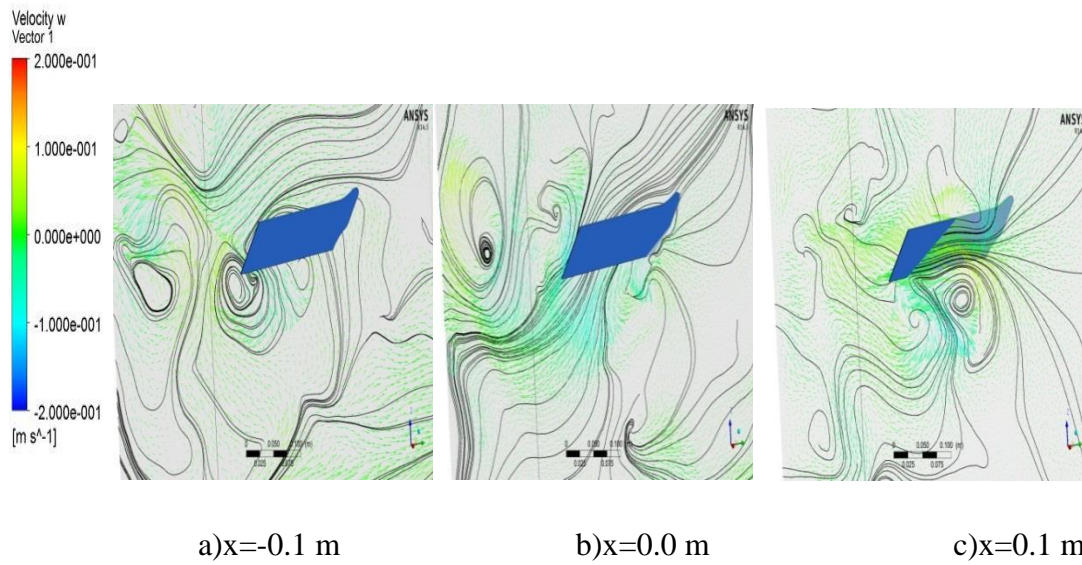
Figure 4.78 :Streamlines and velocity vectors at 45^0 pitch angle and 60^0 sweep angle (t*=3.4)

At t*=3.5

<p align="center">a)x=-0.1 m   b)x=0.0 m   c)x=0.1 m</p>
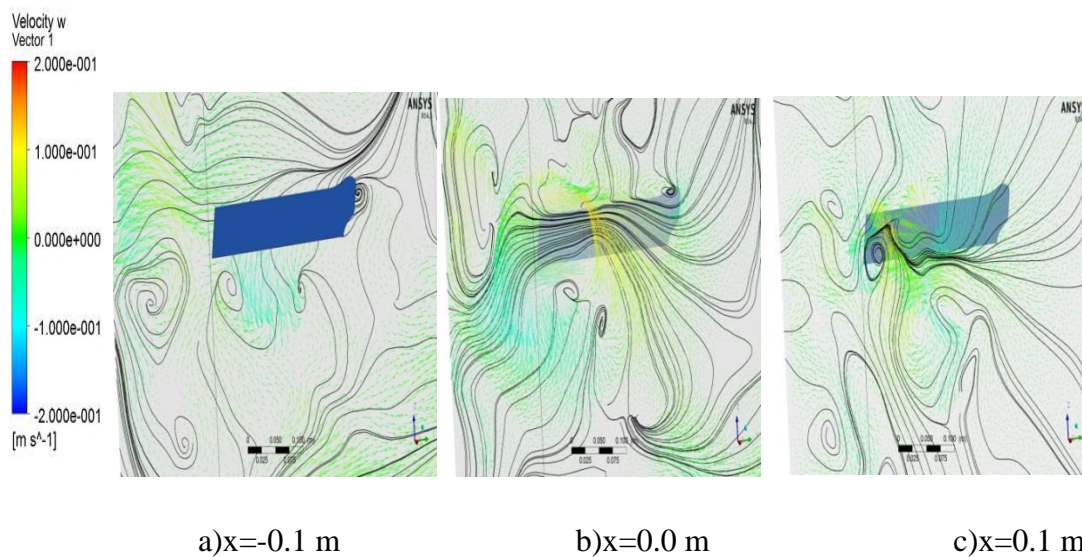
Figure 4.79 :Streamlines and velocity vectors at 45^0 pitch angle and 60^0 sweep angle (t*=3.5)

At t*=3.6

a)x=-0.1 m   b)x=0.0 m   c)x=0.1 m
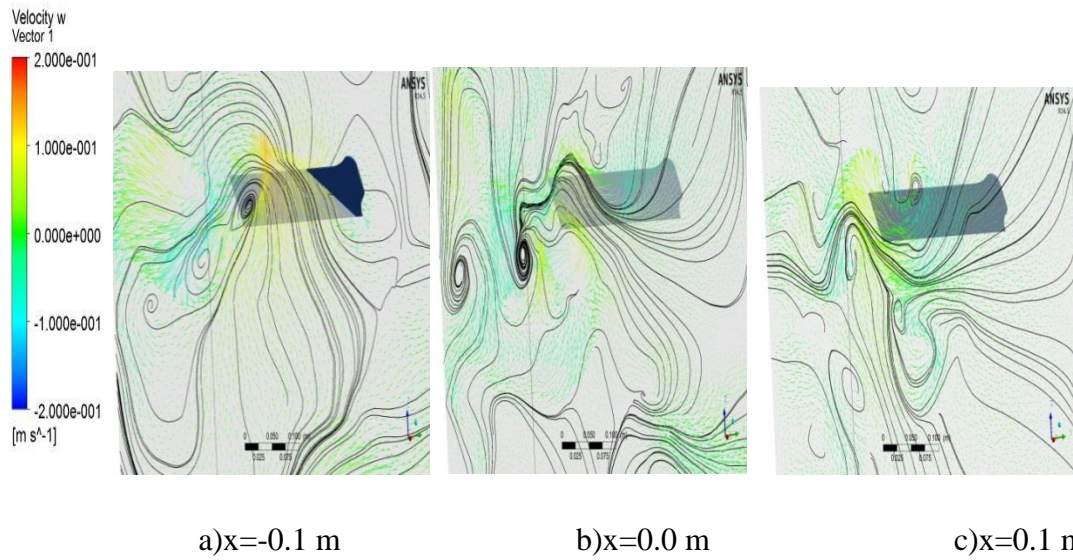
Figure 4.80 :Streamlines and velocity vectors at 45^0 pitch angle and 60^0 sweep angle (t*=3.6)

At t*=3.9

a)x=-0.1 m   b)x=0.0 m   c)x=0.1 m
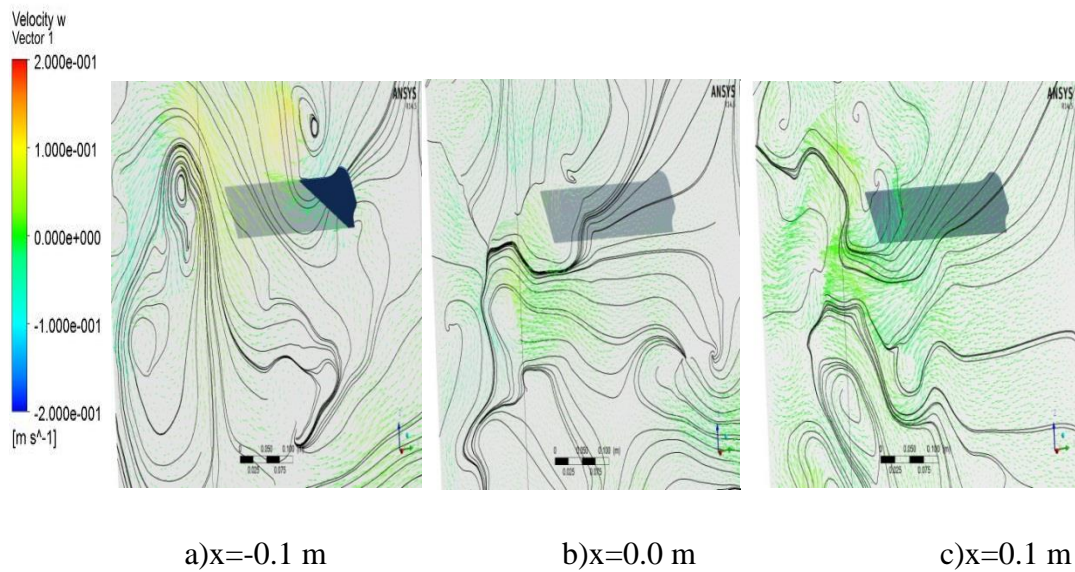
Figure 4.81 :Streamlines and velocity vectors at 45^0 pitch angle and 60^0 sweep angle (t*=3.9)

At t*=4.0

a)x=-0.1 m   b)x=0.0 m   c)x=0.1 m
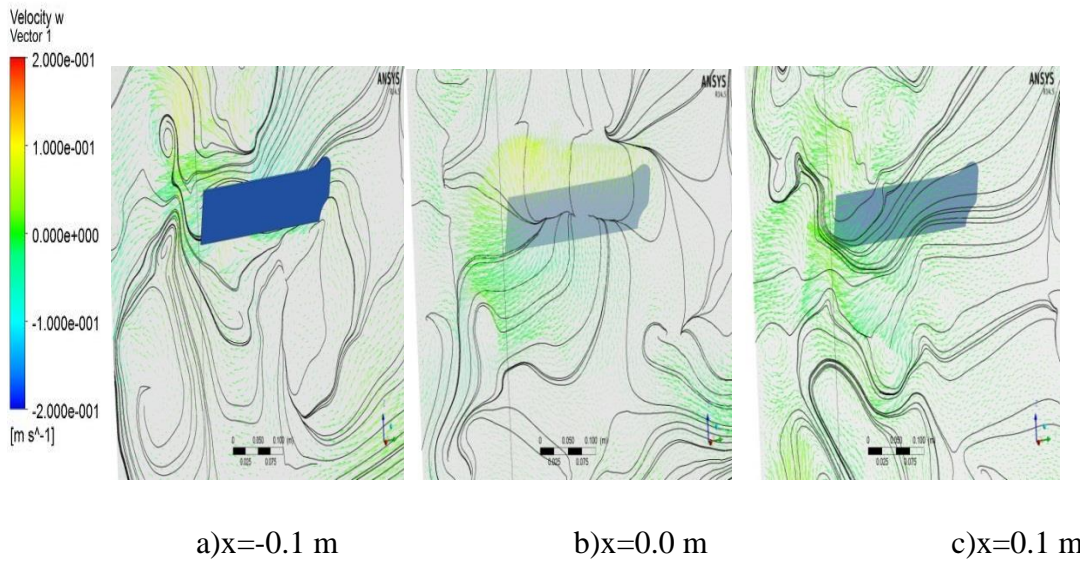
Figure 4.82 :Streamlines and velocity vectors at 45^0 pitch angle and 60^0 sweep angle (t*=4.0)

The fluid structure is quite complex because of the pitch angle and all the planes from t*=3.2 to t*=4.0 have two or three clockwise and counterclockwise vortices. Streamlines show vortex structure and the direction of vortices is determined by observing direction of velocity vectors. Negative and positive velocity vectors can be observed from the plots. Blue colour shows negative and red one shows positive velocity vectors. At t*=3.2 plane 2 shows a uniform flow at the bottom but when wing goes from t*=3.2 to 4.0, vortex structure takes place at the bottom.

CHAPTER 5

CONCLUSION

5.1 General Conclusions

In the present study , 3D water tank and flat plate was designed and then mesh model was obtained by Gambit software program. In addition, grid refinement technique was used to ensure that results are grid independent. Dynamic mesh method was used by uisng ANSYS Fluent package program. In order to obtain force results , pressure based method was performed. The results were taken at three different pitch angles (5º, 30º, 45º) with two sweeping amplitudes (60º and 120º). According to the results, drag and lift coefficints are highest value at 45º constant pitch angle. Also, lift and drag forces attain a periodic behaviour with respect to flapping motion for different constant pitch angles and their cycles are same, regardless of motion type. At 5º constant pitch angle , aerodynamic force coefficient results are low. Therefore in order to obtain high lift force coefficient thus lift and drag, pitch angle must be sufficiently high value. Also pressure distirbutions are investigated at different time steps for different pitch angles. Pressure distribution is observed that it is much higher where C_L is minimum and C_D is maximum. In addition, Pressure distribution is highest at 45º constant pitch angle with a 120º sweep angle. This means that our pressure distribution results are suited with plot results. Also , streamlines and velocity vectors are examined on different planes for cases from 1 to 6. When sweeping and pitch angles increase, it is observed that flow becomes more complex due to the sweeping velocity. To the knowledge of author, there are no other studies that investigate sweeping motion at different pitch angles and sweeping angles.

5.2 Recommendations for the Future Work

3D model of flat plate was investigated to a formal optimization study. 3D model of flat plate and water tank was designed by using Gambit software program and then with dynamic mesh method , forces and pressure distribution acting on flat plate for

laminar condition studied in detail. However , in laminar condition, a figure of eight motion can be examined at same pitch angles .As a future study, this might be considered.

REFERENCES

[1] Vincent H. R.,Ring T. C., "Encyclopedia of Insects", Academic Press,2003.

[2]Deppe,A.,"Hummingbirds"[Online].Available:http://smileimfine.com/2014/09/26/hummingbirds/[Accessed 10 June 2015]

[3] http://www.danubewings.com/helicopter-hovering-flight/[Accessed 20 May 2016]

[4] Dial K.P, "Inside look at how birds fly: Experimental studies of the inertial and external process controlling flight," in *Thirty-Eighths Symposium Proceedings Experimental TestPilots*, Lancaster, California, pp. 301–314, 1994.

[5] Betz A., "Ein beitrag zur erklarung des segelfuges," *Zeitschrift fur Flugtechnik and Motorluftschiffahrt*, vol. 3, pp. 269–272, 1912.

[6] Knoller R., "Die gesetze des luftwiderstandes," *Flung-und Motorechnik*, vol. 3, pp. 1–7,1909

[7] Jones K.D.and Platzer F.M., "Design and development considerations for biologically inspired flapping-wing micro air vehicles," *Experiments in Fluids*, vol. 13, pp. 26–32,2009.

[8] Willis D.J.,Israeli E.R., Persson P. O. , Drela, M. and Peraire J. , "A computational framework for fluid structure interaction in biologically inspired flapping flight," in *AIAA Applied Aerodynamics Meeting*, Miami, 2007, pp. 2007–3803.

[9] Persson P.O. , Willis D. J. and Peraire J. , "Numerical simulation of flapping wingsusing a panel method and a high-order Navier-Stokes solver," *International Journal for Numerical Methods in Engineering*, Feb. 2012, DOI: 10.1002/nme.3288.

[10] Jones K.D and Platzer F.M.,"An experimental and numerical investigation of flappingwing propulsion," in *37th Aerospace Sciences Meeting*, Reno, 1999.

[11] Jones K.D. and Platzer F.M.,"Experimental investigation of the aerodynamic characteristicsof flapping-wing micro air vehicles," in *41st Aerospace Sciences Meeting and Exhibit*, Reno, 2003.

[12] Katz J. and Plotkin A., *Low-speed aerodynamics: From wing theory to panel methods*: McGraw-Hill College, 1981.

[13] Liu H. and Kawachi K. , "A numerical study of insect flight," *Journal of Computational Physics*, vol. 146, pp. 124–156, 1998.

[14] Jones K. D. and Platzer F. M. ,"Anexperimental and numerical investigation of flappingwing propulsion," in *37th Aerospace Sciences Meeting*, Reno, 1999.

[15] Wang Z. J. , "Two dimensional mechanism for insect hovering," Physical Review Letters,vol. 85, pp. 2216–2219, 2000.

[16] Shyy W. , Berg M. and Ljungqvist D. ,"Flapping and flexible wings for biological

and micro air vehicles," Progress in Aerospace Sciences, vol. 35, no. 5, pp. 455–505, 1999.

[17] Grasmeyer J., and Keennon M., "Development of the Black Widow Micro Air Vehicle," AIAA, 2001.

[18] Ansys Fluent 14.0 Tutorial Guide

[19] Tuncer I.H., Platzer M.F. , *"Thrust Generation Due to Airfoil Flapping,"* AIAA Journal, Vol. 34, (2), Feb. 1996, pp. 324–331

[20] Tuncer I.H., Walz,R.,Platzer M.F. *"A Computational Study of the Dynamic Stall of a Flapping Airfoil,"* AIAA Paper 98–2519, June 1998.

[21] Isogai,K. Shinmoto,Y.Watanabe Y., *"Effects of Dynamic Stall on Propulsive Efficiency and Thrust of Flapping Airfoil,"* AIAA Journal, Vol. 37, (10), Oct. 1999, pp. 1145–1151.

[22] Grodnitsky D.L., *"Form and function of insect wings: The evolution of biological structures:"* John Hopkins University Press,1999.

[23] Pennycuick C. J. ,*"Modelling the flying bird:"* Academic Press, 2008.

[24] Floreano D. , Zuffere, J. C , Srinivasan M. V and Ellington , C. P. , Flying insects and robots: Springer- Verlag,2009.

[25] Mueller T. J., *Fixed and flapping wing aerodynamics for micro air vehicle applications*: AIAA, 2001

[26] Kim D. and Gharib M., "Experimental study of three-dimensional vortex structures in translating and rotating plates," *Experiments in Fluids*, vol. 49, pp. 329–339,2010. 15

[27] Zaeem A. Khan and Sunil K. Agrawal," Wing Force and Moment Characterization of Flapping Wings for Micro Air Vehicle Application" in *University of Delaware, Newark, DE 19716*

[28] Abhijit B.A., Saurav K. G., and Das,D., ," Aerodynamics of Flapping Wing at Low Reynolds Numbers: Force Measurement and Flow Visualization" in *Unsteady Aerodynamics Laboratory, Department of Aerospace Engineering, IIT Kanpur 208016, India*

[29] George,R.," Design and Analysis of a Flapping WingMechanism for Optimization", BYU ScholarsArchive,2011

[30] Morrison C.L., Vandenheede B.R., Kumar D., Bernal P.L., and Cesnik C., "Force Measurements of a Flapping Wing with Two Angular Degrees of Freedom and Bio-Inspired Kinematics" AIAA , 2012

[31] Eisma J.,"Flow visualization and force measurements on flapping-wing MAV DelFly II
in forward flight configuration", Delft University of Technology,2012

[32] Masarati P., Morandini M.,.Quaranta G.,Chandar D.,Roget B. and Sitaraman J., *"Tightly Coupled CFD/Multibody Analysis of Flapping-Wing Micro-Aerial Vehicles,"* 29th AIAA3, pp. 257_263 (2012)

[33] Niu Y., Liu S., , Chang C. and Tseng T. I., *"A Preliminary Study of the Three-Dimensional Aerodynamics of Flapping Wings,"* Journal of Applied Science and Engineering, Vol. 15, No. 3, pp. 257_263 (2012)

[34] San-Yih Lin and Jeu-Jiun Hu, *"Numerical Study of Flapping Wing,"* 33rd AIAA Fluid Dynamics Conference and Exhibit, 23-26 June 2003, Orlando, Florida

[35] Ellington C. P., van den Berg C., Willmott A. P., and Thomas A. L. R., "Leading-edge vortices in insect flight," *Nature*, vol. 384, pp. 626–630, 1996.

[36] van den Berg C. and. Ellington C. P, "The three-dimensional leading-edge vortex of a hovering model hawkmoth," *Philosophical Transactions of theRoyal Society of London Series B*, vol. 352, pp. 329–340, 1997.

[37] Liu H. and Kawachi K., "A numerical study of insect flight," *Journal of Computational Physics*, vol. 146, pp. 124–156, 1998.

[38] Liu H., Ellington C. P., Kawachi K., van den Berg C., and Willmott A. P., "A computational fluid dynamics study of hawkmoth hovering," *Journal of Experimental Biology*, vol. 146, pp. 461–477, 1998.

[39] Isaac K. M., Shivaram P. and DalBello T. , "Low Re, High α Aerodynamics with Controlled Wing Kinematics," AIAA 2003-4019-

[40] Usherwood J. R. and Ellington C. P., "The aerodynamics of revolving wings. I. Model hawkmoth wings," *Journal of Experimental Biology*, vol. 205, pp. 1547–1564, 2002.

[41] Knowles K.,. Wilkins P. C,. Ansari S. A, and Zbikowski R. W., "Integrated computational and experimental studies of flapping-wing micro air vehicle aerodynamics," in *3rd International Symposium on Integrating CFD and Experiments in Aerodynamics*, 2007, pp. 1–15.

[42] Liu H. and Kawachi K., "Leading-edge vortices of flapping and rotary wings at low Reynolds number," in *Fixed and flapping wing aerodynamics for micro air vehicle applications*, ed. T. J. Mueller: American Institute of Aeronautics and Astronautics, 2001, pp. 275–285. 18

[43] Drazin P. G. and Reid W. H., *Hydrodynamic stability*: Cambridge University Press, 1981.

[44] Yongsheng L. ," Numerical Investigation of Boundary Effects on Flapping Wing Study" in 47th AIAA Aerospace Sciences Meeting Including The New Horizons Forum and Aerospace Exposition 5 - 8 January 2009, Orlando, Florida

[45] Mayo D.B., "An investigation of a MAV-scale flexıble flapping wing in forward flight: flow field and airloads experiments with coupled CFD-CSD" University of Maryland,2014

[46] Prosser D., "Flapping wing design for a dragonfly-like micro air vehicle "Rochester Institute of Technology , RIT Scholar Works,2011

[47] Çakır H.," Experimental Analysis of 3-D Sweeping Wings", METU,2015

[48] Mutlu T.," Development and Testing of a 3 DOF Tandem Flapping wing Mechanism ". METU,2014

[49] Günaydınoğlu E.," Low Reynolds Number Aerodynamics of Flapping Airfoils in

Hover and Forward Flight ", METU,2010

[50] Hızlı H.," Numerical and Experimental Investigation of Pitching/Plunging Airfoils in Hover ", METU,2012

[51] Kaya M," Computation of Viscous Flows Over Flapping Airfoils and Parallel Optimization of Flapping Parameters",METU,2003

[52] Şenol G.," Design and Testing of a Four-bar Flapping wing Mechanism",METU 2016

[53] Ormanci F.," Development of Unsteady Models for Flapping Wings' Controller Design Approach ", METU 2016

[54] Berman G.J. and Wang Z.J.,"Energy minimizing kinematics in hovering insect flight", J. Fluid Mech. (2007), vol. 582, pp. 153–168.

APPENDIX

USER DEFINED FUNCTION CODE

```
#include "udf.h"

#include "dynamesh_tools.h"

#define   pi  3.1415926

#define  freq  0.1

real sg1 ,teta,per,a1;

DEFINE_CG_MOTION(ozgur, dt, v_cg, omega, time, dtime)

{

per= 1/freq  ;

a1= 30*pi/180 ;

sg1= pi/2 ;

teta= a2*sin(2*pi*time*freq+sg1) ;

omega[0] = 0.0;

omega[1] = 0.0 ;

omega[2] = swp ;


Message ("time = %f, omega[0] = %f, omega[1] = %f ,omega[2] = %f
,teta = %f\n", time, omega[0], omega[1] ,omega[2] ,teta*180/pi );


}
```